THE MIRA DISTANCE SCALE

by

Caroline Huang

A dissertation submitted to The Johns Hopkins University
in conformity with the requirements for the degree of
Doctor of Philosophy

Baltimore, Maryland
September, 2019

Abstract

This thesis covers recent improvements in our understanding of Mira variables that have led to the first Mira-based determination of the Hubble constant (H_0), the current expansion rate of the Universe. Miras are fundamentally-pulsating, large-amplitude, asymptotic giant branch variables that can be divided into Oxygen– (O–) and Carbon– (C–) rich subclasses. O–rich Miras are highly luminous and follow a tight Period-Luminosity Relation (PLR) in the near-infrared (NIR), allowing them to serve as extragalatic distance indicators. In light of the present Hubble tension and *JWST*, Miras have utility in the extragalactic distance scale to check Cepheid distances or calibrate nearby supernovae in early-type host galaxies that would be unlikely targets for Cepheid searches.

In the first part of this thesis I present year-long, NIR *Hubble* Space Telescope (*HST*) WFC3-IR observations of the megamaser host galaxy NGC 4258. I develop criteria for detecting and classifying O–rich Miras with NIR data and discover ~ 400 Mira candidates which I classify with high confidence as O–rich. I calibrate the absolute magnitude of O–rich Miras using the geometric distance to the water megamaser in NGC 4258.

I then present year-long *HST F160W* observations of NGC 1559, the host galaxy of a SN Ia, SN 2005df. These observations are the first dedicated search for Mira variables in a SN Ia host galaxy. I identify a sample of ~ 100 O–rich Miras — by far the most distant Miras ever observed — based on selection criteria developed in the search for Miras in NGC 4258. Using the O-rich Mira PLR and megamaser distance from NGC 4258, I obtain a distance modulus to NGC 1559. Based on the light curve of the well-observed, normal, low-reddening SN 2005df, I obtain a measurement of the fiducial SN Ia absolute magnitude of $M_B^0 = -19.27 \pm 0.13$. With the Hubble diagram of SNe Ia, I find $H_0 = 72.7 \pm 4.5$ km s^{-1} Mpc^{-1}. Combining the calibration from the NGC 4258 megamaser and the Large Magellanic Cloud detached eclipsing binaries gives a best

value of $H_0 = 73.3 \pm 3.9$ km s^{-1} Mpc^{-1} within 1σ agreement with the results of the Cepheid-SN Ia distance ladder.

The last part of this thesis focuses on work done using the Apache Point Observatory 3.5m telescope and spectrograph, TripleSpec. I obtained near-infrared spectra of 97 Galactic Miras, which I use to classify the Miras into Carbon- and Oxygen-rich subtypes. These classifications will eventually be used to calibrate the magnitude of Galactic Miras with *Gaia*, adding an additional anchor for the Mira distance scale.

Thesis Committee Members

Internal Committee Members

Adam Riess (Primary Advisor)
Bloomberg Distinguished Professor
Henry A. Rowland Department of Physics and Astronomy
Johns Hopkins Krieger School of Arts & Sciences

Marc Kamionkowski
William R. Kenan, Jr. Professor
Henry A. Rowland Department of Physics and Astronomy
Johns Hopkins Krieger School of Arts & Sciences

Kevin Schlaufman
Assistant Professor
Henry A. Rowland Department of Physics and Astronomy
Johns Hopkins Krieger School of Arts & Sciences

External Committee Members

Massimo Robberto
Observatory Scientist
NIRCam
Space Telescope Science Institute

Elena Sabbi
Associate Scientist
Instrument Division
Space Telescope Science Institute

Acknowledgments

The person to whom I undoubtedly owe the most for my scientific and personal growth is my advisor Adam Riess. While extremely busy and constantly in demand from reporters and scientists alike, he always made time for discussions about research. Both his passion for science and his scientific integrity were extremely inspiring to me.

I would like to thank my thesis committee members — Marc Kamionkowski, Massimo Robberto, Elena Sabbi, and Kevin Schlaufman. I also had the pleasure of interacting with other scientists — Stefano Casertano, Lucas Macri, Brice Menard, Steven Rodney, Lou Strolger, Patricia Whitelock, Rosemary Wyse, and Nadia Zakamska amongst them — who gave me insight into both science and life. Throughout my time in graduate school I worked with a number of postdocs and older graduate students who were not only mentors to me, but also my friends: Richard Anderson, Samantha Hoffmann, David Jones, Daniel Shafer, and Wenlong Yuan. The Bloomberg staff, whose contributions are often invisible, nonetheless supported me throughout my graduate education, especially Chantal Boisvert, Pam Carmen, Bill Deysher, Kelley Key, Pamela McCullough, Reid Mumford, Bill Ruff, Brian Schriver, Jonathan Soffar, Jesse Warford, and Steve Wonnell. Additionally, I would like to thank my piano instructor Marianna Prjevalskaya, whose wit and musical insight I looked forward to every lesson.

I would also like to thank the friends that have supported me during my time in graduate school: Donnetta Allen, Michael Busch, Leslie Brown, Joel Clemmer, Kwang Cho, Anthony Cordisco, Suhail Dhawan, Kevin Fogarty, Kirsten Hall, Rajpreet Heir, Jessica Hopkins, Terrell Hughes, Charles Hussong, Elizabeth Johnson, D'Arcy Kenworthy, Brooks Kinch, Erini Lambrides, Nison Li, Alice Li-Fogarty, Lucia Mocz, Jacob Mokris, Julian Munoz, Isha Nayak, Caro Nunez, Daniel Pfeffer, Taisha Rodriguez, Rohini Shivamoggi, Jessica Streitz, Jacob Tutmaher, Douglas Watts, Zhilei Xu, and Min Joo Yi.

A large part of my struggles in graduate school came in overcoming the difficulties in my personal life. I would not be the same person I am today without my therapist at the JHU Counseling Center, Jeanna Stokes. For that, I could not be more grateful. I would also like to thank Katherine Jones, who helped me continue my growth as a person.

Finally, I would like to thank my parents and my partner, Nikhil Anand, for their unconditional love and support.

Contents

List of Figures

Chapter 1

Introduction

The expansion of the Universe is one of the most important cosmological discoveries ever made. Though theoretical underpinnings suggested dynamic models for the Universe, it was not until 1929, when Edwin Hubble published his data illustrating a linear correlation between distance to galaxies and their recessional velocities, that the scientific paradigm shifted from a static Universe to an expanding one. As a result, the current expansion rate of the Universe is known as the Hubble constant (H_0).

To produce his groundbreaking result, Hubble measured the distances to 24 nearby galaxies using a variety of methods, including the Cepheid variable Period-Luminosity Relation (also known as the Leavitt Law), which is still used in the most precise (Riess et al., 2019, 2016) measurements of H_0 today. He combined these distance measurements with recessional velocities (obtained from measurements of redshift), resulting in the first Hubble diagram. This linear relationship between redshift and distance is known as Hubble's law, and can be expressed as $v = H_0 D$, where v is the recessional velocity, and D is the proper distance between the observer and the galaxy. Hubble's law holds for galaxies that are distant enough that their peculiar velocities — the velocities resulting from gravitational interactions — are small compared to their recessional velocities, but still at low-enough redshift that cosmological model-dependencies of the redshift-velocity relation do not come into play. Objects whose recessional velocities are dominated by this expansion are considered to be in the "Hubble flow."

Measurements of H_0 have been a source of contention from the start. H_0 is typically given in units of inverse time (km s^{-1} Mpc^{-1}). A Hubble time, t_H, given by $t_H \equiv 1/H_0$, is the age of the Universe given a linear expansion, and is an approximation to the

true age of the Universe. Hubble's initial value of 500 km s^{-1} Mpc^{-1} resulted in an age of the Universe of 2 Gyr, in conflict with radioactive dating of rocks that showed that the Earth was at least 1 Gyr older. This conflict was resolved by the discovery of Type II Cepheids — Population II variable stars that are more than 1.5 magnitudes fainter than Classical Cepheids of the same period. Hubble had treated both classes of variable star as one standard candle. This, in addition to other calibration mistakes he made in his measurements, resulted in an H_0 that was erroneously high. The debate eventually shifted to H_0 measurements that put the value at 50 km s^{-1} Mpc^{-1} or 100 km s^{-1} Mpc^{-1}, before finally settling on an answer that lay somewhere in the middle — $H_0 = 71 \pm 2$ (stat) ± 6 (sys) — by the 2000s (Freedman et al., 2001).

Today value of H_0 is once again a source of growing interest in astrophysics. One of the most intriguing issues in observational cosmology is the discrepancy between H_0 measured in the present-day Universe using the Cepheid-supernovae distance ladder (Riess et al., 2016, hereafter, R16) and gravitational lensing time delays (Bonvin et al., 2017; Wong et al., 2019) and the one inferred from the early Universe using the cosmic microwave background (CMB) data assuming a ΛCDM cosmology (Planck Collaboration et al., 2018). As uncertainties in both the "late" Universe and "early" Universe measurements of H_0 have decreased, the discrepancy has only grown more pronounced, from 3.4σ between R16 and Planck Collaboration et al. (2016), to 5.3σ today after combining R19 and H0LiCOW and comparing with Planck Collaboration et al. (2018). The persistence of such a discrepancy could signal the existence of physics beyond ΛCDM, the Standard Model of Cosmology.

In ΛCDM, the Universe is homogenous, isotropic, flat, and composed of three major components: dark energy (Λ, 68%), which has a constant energy density, cold dark matter (CDM, 27%), and ordinary baryonic matter (5%). There are six free parameters and several other parameters that are fixed (including the sum of the three neutrino masses $\sum m_\nu$, and the effective number of neutrino species, $N_{\rm eff}$). By comparing the angular power spectrum of the CMB with the predictions from a 6-parameter ΛCDM, it is possible to derive a number of calculated values, including prediction of $H_0 = 67.4 \pm 0.5$ km s^{-1} Mpc^{-1}. Predicting H_0 in this way involves the application of early-Universe physics and assumptions about the fixed parameters in the cosmological model and thus is considered an "Early" Universe measurement of H_0. "Late" Universe measurements of

H_0 are made in the present-day, local Universe and do not depend on these assumptions. A comparison of H_0 calculated or measured through these two methods thus provides an "end-to-end" test of Standard Model (Verde et al., 2019).

In light of this, a number of alternatives to the local Cepheid distance ladder have been explored. Amongst them are Tip of the Red Giant Branch (TRGB) (Freedman et al., 2019) and Miras. Both TRGB and short-period ($P < 400$ days) Miras are older stellar populations. TRGB uses the luminosity of the brightest red giant stars in a galaxy as a standard candle whereas Miras are large-amplitude, fundamentally-pulsating asymptotic giant branch (AGB) stars that follow a tight (scatter ~ 0.13 mag) Period-Luminosity Relation (PLR) in the near-infrared (NIR). Both TRGB and Miras have the advantage that they are ubiquitous and can be found in all galaxies. While Cepheids are also evolved stars, they have massive progenitors and thus are typically only found in galaxies with active star formation. However, Miras have the additional advantage of being brighter than TRGB, and of comparable brightness to Cepheids in the NIR. TRGB is up to 2.5 mag fainter than Cepheids in the optical, and 0.5 mag fainter in the NIR, so TRGB will not be able to calibrate Type Ia supernovae (SNe Ia) out to the same volume as Cepheids.

Despite their advantages, Miras they have remained a relatively underused distance indicator because of their long periods (from 100 days on the short-period end to over 2000 days in the long-period end), their existence as two subclasses (Carbon– and Oxygen– rich), and the large scatter in their optical PLRs (Ita & Matsunaga, 2011). Long-baseline observations (minimum of about a year) in the NIR or longer wavelengths are necessary to characterize Mira periods and determine their mean magnitudes. In addition, as AGB stars, their angular sizes are larger than their parallaxes (their physical sizes are greater than 1AU). This extended size is also accompanied by time-variable asymmetries (Paladini et al., 2017) that have been speculated to result from giant convection cells (Lattanzi et al., 1997) or caused by nonradial pulsations. Together, these make determinations of their absolute magnitudes challenging, and the previous best calibrations of the Mira PLR have been extragalactic. Even with *Gaia*, obtaining Mira parallaxes may only be possible with later data releases that can properly account for movement of the photocenter and the resolved profiles of these sources (Whitelock, 2018).

In this thesis, I address the issue of calibration and separation of Miras into Oxygen– (O–) and Carbon– (C–) rich subclasses in Chapter 2. I used year-long baseline *Hubble* Space Telescope (*HST*) WFC3/IR observations of Miras in the water megamaser host NGC 4258. This work was done with my collaborators Adam G. Riess, Samantha L. Hoffmann, Christopher Klein, Joshua Bloom, Wenlong Yuan, Lucas M. Macri, David O. Jones, Patricia A. Whitelock, Stefano Casertano, and Richard I. Anderson. It first appeared as Huang et al. (2018).

In Chapter 3, I use the calibration of Miras from Chapter Two to determine the distance to a SN Ia host galaxy, NGC 1559. From this I obtain a fiducial SN Ia absolute magnitude and the first Mira-based H_0. This work was first done with my collaborators Adam G. Riess, Wenlong Yuan, Lucas M. Macri, Nadia L. Zakamska, Stefano Casertano, Patricia A. Whitelock, Samantha L. Hoffmann, Alexei V. Filippenko, and Daniel Scolnic. This work is being submitted for publication.

In Chapter 4, I present a catalog of 97 Miras with spectra taken from the ARC 3.5m telescope located at Apache Point Observatory. I use these spectra to classify the Miras into O— and C— rich subclasses. David O. Jones helped in part of the collection of the data, and Adam G. Riess served as the faculty sponsor on the proposals.

Chapter 2

A Period-Luminosity Relation for Miras in NGC 4258, An Anchor for a New Distance Ladder

2.1 Introduction

The value of the Hubble constant (H_0), the current expansion rate of the Universe, is a source of great interest in astrophysics. The improved precision in H_0 measurements (Riess et al., 2016) has revealed a 3.4σ discrepancy with the value inferred from observations of the cosmic microwave background (CMB) under the assumption of a ΛCDM cosmology (Planck Collaboration et al., 2016). Although the local results have been confirmed (Follin & Knox, 2017; Dhawan et al., 2017; Bonvin et al., 2017) and the discrepancy is not dependent on any one datum (Addison et al., 2018), the standard of proof is high for new physics and additional crosschecks are warranted.

The most precise local measurement of H_0 relies on Cepheid variables as distance indicators (Riess et al., 2016) (hereafter, R16) to calibrate the luminosity of type Ia supernovae (hereafter, SNe Ia) in hosts at nearby distances of 10-40 Mpc. Cepheids remain the best understood and most vetted primary distance indicator (Freedman et al., 2001; Bono et al., 2010).

The next generation of space-based telescope, the *James Webb* Space Telescope (*JWST*), will not have the optical filters equivalent to those found in *Hubble* Space Telescope (*HST*), making it more difficult to search for Cepheids beyond $\sim$ 40 Mpc to

increase the sample of SNe Ia calibrators, which is essential to improve the precision of H_0. Cepheids are typically detected in the optical, where they have amplitudes ~ 1 mag. Their near-infrared (NIR) amplitude variations are much smaller (~ 0.3 mag) and they lose their characteristic optical saw-toothed light curve shape which helps in their identification. This makes them more difficult to identify as variable stars at NIR wavelengths. As an alternative, Jang & Lee (2017) have used the Tip of the Red Giant Branch (TRGB) observed with *HST* to check the Cepheid distances in nearby hosts, finding good agreement. However, because the TRGB is ~ 2.5 mag less luminous than Cepheids in the optical and ~ 0.5 mag less luminous in the NIR, this method will not be able to measure distances within the same volume as a Cepheid distance ladder.

A possible solution to this problem is using Mira variables to measure extragalactic distances. Miras are highly-evolved asymptotic giant branch (AGB) stars. They can provide an alternative distance indicator, allowing a simultaneous check of Cepheid distances and increasing the SNe Ia sample with *JWST*. Miras are long-period ($P \gtrsim 100$ days), large amplitude ($\Delta V > 2.5$ mag, $\Delta I > 0.8$ mag) M or later spectral-type pulsating variable stars (Kholopov et al., 1985; Soszyński et al., 2009b). They are divided into oxygen- and carbon-rich spectral classes based on surface chemistry, with oxygen-rich (O-rich) Miras having a carbon-to-oxygen C/O ratio < 1 and a carbon-rich (C-rich) Miras having C/O > 1. AGB stars with C/O ~ 1 are known as S stars. All stars are thought to enter the AGB phase as O-rich stars, but some evolve into C-rich stars due to dredge-up events (Iben & Renzini, 1983). The O-rich Miras have been shown to follow a tight ($\sigma \sim 0.14$ mag) Period-Luminosity Relation (PLR) in the K-band (Whitelock et al., 2008; Yuan et al., 2017a) that is comparable to the scatter in the Cepheid PLR in that bandpass (Macri et al., 2015). The relation of Miras in the amplitude-period space relative to other classes of variables stars, including other distance indicators like Cepheids and RR Lyrae, is shown in Figure 2.1. As can be seen in the figure, they are distinguished from other variable stars by their large amplitudes and long, year-scale periods.

Miras have a few advantages as distance indicators over Cepheids. Stars of a wide range of stellar masses go through the AGB phase, but Mira progenitors are typically of low-to-intermediate mass ($\sim 1 M_\odot$) while Cepheids have intermediate to high-mass progenitors ($> 5 M_\odot$). Due to the bottom-heavy distribution of the stellar initial mass

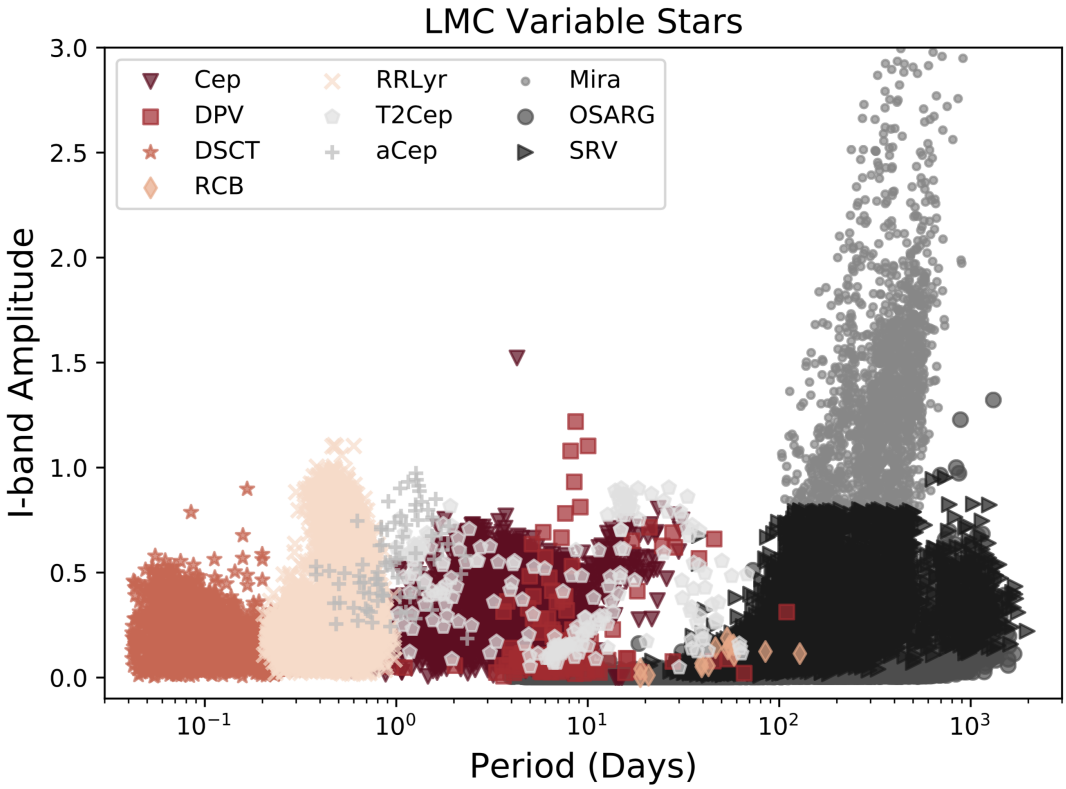

Figure 2.1 The distribution of I-band amplitude and period for LMC variable stars discovered by the Optical Gravitational Lensing Experiment (OGLE) III Survey (Udalski et al., 2008; Soszynski et al., 2008; Soszyński et al., 2008, 2009a,b,c; Poleski et al., 2010b,a). Abbreviations are as follows: Cep–Classical Cepheid; DPV–Double Period Variable; DSCT–δ Scuti variable; RCB–R Coronae Borealis variable; RRLyr–RR Lyrae; T2Cep–Type II Cepheid; aCep–anomalous Cepheid; Mira–Mira; OSARG–OGLE Small Amplitude Red Giant; SRV–Semi-Regular Variable. Miras and Semi-Regular Variables (SRVs) are separated on the basis of I band amplitude of variation, but this distinction is somewhat arbitrary (Soszynski et al., 2005). Miras, Cepheids, Type II Cepheids, RR Lyrae, and SRVs are radially-pulsating variables that follow Period-Luminosity Relations.

function (IMF), Mira progenitors are much more common than Cepheid progenitors. Lower mass stars also live longer and evolve more slowly than higher mass stars. In addition, as seen in Figure 2.2, their NIR amplitudes are about twice as large as NIR Cepheid amplitudes, making it much easier to discover these with infrared-only observatories like *JWST*. Since they are older stars, Miras can also be found in galaxies without current star formation. This would allow the calibration of SNe Ia luminosities in early-type host galaxies with Miras.

To test the efficacy of Miras as standard candles and demonstrate the feasibility of discovering and characterizing Miras with *HST* and *JWST*, we conducted a year-long, 12-epoch search for Mira variables in the megamaser-host galaxy NGC 4258 using WFC3 *F160W* data. Our goals are to develop criteria for identifying and classifying Miras using primarily NIR photometry, to provide an initial test of the relative distances from Cepheids, and to obtain a calibrated Mira PLR relation relative to the Large Magellanic Cloud (LMC) by using the water megamaser distance to NGC 4258.

Throughout this Chapter, we refer to peak-to-trough variation in a Mira's magnitude over the course of one cycle as its 'amplitude.' Statistical and systematic uncertainties are represented as σ_r and σ_s or with the subscripts r and s respectively.

2.2 Observations, Data Reduction, and Photometry

2.2.1 Observations

With a roughly monthly observational cadence, we used twelve epochs of *HST* WFC3 data (GO 13445; PI: Bloom) collected between October 2, 2013 and August 3, 2014 to search for Miras in NGC 4258. The field was chosen to overlap with the NGC 4258 "inner" field from Macri et al. (2006), who discovered $\sim$ 50 Cepheids (see below for a description of these observations). The term "inner" references the field's proximity to the nucleus of NGC 4258. The observations were centered at RA = $12^{\rm h}18^{\rm m}52^{\rm s}.800$ and Dec = $+47°20'19.70''$ (J2000.0).

All twelve epochs have *F160W* and *F125W* data, but the first epoch is comprised of four 703s exposures in both the *F160W* and *F125W* (*HST* J-band). The other epochs each contain four 553s *F160W* exposures and one 353s *F125W* exposure.

This field was previously observed in *F160W* (GO 11570; PI: Riess) in December

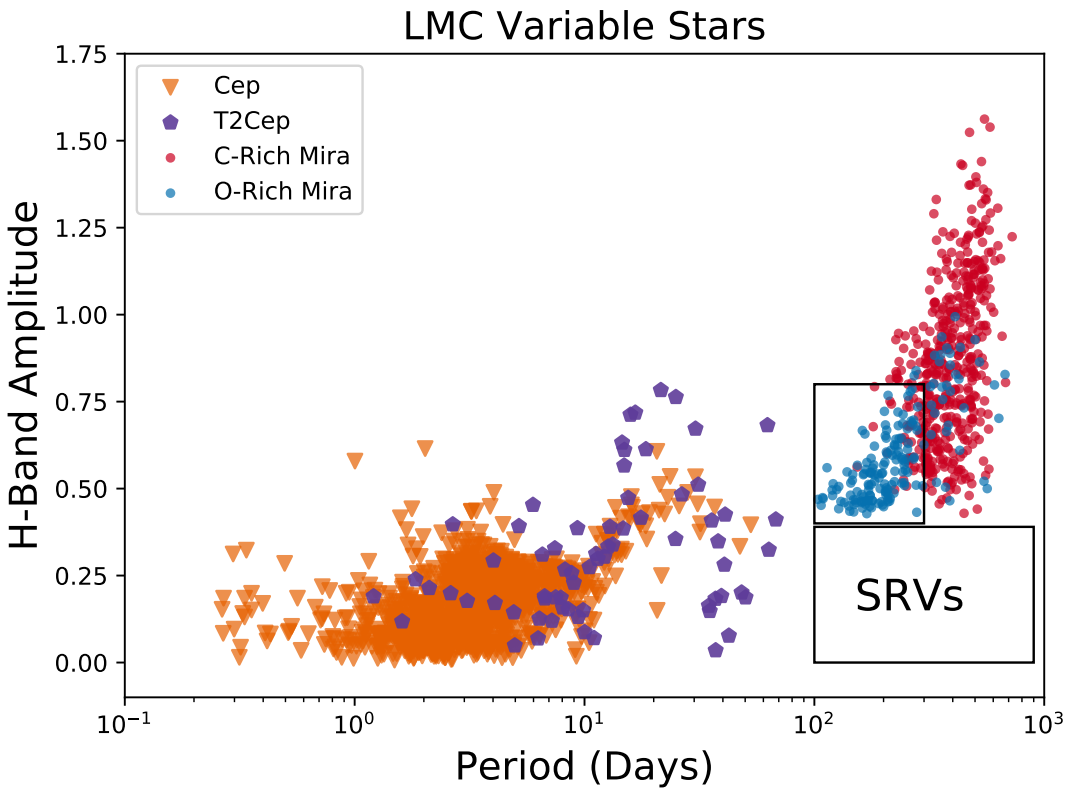

Figure 2.2 The distribution of H-band amplitude and period for LMC variable stars. Cepheid (Macri et al., 2015) and Type II Cepheid (Bhardwaj et al., 2017) points use data from the LMC Near-Infrared Synoptic Survey. Abbreviations are same as for Figure 2.1. H-band amplitudes of Miras are from Yuan et al. (2017a). The boxes show the target selection of O-rich Miras and the location of SRVs.

Table 2.1. *HST* Observations Used in this Work

Epoch	Proposal ID	Camera	UT Date	Exposure Time (s)				
				F435W	F555W	F814W	F125W	F160W
H-01	13445	WFC3	2013-10-02	···	···	···	2812	2812
H-02	13445	WFC3	2013-11-17	···	···	···	353	2212
H-03	13445	WFC3	2013-12-03	···	···	···	353	2212
H-04	13445	WFC3	2013-12-22	···	···	···	353	2212
H-05	13445	WFC3	2014-01-26	···	···	···	353	2212
H-06	13445	WFC3	2014-02-11	···	···	···	353	2212
H-07	13445	WFC3	2014-03-14	···	···	···	353	2212
H-08	13445	WFC3	2014-04-10	···	···	···	353	2212
H-09	13445	WFC3	2014-05-11	···	···	···	353	2212
H-10	13445	WFC3	2014-06-08	···	···	···	353	2212
H-11	13445	WFC3	2014-07-05	···	···	···	353	2212
H-12	13445	WFC3	2014-08-03	···	···	···	353	2212
O-01	9810	ACS/WFC	2003-12-06	1800	1600	800	···	···
O-02	9810	ACS/WFC	2003-12-07	1800	1600	800	···	···
O-03	9810	ACS/WFC	2003-12-08	1800	1600	800	···	···
O-04	9810	ACS/WFC	2003-12-09	1800	1600	800	···	···
O-05	9810	ACS/WFC	2003-12-11	1800	1600	800	···	···
O-06	9810	ACS/WFC	2003-12-13	1800	1600	800	···	···
O-07	9810	ACS/WFC	2003-12-16	1800	1600	800	···	···
O-08	9810	ACS/WFC	2003-12-20	1800	1600	800	···	···
O-09	9810	ACS/WFC	2003-12-24	1800	1600	800	···	···
O-10	9810	ACS/WFC	2003-12-31	1800	1600	800	···	···
O-11	9810	ACS/WFC	2004-01-08	1800	1600	800	···	···
O-12	9810	ACS/WFC	2004-01-19	1800	1600	800	···	···
M-13	11570	WFC3	2009-12-17	···	···	···	···	2012
M-14	11570	WFC3	2009-12-17	···	···	···	···	2012
M-13b	11570	WFC3	2010-05-29	···	···	···	···	2012

Note. — Exposure times are rounded to the nearest second. The epochs labeled represent the results of three campaigns to observe NGC 4258. The H-xx epochs were aimed at discovering Miras. The O-xx epochs were observed previously to search for Cepheids. The M-xx epochs were observed in order to create a mosaic image of the whole galaxy. We have no epochs with simultaneous optical and infrared observations.

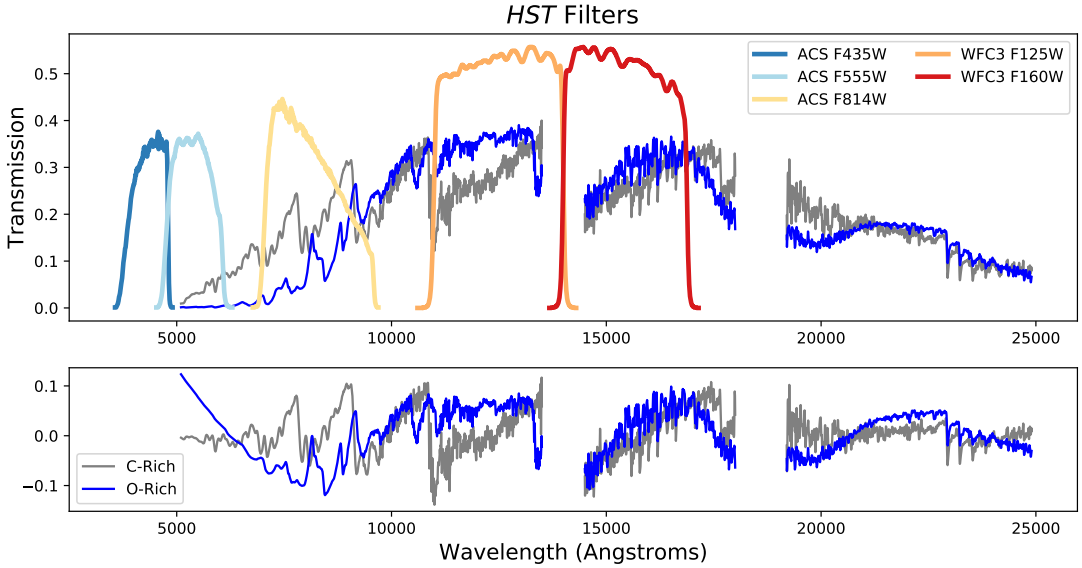

Figure 2.3 The transmission curves for every *HST* filter in the images we analyzed shown with example O-rich and C-rich Mira spectra of the stars WW Sco and BH Cru respectively from Lançon & Wood (2000). In the bottom image, the continuum emission has been subtracted out to better show the difference in spectral features. The *F435W*, *F555W*, *F814W*, *F125W*, *F160W* filters roughly correspond to *B, V, I, J, and H* in ground-based filter systems.

2009 and May 2010. These earlier images were taken to create a mosaic of NGC 4258 in *F160W* and to follow-up a number of long-period Cepheids discovered in the galaxy from the ground. This provided a thirteenth epoch of observation for most objects, while a few in the overlapping regions of the mosaic were observed twice and had fourteen epochs.

As already mentioned, this field was previously observed at optical wavelengths using *HST* (GO 9810; PI: Greenhill Macri et al., 2006). These observations were taken with the Advanced Camera for Surveys (ACS) (Ford et al., 2003) in *F435W*, *F555W*, *F814W*. The optical time-series consisted of twelve epochs between December 5, 2003 and January 19, 2004 with an observation spacing that followed a power law to allow for the detection of Cepheids at the largest possible range of periods. A summary of all of the observations used in the analysis is shown in Table 3.1 and transmission curves for every filter are shown in Figure 2.3.

2.2.2 Data Reduction

We use pipeline-processed images downloaded from the Canadian Astronomy Data Centre (CADC). For the *F125W* and *F160W* images taken between October 2013 and August 2014, we generated drizzled and stacked images for each epoch and filter using v.1.1.16 of Astrodrizzle (Gonzaga, 2012). Each image contained four sub-pixel dither positions. The images were drizzled to a pixel scale of 0.08"/pix instead of the 0.13"/pix scale of WFC3 IR. As the baseline of observations of the field spanned almost a year, the roll angle of the camera changed by 282 degrees over the course of our observations. We choose the first epoch as the reference image and aligned all of the subsequent images onto it using DrizzlePac (Gonzaga, 2012).

We used DAOMATCH and DAOMASTER, kindly provided by P. Stetson, to match sources in common between Macri et al. (2006) and our *F160W* master image.

2.2.3 Photometry and Calibration

Given that our fields are quite crowded, we used tools specifically designed for crowded fields: DAOPHOT/ALLSTAR (Stetson, 1987) and ALLFRAME (Stetson, 1994). Our DAOPHOT procedure is different from the R16 NIR forced photometry because we conduct a search for Miras in WFC3 *F160W* and do not know their positions *a priori*. We created point-spread-functions (PSFs) in DAOPHOT with *F160W* and *F125W* exposures of the standard star P330E. Due to the crowded nature of our fields, we were unable to find enough isolated stars to make PSFs using sources in our field. Aperture corrections, discussed in §2.2.4, were used to account for imperfections in the PSF model.

We stacked all of the *F160W* observations to make a deeper "master" image. Then we used the DAOPHOT routine FIND to detect sources with a greater than 3σ significance level in standard deviations from the sky background noise. Then the DAOPHOT routine PHOT was used to perform aperture photometry. We input the star list produced from the aperture photometry into ALLSTAR for PSF photometry, optimized for a 2.5 pixel full-width at half-maximum (FWHM). We then repeated these steps on the star-subtracted image generated by ALLSTAR (with all of the previously-discovered sources removed) to produce a second source list. The two source lists were then con-

Table 2.2. Secondary Standards

ID	R.A. (J2000.0)	Dec. (J2000.0)	X (Pixels)	Y (Pixels)	F160W (mag)	Error (mag)
49680	12 18 46.910	+47 19 58.43	987.352	1019.138	19.035	0.013
23564	12 18 48.964	+47 20 36.93	877.748	482.696	19.090	0.010
4663	12 18 50.894	+47 21 00.70	874.317	97.506	19.256	0.010
31187	12 18 51.819	+47 19 56.35	1481.836	637.801	19.298	0.011
35864	12 18 47.198	+47 20 25.75	795.737	734.066	19.309	0.012
51997	12 18 46.957	+47 19 53.17	1034.231	1065.619	19.389	0.010
44141	12 18 47.862	+47 20 02.36	1048.415	903.643	19.574	0.012
6657	12 18 50.314	+47 21 01.32	813.004	139.018	19.577	0.011
41446	12 18 47.622	+47 20 10.24	961.708	847.871	19.594	0.013
4234	12 18 51.396	+47 20 57.28	950.684	89.193	19.625	0.018
3655	12 18 51.193	+47 21 00.35	906.218	76.444	19.657	0.016
8400	12 18 50.221	+47 20 58.51	826.487	173.487	19.677	0.010
45991	12 18 46.740	+47 20 07.89	894.789	942.392	19.694	0.010
4662	12 18 50.548	+47 21 03.66	816.930	97.443	19.699	0.010
20550	12 18 48.903	+47 20 43.91	815.702	420.941	19.715	0.013
27518	12 18 48.969	+47 20 28.55	945.605	562.518	19.832	0.010
57524	12 18 48.801	+47 19 25.55	1435.620	1179.302	19.878	0.011
23751	12 18 48.816	+47 20 37.72	856.961	487.319	19.890	0.011
42544	12 18 48.425	+47 20 00.99	1114.240	870.805	19.913	0.013
7460	12 18 49.568	+47 21 06.00	702.760	155.089	19.918	0.011
3896	12 18 50.963	+47 21 01.74	872.693	81.896	19.925	0.016
10561	12 18 49.443	+47 21 00.47	735.012	218.259	19.937	0.012
4566	12 18 50.618	+47 21 03.22	827.237	95.984	19.991	0.009
22541	12 18 49.572	+47 20 33.95	960.815	461.519	20.052	0.013
14188	12 18 50.626	+47 20 42.79	992.267	290.814	20.057	0.011
695	12 18 52.032	+47 20 59.76	992.657	13.522	20.060	0.011
45068	12 18 48.285	+47 19 56.76	1134.596	922.657	20.150	0.012
8203	12 18 49.034	+47 21 09.03	626.493	169.699	20.212	0.009
42205	12 18 48.214	+47 20 03.52	1073.341	863.826	20.237	0.016
65132	12 18 45.898	+47 19 33.70	1087.567	1338.530	20.275	0.010
12889	12 18 50.029	+47 20 50.58	871.554	265.064	20.293	0.010
36017	12 18 48.265	+47 20 16.35	975.233	736.852	20.295	0.010
15965	12 18 48.742	+47 20 55.00	710.891	327.951	20.448	0.012
2890	12 18 51.222	+47 21 01.68	898.406	61.263	20.467	0.010
57706	12 18 49.091	+47 19 22.73	1486.569	1182.616	20.514	0.013
40960	12 18 44.791	+47 20 35.40	483.976	838.315	20.575	0.009
59832	12 18 44.802	+47 19 54.64	812.577	1227.611	20.609	0.009
59266	12 18 48.736	+47 19 22.40	1454.737	1214.741	20.642	0.010
4044	12 18 50.747	+47 21 03.30	839.175	84.681	20.673	0.010
48800	12 18 46.408	+47 20 04.56	889.228	1001.389	20.750	0.011
36245	12 18 45.236	+47 20 41.70	476.671	741.707	20.830	0.015
64758	12 18 46.901	+47 19 25.91	1247.840	1331.200	20.886	0.010
43584	12 18 43.617	+47 20 39.71	335.074	892.949	21.029	0.010
52996	12 18 45.086	+47 20 06.86	742.139	1087.443	21.039	0.011

Note. — A list of all the secondary sources used calibrate the *F160W* light curves. ID numbers are photometry IDs, X and Y positions are relative to the first epoch of the *F160W* image, and the errors are photometric errors as estimated by DAOPHOT.

catenated to create a master source list of $\sim 1.3 \times 10^5$ entries.

We input this master source list into ALLFRAME. ALLFRAME is similar to ALLSTAR, except that it is capable of performing simultaneous fits to the profiles of all of the stars contained in all of the images of the same field. It then produces time-series PSF photometry as output. We used the master source list as the input for fitting all of the *F160W* epochs at the same time.

We then searched for secondary standards in the star lists by choosing bright objects that had been observed in all twelve of the last *F160W* epochs. We visually inspected the stellar profiles and their surroundings to choose secondary standards that were relatively isolated compared to other bright stars, removing any that showed variability or had large photometric errors. This left us with a total of 44 sources, summarized in Table 3.2. We calculated the celestial coordinates for all of these sources using the astrometric solutions in the FITS headers and PyAstronomy program pyasl. The mean residuals for these stars across all epochs of *F160W* imaging exhibited a dispersion of 0.01 mag which is corrected for during the ALLFRAME photometry.

2.2.4 Aperture Corrections

We use aperture corrections to account for missing flux from imperfections in our PSF model. Using the standard stars chosen for the variability search, we subtract everything but these sources from the master image using the master source list with DAOPHOT's SUB task. The standard stars are already relatively bright and isolated for our field, but this subtraction helps to ensure that we remove any additional flux from the wings of the standard stars. We then perform aperture photometry on the sources using increasing aperture radii (up to 0.4") and check that the growth curves look well behaved over a range of apertures.

We calculated the difference between PSF and 0.4" aperture magnitudes, to which we added the flux beyond this limit previously calculated by STScI. The WFC3 *F160W* Vegamag zeropoint was 24.5037. The overall correction from PSF to "infinite aperture" magnitudes was 0.023 +/- 0.01 mag.

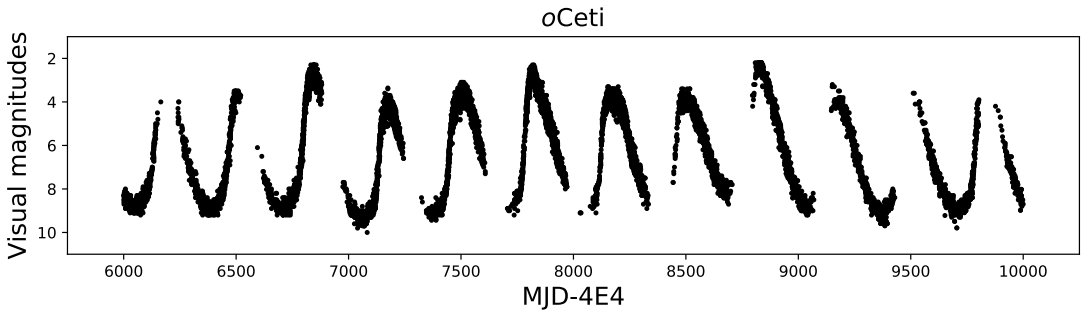

Figure 2.4 Visual light curve of *o*Ceti (Mira) using data from the American Association of Variable Star Observers (AAVSO). The light curve shows cycle-to-cycle variations in both amplitude and mean magnitude.

2.3 Mira Selection Criteria

RR Lyrae, Classical Cepheids, and Type II Cepheids, among other variable stars, can be identified with the use of light curve templates, which exist for both the optical and near-infrared (Jones et al., 1996; Yoachim et al., 2009; Sesar et al., 2010; Inno et al., 2015; Bhardwaj et al., 2017) since the shapes of their light curves vary as function of period in a predictable way. The templates allow them to be identified as a particular class of variable star by light curve morphology after they have been initially identified as variable. However, Miras have irregular light curve shapes that are not strictly a function of period. They may also also exhibit variations in light curve shape or amplitude between different cycles. These cycle-to-cycle variations can be seen in the visual light curve of the prototype Mira, *o*Ceti, shown in Figure 2.4. Figures 7 and 9 of Whitelock et al. (1994) and Figure 1 of Olivier et al. (2001) show the smaller cycle-to-cycle variations present in K-band Mira light curves.

Miras and other long-period variables (LPVs) can also have a longer, secondary pulsational period in addition to their primary pulsational periods. These long secondary periods (LSPs; Payne-Gaposchkin, 1954; Houk, 1963; Nicholls et al., 2009) are typically about an order of magnitude longer than the primary periods (Wood et al., 1999) and are found in about 25-50 percent of all LPVs (Wood et al., 1999; Percy et al., 2004; Soszyński, 2007; Fraser et al., 2008). Several theories have been proposed to explain LSPs, but there is no general consensus (Soszyński, 2007; Saio et al., 2015; Percy & Deibert, 2016). Both LSPs and cycle-to-cycle variations will result in the same Mira having different magnitudes at the same phase in different cycles.

Instead of using template-fitting, Mira variables are typically identified only by their large V and I amplitudes and long periods. The amplitude criterion is used to separate Miras from the more numerous, lower-amplitude, and sometimes more inconsistent semi-regular variables (SRVs), which are another type of LPV (see Figures 2.1 and 2.2). The amplitude cutoffs have traditionally been defined in the optical as $\Delta V > 2.5$ mag or $\Delta I > 0.8$ mag (Kholopov et al., 1985; Soszyński et al., 2009b) and the periods range from 80-1000 days, though there are some Miras with periods that can be significantly longer. A few previous studies also identified Miras in the infrared by using J, H, and K time-series data (Whitelock et al., 2006; **?**; Matsunaga et al., 2009) but large amplitudes in the NIR do not always correspond to large amplitudes in the visible bands. A sample of Miras selected based on large NIR amplitudes could contain objects that would not be selected based on visual criteria and vice versa.

Yuan et al. (2017b) sought to differentiate between these classes of variable stars by using a Random-Forest classifier which incorporated period, light curve shape (O-rich Miras have more symmetric light curves), and other properties into the classification. However, our small number of epochs limits us to using simple cuts. Since we have only limited optical data (at most spanning $\sim 40\%$ of a Mira phase due to the short baseline optimized to detect Cepheids) and only one band in the NIR with time-series photometry, we need selection criteria which rely more heavily on NIR measurements.

We also note that not all Miras are good distance indicators. The two C-rich and O-rich subgroups follow different PLRs in the H-band (Ita et al., 2004; Ita & Matsunaga, 2011). C-rich stars can also develop optically thick circumstellar dust shells that result in them appearing fainter even in the NIR (Yuan et al., 2017b). Therefore, we use only O-rich Miras as distance indicators and must separate them from C-rich Miras.

The photospheric differences between C- and O-rich Miras are thought to be due to the differing ratios of carbon and oxygen in their atmospheres. The carbon and oxygen in a star's atmosphere will combine to make the stable CO molecule until there is no more of the less abundant element. The excess carbon or oxygen will then be left over for dust formation and will combine to create molecules such as TiO and VO in O-rich stars or CN and C_2 in C-rich stars (Cioni et al., 2001). These molecules define each spectral type and can also change a Mira's color, which has potential consequences that are discussed in greater detail in §2.3.4.3. While there are generally $J-K$ distinctions in

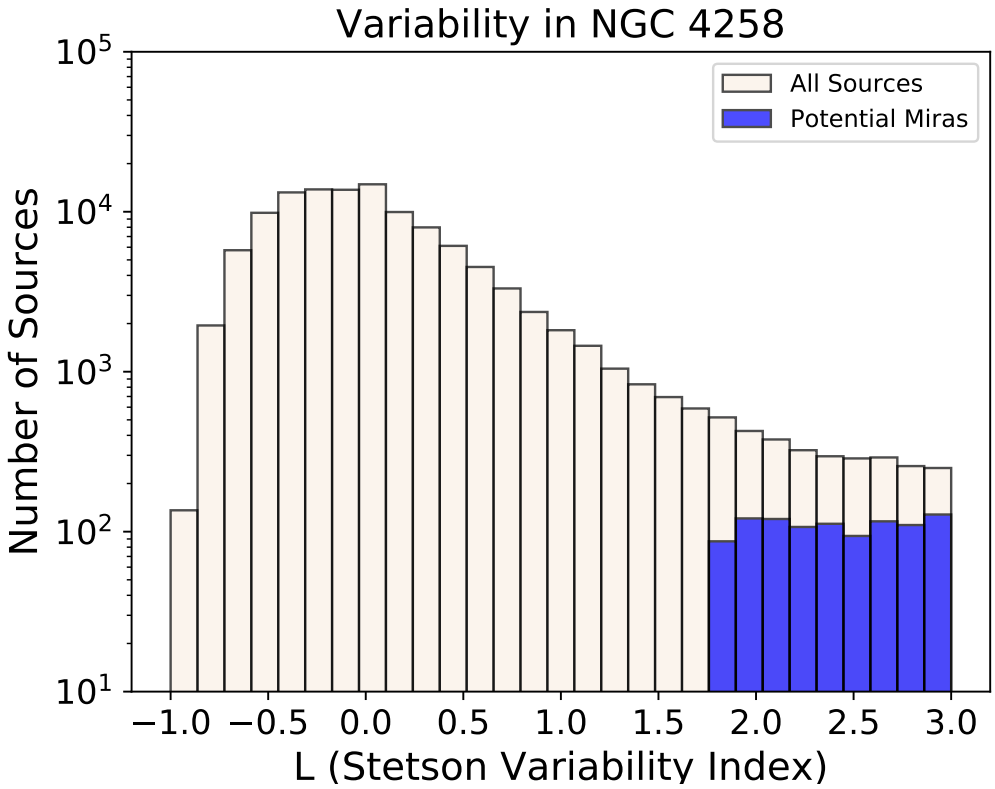

Figure 2.5 The distribution of the Welch-Stetson variability index L for all of the sources in the field (shown in white) and for the subset of objects that made it past the initial visual inspection (in blue). All objects with $L \geq 1.75$ were visually examined and anything that did not pass visual inspection or had $\Delta F160W < 0.4$ was automatically discarded.

color between C- and O-rich stars, the cutoff in color varies in different galaxies (Cioni & Habing, 2003). In addition, some O-rich stars may be very red, as in the case of OH/IR stars.

We expect to encounter a smaller ratio of C-rich Miras to O-rich Miras in NGC 4258 than in the LMC. Higher ratios of O-rich to C-rich stars are observed in galaxies with higher metallicity (Blanco & McCarthy, 1983; Mouhcine & Lançon, 2003; Hamren et al., 2015). The inner field of NGC 4258 is expected to be ~ 0.1 dex more metal-rich than the LMC, though still ~ -0.2 dex relative to solar (Bresolin, 2011).

2.3.1 Detection of Variability

We first used the Welch-Stetson variability index L (Stetson, 1996) to identify a sample of variable objects detected in all of the *F160W* epochs. To do this, we calculated L for every object identified in the master photometry list and then further inspected a

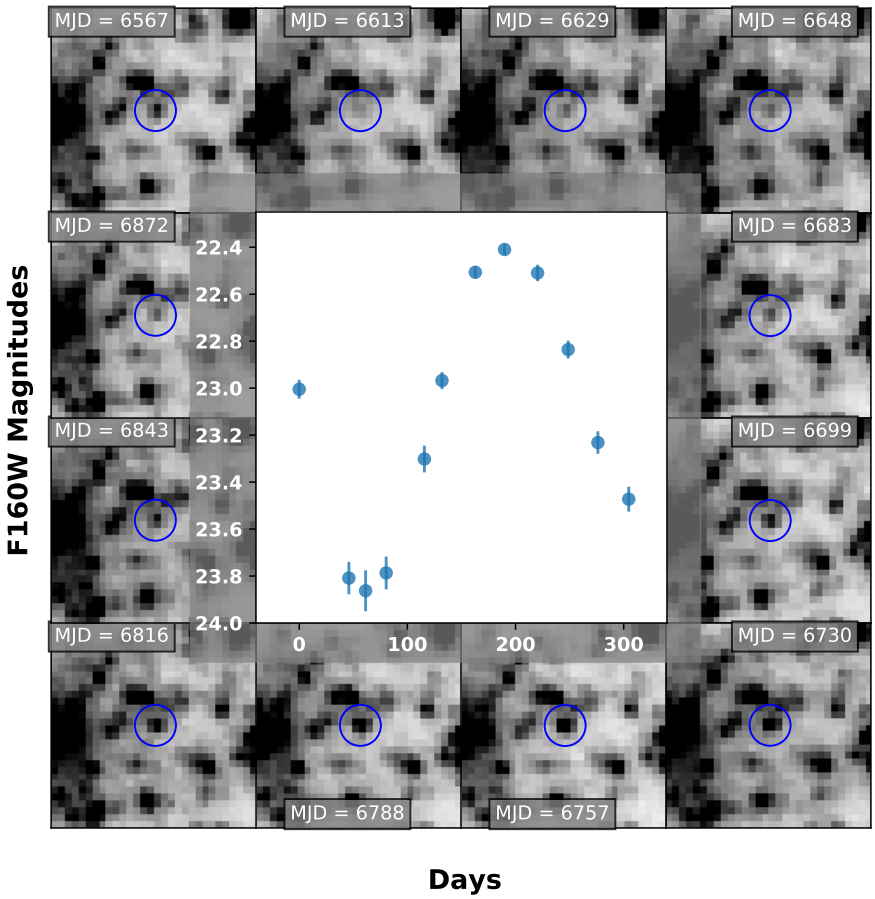

Figure 2.6 Light curve and finding charts for a 266 day Mira from NGC 4258. The Mira is the source in the blue ring in each of the finding charts. Numbers on each stamp represent the date of the observation, corresponding to MJD - 50000. The vertical axis of the inset plot gives the *F160W* magnitude and the horizontal axis marks the time since the first epoch of observations in days. Each stamp corresponds to one point on the light curve, starting in the upper left corner and going clockwise around the image. As the Mira progresses through its light cycle, the brightness of the sources in the postage stamps noticeably changes.

number of objects that met our threshold of $L > 1.75$, about 3σ above the mean L for all objects.

Figure 2.5 shows the distribution of L values for candidate Miras and all sources in NGC 4258. We kept only sources with $L \geq 1.75$ that were detected in all twelve epochs of the most recent *F160W* observations. Sources that did not show periodicity (were only continuously rising or decreasing light curves), had $\Delta F160W < 0.4$ or periods of less than 100 days were then removed from the list of possible Miras. The $\Delta F160W > 0.4$ cut roughly corresponds to the $\Delta I > 0.8$ used by Soszyński et al. (2009b) to distinguish between Miras and SRVs. Additional discussion of the appropriate minimum amplitude cut can be found in §3.2.2. These requirements resulted in 3951 Mira candidates remaining in our sample. An example of an *F160W* Mira light curve and its finding charts is shown in Figure 2.6.

2.3.2 Estimating Cycle-to-Cycle Variation

We estimated the level of cycle-to-cycle variations on the H-band mean magnitude we might measure using data from Matsunaga et al. (2009), which looked at Miras in the Galactic Bulge. These Miras were observed in twelve fields in the NIR between 2001 and 2008, with observations of the same phases during various cycles each Mira. While most of our observations took place over a span of only ~ 300 days, we still need to account for possible variations in magnitude at a given phase between the main *F160W*/H band campaign in 2013 and 2014 and the observations taken in 2009, many oscillation cycles earlier.

We binned the Galactic Bulge data of each Mira candidate observed by Matsunaga et al. (2009) into 30-day bins (to simulate the frequency of our observations) and calculated the H-band mean magnitude in each bin. Next we folded the binned magnitudes by the periods measured in Matsunaga et al. (2009) to obtain their phases. We then binned the resulting points by phase to see how bright each Mira was at that particular phase over different cycles. Finally, we calculated the variance of the points in each phase bin to estimate the cycle-to-cycle variations in magnitude at similar phase for the observations. Figure 2.7 shows the cycle-to-cycle variation of mean magnitudes as a function of Mira period. As expected, the shorter-period Miras have larger 'cycle-to-cycle' variations because each 30-day bin averages over a larger range of phases. The

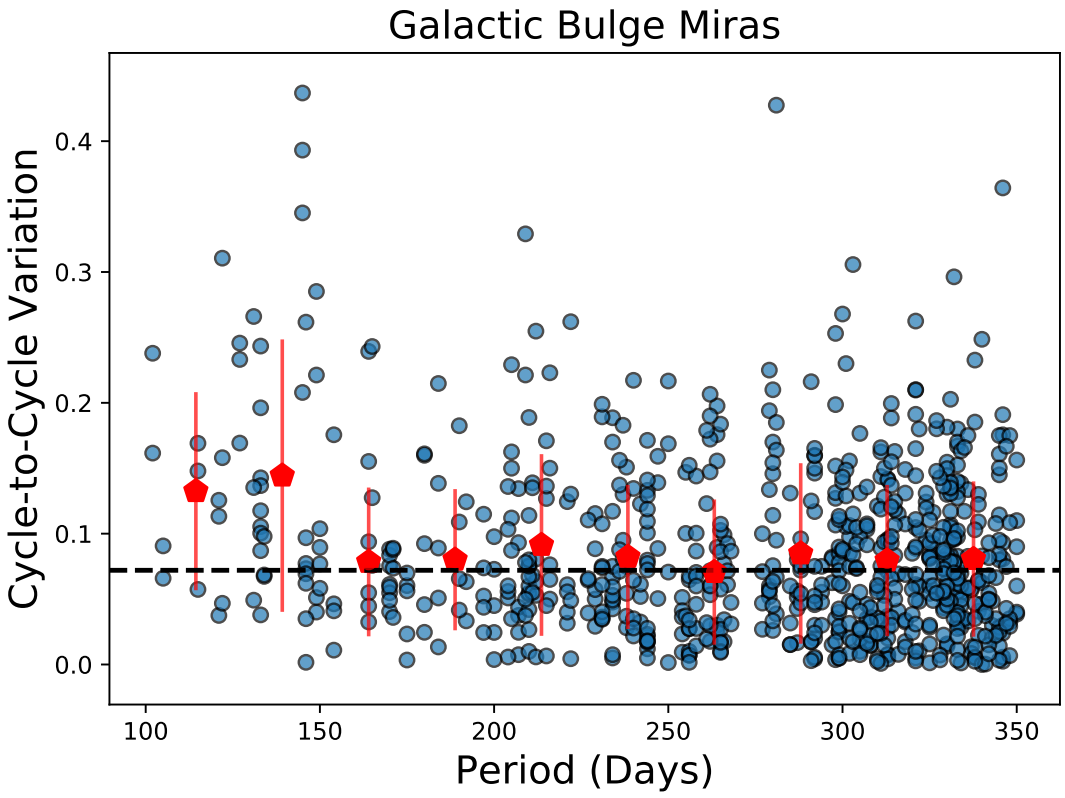

Figure 2.7 Distribution of cycle-to-cycle variations in Galactic Bulge Miras in the H-band using data from Matsunaga et al. (2009). Blue points show the cycle-to-cycle variation for each Mira studied, as a function of the Mira's period, red points are the means of each period bin along with the standard deviations of each bin.

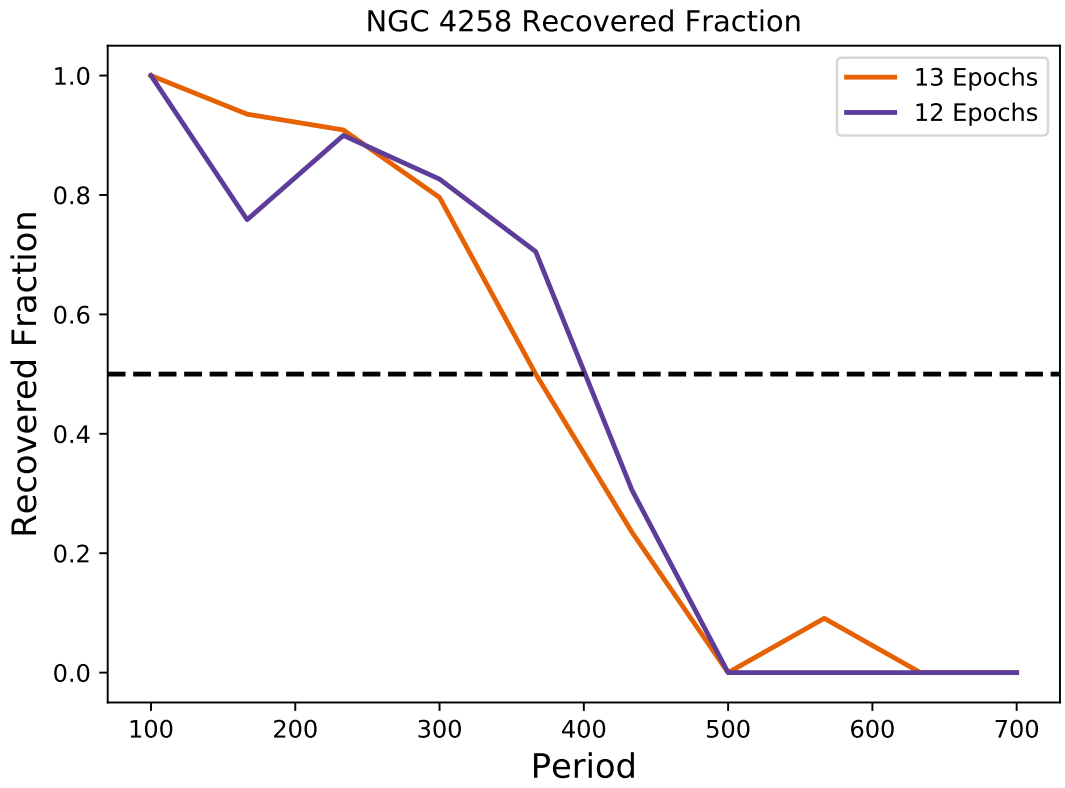

Figure 2.8 The fraction of Mira periods recovered as a function of period. The range of periods for the input Miras (from LMC Mira observations) ranged from 103 to 675 days. Miras were considered 'recovered' if their measured periods were within 30 days of their true periods. A dashed line is shown at a recovery fraction of 0.5 to guide the eye. For the vast majority of our sources, with 13 epochs of observation, the recovery rate $\sim 90\%$.

median cycle-to-cycle variation overall was 0.072 magnitudes, which we incorporated as an additional error added in quadrature when fitting periods using data from different cycles.

2.3.3 Determination of Periods

We used a two-step method to measure the periods of the 3951 Mira-like objects remaining after the previous cuts based on variability and preliminary $\Delta F160W$ amplitude. Unlike the previous steps, which used only the twelve recent epochs of $F160W$ data, we incorporated the additional epochs of observation from 2009 and early 2010 into our analysis at the next stage to get more accurate periods.

First we calculated a Lomb-Scargle periodogram for each variable source. Then the peaks of the Lomb-Scargle were each fit with a Fourier series up to the third order. Well-sampled Mira light curves from the LMC have shown that Miras can have higher order

Table 2.3. Mira Sample Criteria

	Bronze	Silver	Gold
Period Cut:	$P < 300$ days	$P < 300$ days	$P < 300$ days
Amplitude Cut:	$0.4 < \Delta F160W < 0.8$ mag	$0.4 < \Delta F160W < 0.8$ mag	$0.4 < \Delta F160W < 0.8$ mag
Color Cut:	$m_{F125W} - m_{F160W} < 1.3$	$m_{F125W} - m_{F160W} < 1.3$	$m_{F125W} - m_{F160W} < 1.3$
F814W Detection:	–	*F814W* detection	Slope-fit to *F814W* data$> 3\sigma$
F814W Amplitude:	–	–	$\Delta F814W > 0.3$ mag

Note. — The criteria used in selecting each sample of Miras.

harmonics but more could not be fit due to the limited number of available observations. We folded the light curves by each potential period and then fit every folded light curve using a Fourier series. We used a Bayesian information criterion (BIC) to determine if adding another harmonic to the fit was significant before increasing the number of harmonics. Given the limited number of epochs, the BIC indicated that a simple sine function is most appropriate for almost all of the Miras. Finally, we used the Fourier fit parameters and period as initial guesses for a fit to the data using Levenberg-Marquardt least-squares curve-fitting. At this point all of the parameters were fit simultaneously.

To verify that the periods were correct, we visually inspected each $P < 350$ day Mira candidate light curve and checked its fit to a sinusoid using the period determined earlier. Any periods that did not produce a good fit to the data were either refit by removing outliers and overriding the original fit, or, if a good fit could not be found, flagged as a lower-quality object and not used in the analysis.

Since the baseline of our observation was only 305 days, we only have at least one cycle of good phase coverage for Mira candidates with periods less than 305 days. To calculate the period recovery rate, we used LMC Mira observations as templates and added photometric uncertainties and the observation sampling that reflected the NGC 4258 dataset. We tested both the case of 13 epochs of observation (incorporating in the earlier epoch from 2009) and 12 epochs of observation. We then measured the periods of our sample Miras and considered every period measured to within 30 days of the true input period as recovered. For both we found that the recovery rate of Mira periods less than 300 days was approximately 90%. Figure 2.8 shows the results of the simulation.

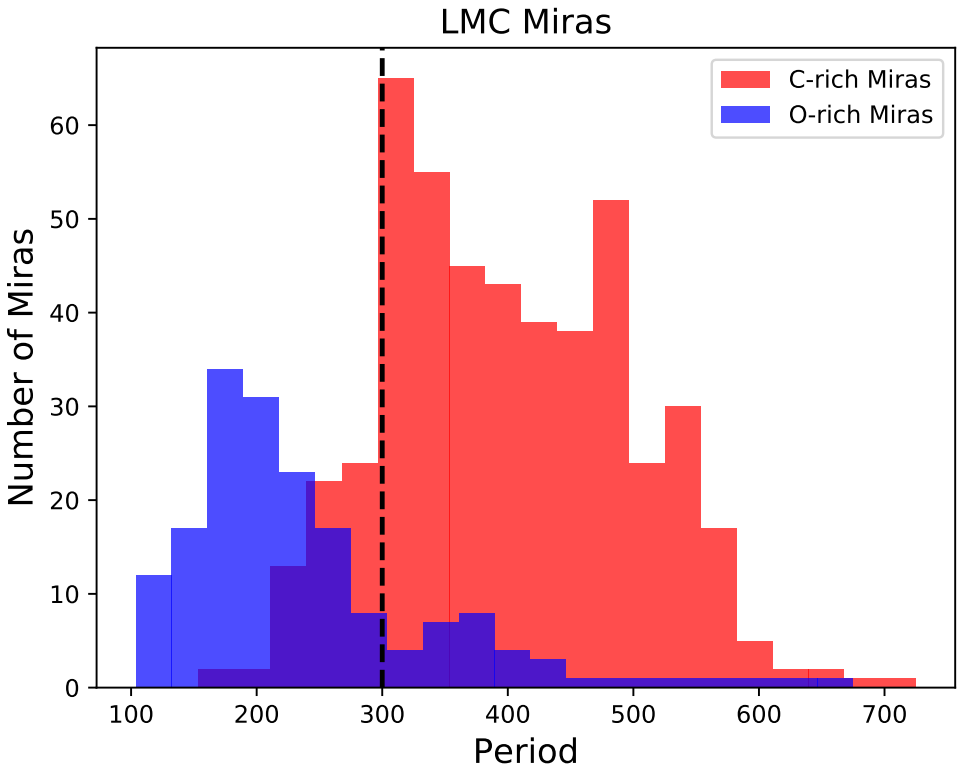

Figure 2.9 The distribution of periods for LMC O- and C-rich Mira variables. C-rich Mira periods are shown in red, the O-rich Mira periods are shown in blue. The black dashed line represents the period cut of 300 days.

2.3.4 Samples and Selection Criteria

Our goal is to recover samples of the most secure Miras, rather than the most Miras, since the statistical uncertainty on the zeropoint of a PL due to our sample size will already be much smaller than the systematic error. We created three samples of Miras, which we have called Gold, Silver, and Bronze based on varying degrees of confidence in classification. Each sample contains predominantly O-rich Miras but the Bronze sample relies only on NIR information for classification, while the Gold and Silver samples are further vetted using our short time series of optical data. This makes the Bronze sample a good test case for future NIR-only observations of Miras. The criteria for each sample are given in Table 3.4. We outline the consequences and motivation for each of these criteria in the following sections.

2.3.4.1 Period Cut

Because the baseline of our observations spanned only 305 days, we kept only Miras with periods less than 300 days. However, this period cut has additional benefits for classification. Applying a cut to the period range also reduces the number of C-rich stars in our sample since C-rich Miras typically have longer periods than O-rich Miras as discussed in §2.3.3 (see Figure 2.2). A distribution of C- and O-rich Mira periods in the LMC is shown in Figure 2.9.

While this period cut will exclude longer-period O-rich Miras, some of these also do not make good distance indicators because they can be hot-bottom-burning stars (HBB). The onset of HBB depends on both mass and metallicity, but it is typically thought to occur in stars with initial masses greater than 4-5 $M_{\odot}$ that are near the end of their AGB phases (Glass & Lloyd Evans, 2003). Whitelock et al. (2003) showed that HBB Miras deviate from a linear PLR, making them poor candidates for distance indicators.

2.3.4.2 F160W Amplitude

Miras have generally been selected on the basis of their large optical (V and I-band) amplitudes to distinguish them from semi-regular variables. Semi-regular variables (SRVs) can be as consistent as Miras in their variability and have similar periods but have smaller amplitudes than Miras. SRVs can also fall on the same PLR as Miras or on various other parallel PL relations (Wood et al., 1999; Trabucchi et al., 2017), depending on their pulsation mode. In general, SRVs are brighter than Miras with the same period and thus can bias the PLR if they are not removed from the final Mira sample. Previous studies of Miras (Matsunaga et al., 2009; Whitelock et al., 2008) have suggested a minimum peak-to-trough variation of ΔJ, ΔH, $\Delta K \sim 0.4$ mag to classify a variable as a Mira. Thus, we have used $\Delta F160W > 0.4$ as the cutoff for minimum change in brightness over one cycle.

In addition to removing SRVs, this minimum amplitude cut also allows us to remove constant stars and blended objects, which would not follow a PLR at all. For a variable star like a Mira or a Cepheid, the resulting blend will have a different color and amplitude from the original star in addition to being more luminous.

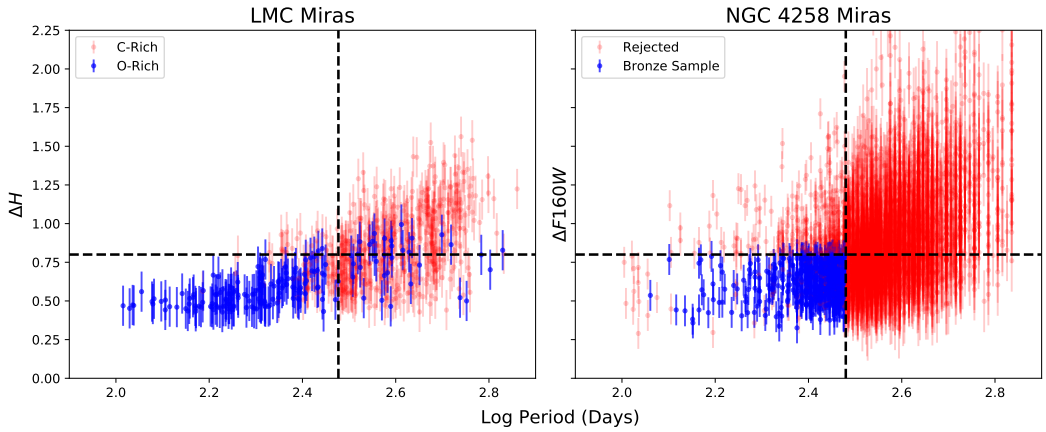

Figure 2.10 **Left**: The amplitude and period relationship for LMC Miras. Red points are C-rich Miras and blue points are O-rich Miras as classified by Soszyński et al. (2009b). They divided the Mira sample along the W_I *vs* W_{JK} plane, where W_I and W_{JK} are Wesenheit indices using optical and NIR magnitudes, respectively. Amplitude information of the LMC Miras comes from (Yuan et al., 2017b) with errors on the amplitude estimated to be ~ 0.13 mag. The dashed vertical and horizontal lines represent the maximum period (300 days) and amplitude (0.8 mag) cuts respectively. Under our selection criterion, only objects within the bottom-left quadrant would have made it into the final Mira sample. **Right**: The same plot constructed for NGC 4258 Miras with the objects in the Bronze Sample in blue, and all the rejected Miras in red. Period and amplitude beyond 300 days are unreliable but have been plotted with their best estimates shown for comparison. Errors on amplitudes greater than 300 days are estimated to be $\sim .2$ magnitudes. Periods below 300 days were verified by visual inspection.

O- and C-rich Miras can also have different amplitude distributions. Cioni et al. (2003) found that C-rich Miras had larger optical amplitudes on average than O-rich Miras in the SMC. Yuan et al. (2017b) found that this was also the case for O-rich Miras in the LMC, especially when considering the amplitude distribution over many cycles. Over the course of a single cycle, C-rich Miras usually have larger amplitudes. This is caused by C-rich Miras having longer periods and thicker dust shells on average compared to O-rich Miras. Both longer-period Miras and heavily reddened stars are more likely to have larger amplitudes. While there is considerable overlap in the distribution of amplitudes for O- and C-rich Miras (as shown in Figure 2.10) the largest-amplitude objects are usually C-rich.

The left half of Figure 2.10 shows the distribution of LMC Miras as a function of period and ΔH using data from Yuan et al. (2017b). These Miras were classified by the OGLE team using a $W_I - W_{JK}$ diagram, where W_I and W_{JK} are the Wesenheit indicies in the optical and NIR, respectively (Madore, 1982). Both types of Miras have estimated uncertainties in amplitude of ~ 0.13 mag but different distributions in amplitude. Since we are interested in obtaining a clean sample of O-rich Miras, we employ a cut of $\Delta F160W < 0.8$ mag as a maximum amplitude cut in addition to the > 0.4 mag minimum amplitude. The corresponding plot of accepted and rejected Miras in NGC 4258 is shown in the right half of Figure 2.10, with our 'Bronze' Miras (Miras that met all of the NIR criteria) shown in blue. Some objects in the same quadrant as the Bronze sample were rejected on the basis of their uncertain periods. However, we expect that there should be a few percent overall contamination from C-rich Miras in this quadrant in the Gold sample.

In the LMC, the ratio of C-to-O Miras in this quadrant is 1/3, and the overall C-to-O ratio in the LMC is 3/1. The C-to-O ratio in the solar neighborhood, which is more similar environment to the inner field of NGC 4258 is ~ 1 (Ishihara et al., 2011). This suggests a $\sim 10\%$ contamination rate from C-rich Miras from using these two cuts alone. Combining these with the optical observations and the color cut which both exclude the reddest objects, we estimate that the contamination in the Gold sample after all of the cuts should be a few percent.

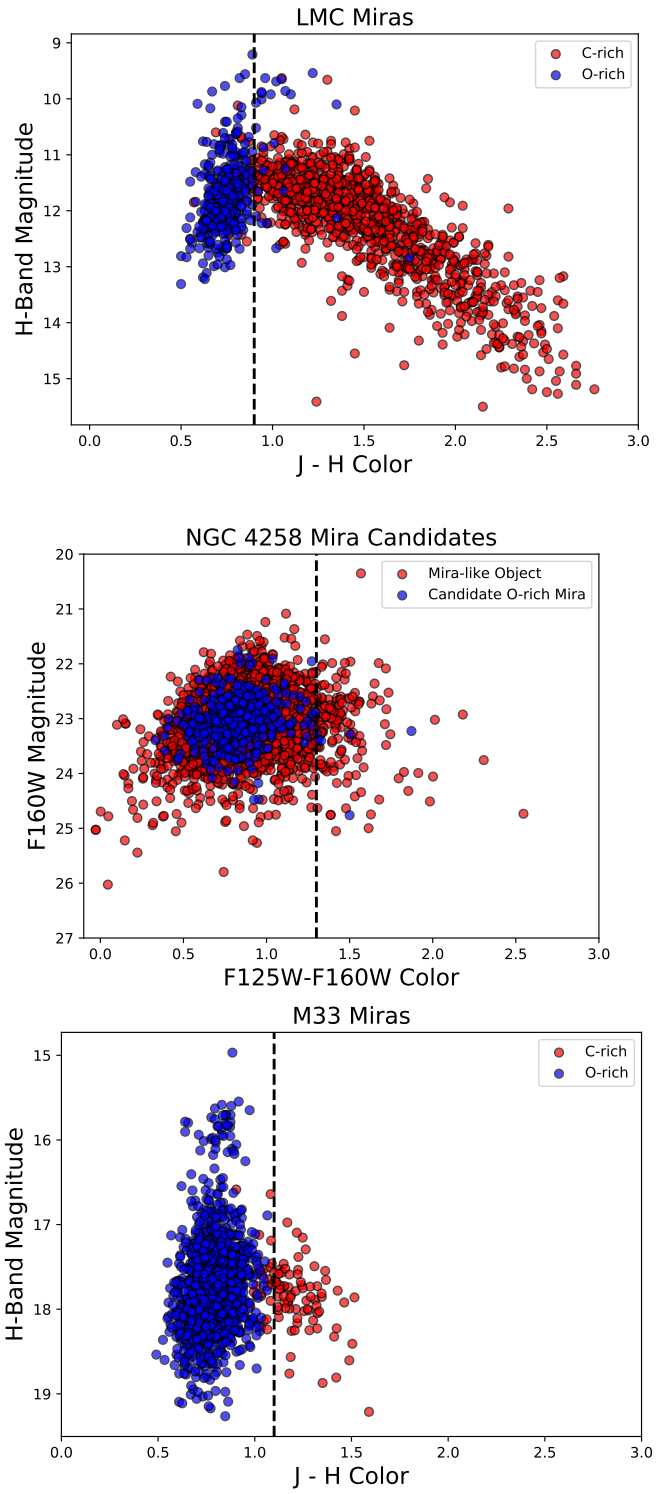

Figure 2.11 **Top**: The color-magnitude diagram for Miras in the LMC made from cross-matching the OGLE-III star catalog with near-infrared data from IRSF. The two subclasses of Miras were classified using a $W_I - W_{JK}$ diagram. The black dashed line is at $J - H = 0.9$. **Middle**: The color-magnitude diagram for Mira candidates in the NGC 4258 made from comparing the mean *F125W* and *F160W* colors. The black dashed line represents $J - H = 1.3$. There are many more bluer variables in the NGC 4258 dataset than in the LMC data set. The 'Candidate O-rich Miras' are objects that have passed all of our NIR cuts except for color. **Bottom**: The color-magnitude diagram for Miras in M33, using UKIRT data from Yuan et al., in preparation. The black dashed line is at $J - H = 1.3$. These Miras were observed from the ground and detected in the optical. C-rich Miras, which are redder, as less likely to have been detected.

2.3.4.3 Color

We calculated the $F125W-F160W$ color by creating a stacked "master" image in each bandpass where each epoch was weighted evenly (despite the first epoch in both bands having a longer observation time). The $F125W-F160W$ color was then measured from the fluxes of the objects in these two images.

Our final NIR cut uses $F125W-F160W$ color. We see that the majority of C-rich Miras can be removed by employing a color cut of $J-H<0.9$, as shown in Figure 2.11 (adopted from Soszyński et al. (2009b)). Color cuts to separate O- and C-rich Miras are physically motivated by the differing opacity in the near-infrared and mid-infrared (MIR) in C- and O-rich stars. It is most effective to use both NIR and MIR colors for distinguishing between the two groups; broad NIR bands alone have not been shown to be sufficient to separate C- and O-rich Miras (Le Bertre et al., 1994). Medium-band filters on *HST* that target unique spectral features have been used to separate C- and O-rich stars in M31 (Boyer et al., 2013, 2017), but are not efficient for identifying Miras in more distant galaxies because they would require much longer integration times.

The J and H filters are also better suited for distinguishing between C- and O-rich Miras than $F125W$ and $F160W$, which are much more similar in their transmission functions. As seen in Figure 2.11, the objects flagged as Mira-like (all objects both red and blue points) in our analysis do not follow the same distribution as the Miras in the LMC. The Mira-like objects in NGC 4258 appear to be one population rather than two seen in the LMC. This is most likely caused by differences in the *HST* filter system and the typical ground-based NIR filters. Stellar models of C- and O-rich AGB stars from Aringer et al. (2009) and Aringer et al. (2016) suggest that these two populations overlap more in $F125W$-$F160W$ color than in J and H color. Some of the reddest objects may also have been undetected.

To avoid cutting through the middle of our population, we used $F125W-F160W<1.3$ mag as a color cut to remove the reddest objects, but anticipated that it would not fully remove C-rich Miras from our sample. We employ the $F160W$ amplitude cuts from §3.2.2 and period cut to remove the majority of C-rich Miras instead.

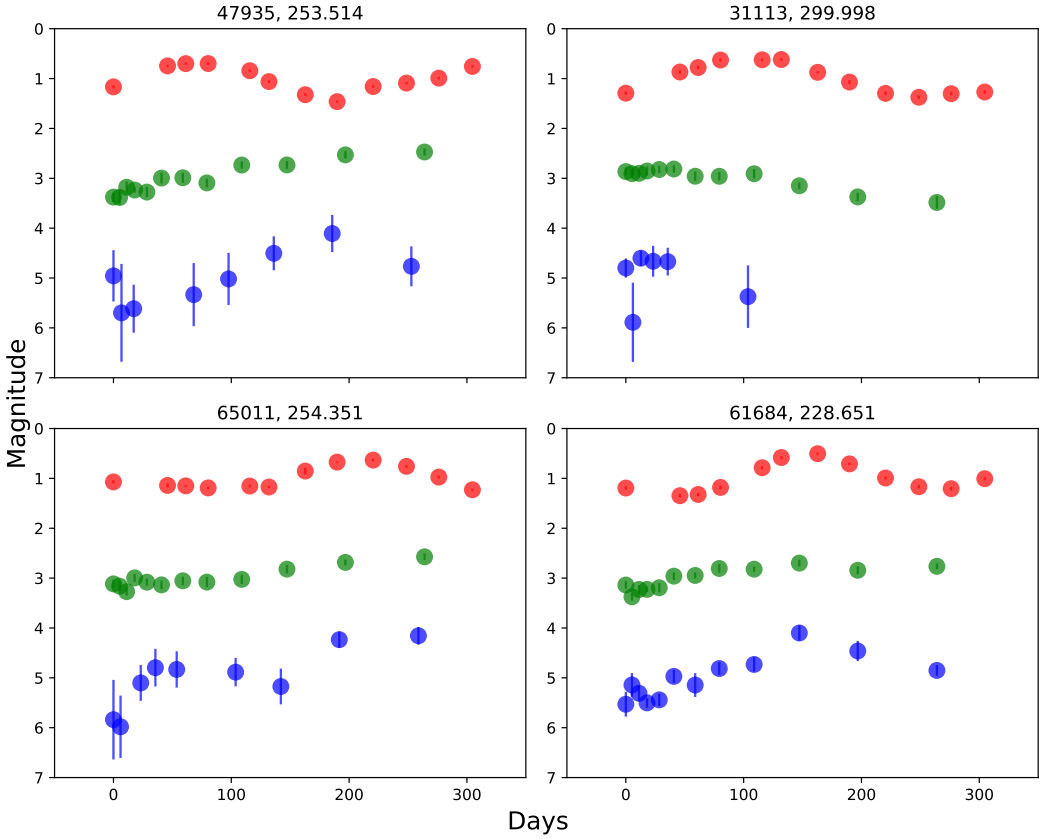

Figure 2.12 The *F160W* (red), *F814W* (green), and *F555W* (blue) light curves for four Mira candidates. The magnitudes have been shifted in order to display every candidate Mira's light curve on the same plot axes and show the amplitude of the light curves. The horizontal axis marks the number of days since the start of each series of observations. The days for the optical light curves have been multiplied by a factor of six in order to better show the shape of the light curves. Numbers at the top of each subplot are photometry ID and calculated period of the object. As can be seen in Table 3.1, we did not have concurrent observations of near-infrared and optical data. Only 35 of the candidate Miras in the Bronze sample had *F555W* light curves. *F555W* data was not included in the analysis, but have been shown here for completeness.

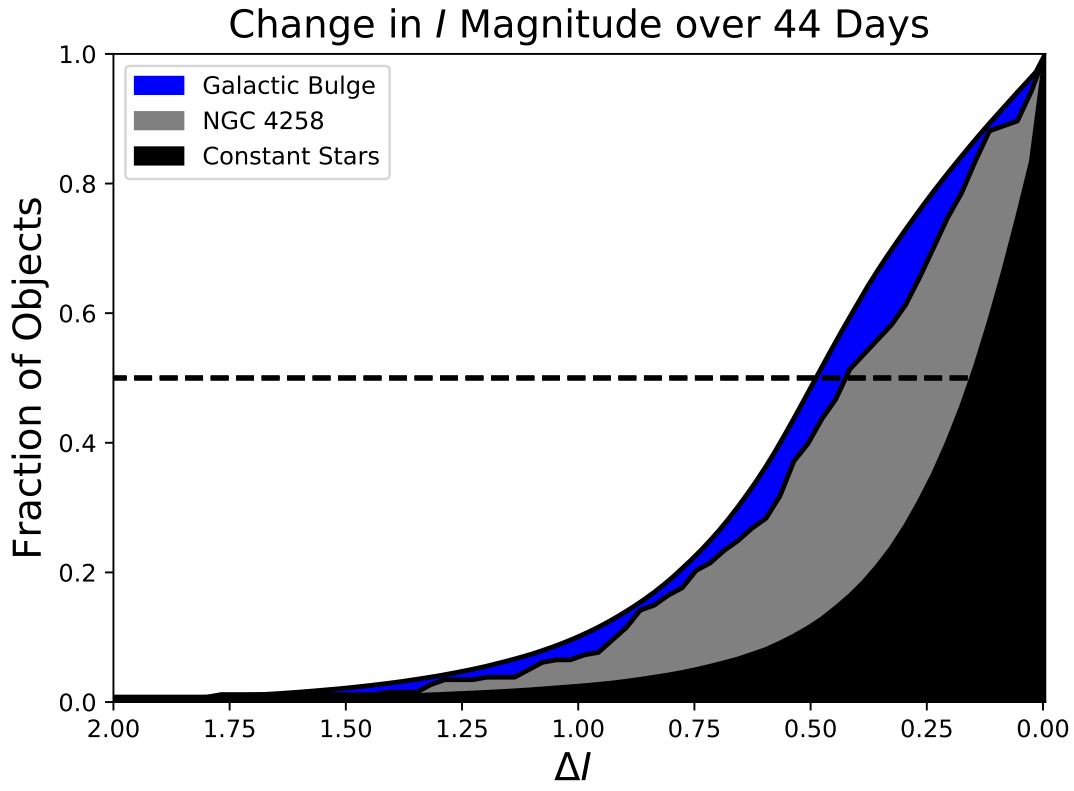

Figure 2.13 The change in I-band magnitude for Miras in the Galactic Bulge (detected with OGLE), Miras in the NGC 4258 Silver sample (248 objects), and constant stars. The three curves show the cumulative distribution for each class of objects as a function of change in I-band magnitude over 44 days (the baseline of our $F814W$ observations.

Table 2.4. Typical Mira Amplitudes and Absolute Magnitudes

Bandpass	Amplitude Range (mag)	Absolute Magnitude (200-Day Mira)
V	2.5- >10	-1.4
I	0.8-3.5	-4.1
J	0.5-3.0	-5.8
H	0.4-3.0	-6.6
K_s	0.4-3.0	-7.0

Note. — The range of amplitudes for Miras and the absolute magnitude of a 200-day Mira in various photometric bands. Upper limits on the amplitudes are approximate. V band absolute magnitudes are not well known and have been estimated from OGLE data (Soszyński et al., 2009b). The other absolute magnitudes are calculated using LMC and M33 PLRs from Yuan et al. (2017a).

2.3.4.4 F555W and F814W amplitudes

In addition to variability, amplitude, and color cuts based on NIR data which were applied to all three samples, we looked for corroborating evidence for the variability of Mira-like objects in *F555W* and *F814W* observations for the Silver and Gold samples. Given photospheric temperatures of only $\sim 3000 - 3500$ K, Miras are significantly less luminous at optical wavelengths. They also experience extremely large-amplitude variations in those bands, with $\Delta V \sim 10$ mag or greater in some cases. Table 2.4 shows a range of amplitudes in different bandpasses and magnitudes for a 200-day Mira.

We estimated the recovery rate of Miras in the optical data. Using the *F160W* observations, we calculated the *F160W* phase at the time of the optical observations and assumed a phase lag between the optical and NIR phases that was dependent on period. The phase lag was calculated using data from Yuan et al. (2017b). We used

$$\phi_I - \phi_H = 2\pi(0.469 - 0.144\log(P)) \tag{2.3.1}$$

where ϕ_I is the I-band phase, ϕ_H is the H-band phase, and P is the period. We assumed that the I and H bands are roughly equivalent in phase to the *F814W* and *F160W*, respectively. We used the estimated differences in mean magnitude and amplitude from Table 2.4 to convert from *F160W* magnitudes and amplitudes to *F555W* and *F814W*. Any stars that had a signal-to-noise ratio greater than 3 were considered recovered in the simulation. This resulted in an expected recovery rate of $\sim 78\%$ for *F814W*.

We used the DAOMATCH and DAOMASTER programs to match the NIR and optical master source lists and found that 296 out of 438 Miras (or 68%) of the Miras from the Bronze sample were matched with sources in *F814W* images. This is roughly in agreement with the simulated expected numbers. As anticipated, very few of our Mira sample could be matched with *F555W* light curves (a 3% recovery rate was predicted by the simulation, compared to 2% in reality). Thus, we used only information from the *F814W* observations in our selection criteria. Light curves for some of the few potential Miras with both *F555W* and *F814W* matches are shown alongside their *F160W* light curves in Figure 2.12. The optical observations precede the NIR epochs by about ten years.

We interpret a Mira's chances of *F814W* detection as a function of both a Mira's

F814W − *F160W* color and phase. We assumed that all of the Miras in the simulation had the same color, but C-rich or heavily dust-enshrouded O-rich Miras are known to be very red and would be difficult to detect in optical bandpasses. Similarly, Miras measured towards the trough of their light cycles would be more difficult to detect than Miras at the peak. However, we were unable to determine our Mira candidates' true phases at the time of the previous observations, so we could not test this directly through simulations.

In order to determine the significance of a change in magnitude over the observation baseline, we fit each *F814W* light curve fragment with a linear fit. We then kept only objects with at least a naive '3σ' significance in change of magnitude in the Gold Sample. This allows us to check that the object we detected as variable in *F160W* is variable in *F814W*.

We also used the difference in magnitude between the first and last epoch of observation to estimate the I-band amplitude. Thus, we could determine if the sources that were variable in *F160W* were also variable in the optical observations. Given that the baseline of the optical observations were only 44 days and the shortest-period Miras have periods of about 100 days, the *F555W* and *F814W* light curves cover only about 15-20% of an average Mira's oscillation and at most contain only about $\sim$ 60% of its total variation. Due to the short temporal baseline of observations, objects close to the peak or trough (if detected) of their observations will be rejected on account of their small overall variations.

We used the OGLE Galactic-Bulge sample of Miras (Soszyński et al., 2013) to calculate the distribution of changes in I band magnitude expected over a period of 44 days. We compared this with the distribution we obtained while looking at the changes in *F814W* magnitude over the same duration baseline for objects in our Silver sample. However, the two bandpasses are not completely identical and their distributions are slightly different, as shown in Figure 2.13. We also created some light curves of constant stars with photometric noise added in as a null case. The Silver sample from NGC 4258 and the Galactic Bulge distribution both show significantly higher levels of I band variation than the simulated "constant" stars over the same period, suggesting that they are true variable stars. The optical requirement also excludes the reddest stars, which are most likely C-rich.

Table 2.5. Final Sample of Miras

ID	Period (Days)	R.A. (J2000.0)	Dec. (J2000.0)	X (Pixels)	Y (Pixels)	Magnitude (F160W mag)	Amplitude ($\Delta F160W$)	Quality
60841	287.015	12 18 47.087	+47 19 32.85	1210.179	1249.445	22.029	0.776	Gold
47935	253.514	12 18 42.138	+47 20 42.89	165.583	983.280	22.918	0.684	Gold
44958	272.561	12 18 43.976	+47 20 33.73	418.105	920.864	22.790	0.712	Gold
24235	292.075	12 18 44.806	+47 21 10.89	200.187	497.320	22.455	0.716	Gold
31113	299.998	12 18 44.585	+47 20 58.19	280.781	636.955	22.539	0.796	Gold
52981	275.948	12 18 42.945	+47 20 25.17	386.517	1087.064	22.523	0.746	Bronze
64439	256.965	12 18 41.148	+47 20 15.63	288.277	1325.193	22.938	0.712	Gold
64343	298.885	12 18 40.925	+47 20 17.73	249.748	1323.194	22.792	0.758	Silver
33823	265.960	12 18 45.165	+47 20 47.61	422.330	690.870	22.681	0.654	Silver
39445	237.358	12 18 42.893	+47 20 54.83	143.229	807.290	22.897	0.798	Gold

Note. — A partial list of Miras is shown here for information regarding form and content.

Table 2.6. Systematic Uncertainties

Systematic	Uncertainty
F160W Amplitude Cut.....	0.042
F160W - *F125W* Color Cut	0.024
Color Correction Term	0.038
Intrinsic Scatter.....	0.021
Total.....	0.06

Note. — The approximate contribution to the total systematic error of the gold sample from each systematic.

2.4 Systematics

In order to get an accurate relative distance and to compare our results with previous studies of Miras using ground-based observations, we needed to transform ground-based H and J magnitudes of LMC Miras into the *HST F160W* magnitude. We performed artificial star tests to account for excess background due to the density of sources in our field and loss of flux due to an imperfect PSF model. Each of these introduces a systematic error into the final result.

To estimate the systematic errors of each of our cuts, we varied each cut around a standard deviation of the values chosen or the range of values present in the literature when possible and looked at the effect that it had on the zeropoint of the PLR relation. Table 2.6 has a summary of each of these contributions.

2.4.1 Slope

Miras and other variable stars are typically fit with a linear Period-Luminosity Relation (called the Leavitt Law for Cepheids). However, there is some evidence for break at 10 days for Cepheids and previous Mira observations have suggested that the Mira PLR may have a break as well, at periods of about 400 days (Ita & Matsunaga, 2011). This is likely to be caused by the onset of HBB.

Yuan et al. (2017a) used a quadratic fit for the Period-Luminosity relation instead of fitting the sample with two linear PLRs with a break. We fit each of our subsamples of Miras using their quadratic PL relations for the H band, which is the closest match to *F160W*:

$$m = a_0 - 3.59(\log P - 2.3) - 3.40(\log P - 2.3)^2 \tag{2.4.1}$$

where P is the period in days, m is the H-band magnitude, and a_0 is what we have called the zeropoint. We fit for a_0 and hold the other parameters fixed to the values from Yuan et al. (2017a).

This PLR was derived using observations of about 170 LMC O-rich Miras. While the *F160W* filter is bluer than the H band, deriving a PLR from the NGC 4258 data alone was not possible because of the much larger scatter induced by the background brightness fluctuations, which is discussed in great detail in §2.4.2. With observations of Miras in more galaxies using *F160W*, we could simultaneously fit the Miras in multiple galaxies and derive a more robust fit in this bandpass.

2.4.2 Artificial Star Tests

The high density of sources and unresolved background objects in our images will systematically bias our magnitude measurements towards brighter values. This is caused by the superposition of several point sources. We refer to this effect as crowding.

We correct for crowding using artificial star tests. Starting with a master image created from combining all twelve epochs of *F160W* data, we use DAOPHOT to place fake sources in the images at the same apparent magnitude as the Mira candidates. We then compare the recovered magnitudes of the artificial stars with the input magnitudes and adjust the input magnitudes to better agree with the recovered magnitudes. On

average, the artificial stars were measured to be 0.25 magnitudes more luminous than their true magnitudes.

We then repeat the steps in the photometry process up to the creation of the master source list and then compare the recovered and input magnitudes to determine the crowding correction. Because there are $\sim$ 1700 variables in the image, we add in one fake star for *half* of the variable stars in the image at any given time to avoid artificially raising the background of the image. The artificial stars are dropped within a 25-pixel radius of each Mira, and at least 10 pixels away from the edges of the image. Only stars that did not fall within 3 pixels of another star up to 1.5 magnitudes fainter were used in the analysis.

After calculating the difference in the input and recovered magnitudes, we then use a three sigma-clip about the median to remove outliers. The mean difference between input and recovered magnitude for each star is then the crowding correction we apply.

2.4.3 Mean Magnitude Correction

We used OGLE O-rich Miras cross-matched with J and H magnitudes from the Infrared Survey Facility (IRSF) catalogue (Kato et al., 2007) to determine the LMC zeropoint. The mean magnitudes for NGC 4258 were defined as the first term in the Fourier-series fit to each object. Because Mira light curves are irregular in shape, they do not spend the same amount of time at each phase in their cycles, creating a small bias in single-epoch measurements when compared to mean magnitudes.

We used Monte Carlo simulations to calculate the difference between these two estimates of mean magnitude and found that on average, the PLRs measured using the fit mean magnitudes were 0.02 fainter than the PLRs measured using single-epoch mean magnitudes. Therefore, in order to correct between the two, we added in a mean magnitude correction of -0.02 mag to our final results.

2.5 Results

2.5.1 Color Transformation

In order to compare ground-based NIR PLRs with the *F160W* PLR from NGC 4258, we calculated a color correction to transform the ground-based H band Mira observa-

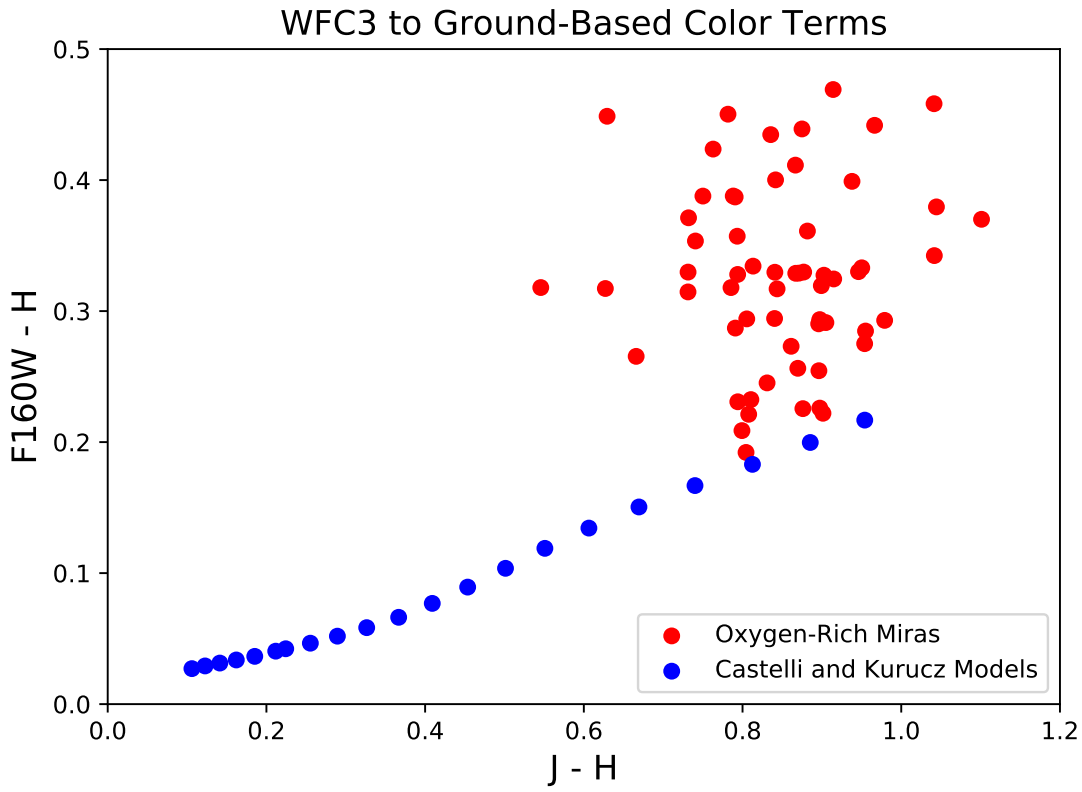

Figure 2.14 Non-linear color term for the *F160W* - *H* transformation as a function of $J - H$ color. The blue points represent calculations using Castelli & Kurucz (2004) models with $3500 < T < 7000$, $\log g = 0.1$ and solar metallicity. The red points are based on observed spectra of O-rich Miras. Note that neither set of points has a constant color coefficient as a function of color. The mean of the red points is 0.39, which we adopt for our transformations.

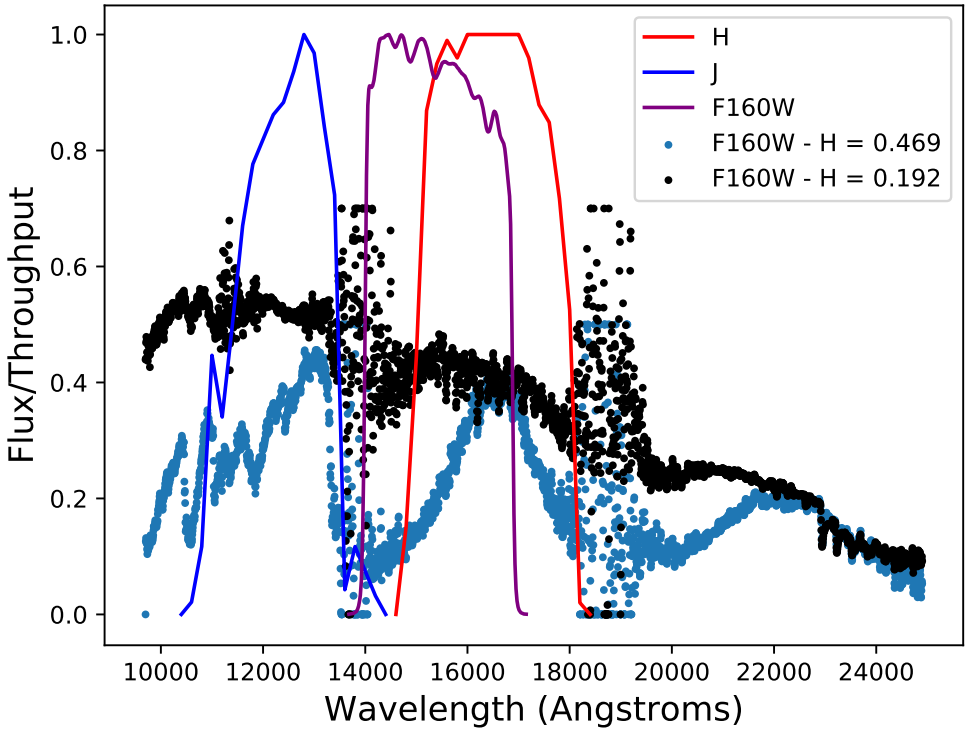

Figure 2.15 The reddest and bluest O-rich Mira spectra in used to calculate the color correction (very red OH/IR stars were excluded) are shown in blue and black respectively with ground-based J and H filters and *HST* WFC3 *F160W*. The filters have been normalized to have a peak throughput of 1. The difference in color appears to be the result of a combination of both the continuum emission and the much stronger absorption lines in the redder spectrum.

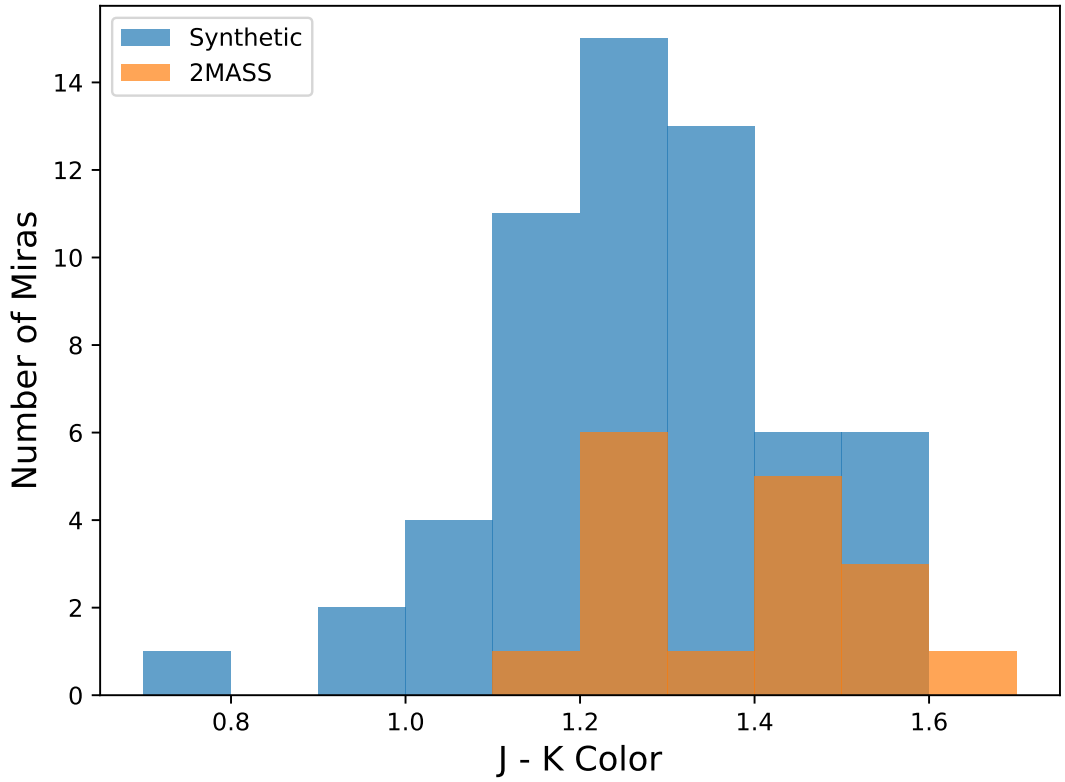

Figure 2.16 A comparison of the $J-K$ color derived synthetically using PySynPhot and $J-K$ colors from 2MASS. Most of the objects in the Galactic sample of Miras were observed at more than one part of their light cycle and thus had synthetic colors that varied by $\sim$ 0.15 magnitudes. The synthetic colors had an overall standard deviation of 0.19 magnitudes whereas the 2MASS colors had a standard deviation of 0.14 magnitudes.

tions to *F160W* observations. Miras have heavy molecular absorption lines in the NIR compared to M-type main sequence stars so we used real O-rich Mira NIR spectra observed from the ground from Lançon & Wood (2000) as input to PySynPhot to derive the transformations for Miras specifically (STScI Development Team, 2013).

This resulted in an H to *F160W* transformation of:

$$F160W = H + 0.39(J - H) \tag{2.5.1}$$

This is a significantly larger color term than was found for the bluer Cepheids (0.16) in R16. This difference is due to the non-linearity of the color term, shown in Figure 2.14. Because Cepheids are much bluer than Miras (a typical Cepheid is an F star), and the color term is non-linear, we must use a different color transformation of Miras. Using the same color term to transform from H to *F160W* for Miras as we used for Cepheids would result in a ~ 0.18 mag difference for an average O-rich Mira with a $J - H$ color of 0.8. The ground-based spectra are affected by the telluric absorption bands, as seen in Figure 2.15. Water bands dominate the near infrared spectra of O-rich Miras, and these are difficult to separate from telluric features in ground-based observations.

Because the O-rich Miras we used to calculate the color transformation displayed a large scatter in *F160W* - H color, we also examined spectra of individual Miras that were particularly blue or red to check that the spectra were calibrated well enough for synthetic photometry. We found that very red Miras had much larger absorption features (the result of having more dust) than very blue Miras. Additionally, we compared the measured $J - K$ colors of the O-rich Miras in the 2MASS catalog to the $J - K$ colors derived synthetically (Figure 2.16). We found that for individual Miras, the two were in agreement and the standard deviation of the two distributions of color (0.19 from spectrophotometry and 0.14 from 2MASS measurements) was also similar. The 2MASS colors were on average slightly redder (by ~ 0.1 magnitudes), suggesting that the true color correction might be slightly larger. However, the distribution in Mira color appears to be real and not the result of poor calibration.

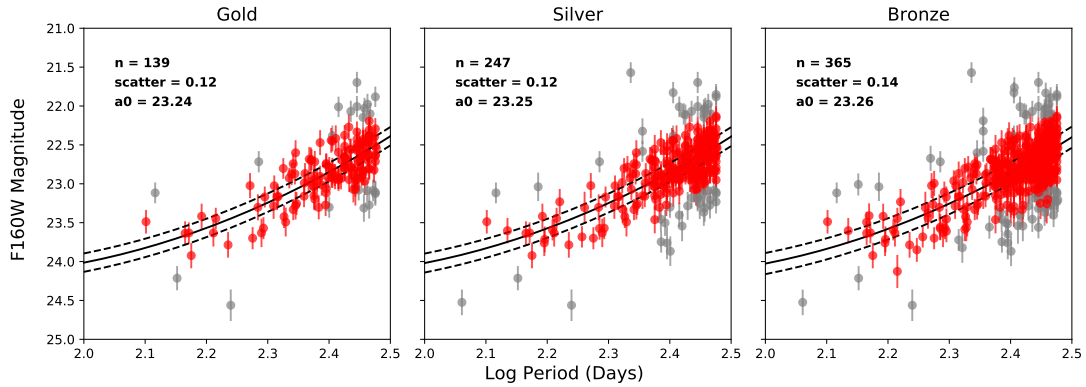

Figure 2.17 Mira Period-Luminosity relations for the Gold, Silver, and Bronze subsamples (left, center, and right, respectively). Red points denote objects used in the final fit, white gray points represent variables that were removed through iterative 3σ clipping. The solid black curves show the best-fit relations, while the dashed lines denote the 1σ scatter (0.11, 0.13, 0.14 $\sim$ mag respectively).

2.5.2 Mira Samples

We created three subsets of Mira candidates based on our estimate of their reliability as distance indicators and the possibility of contamination, applying the cuts discussed described in Table 3.4. For our Gold sample of Mira candidates, we had a total final sample size of 161 objects. Fitting these objects to the PL relation derived by Yuan et al. (2017a) for the H band gave us a zeropoint of $a_0 = 23.24 \pm 0.01$ mag. The sigma clipping removed 22, $\sim 14\%$ of the Gold sample Mira candidates from the final PLR, leaving a total of 139 Mira candidates remaining.

For the larger Silver sample, we had a final sample size of 296 and determined $a_0 = 23.25 \pm 0.01$ mag for this sample. After sigma clipping, which removed 48 objects, $\sim 16\%$ of the Mira candidates, leaving 248 remaining for the fit.

Finally, the Bronze sample consisted of 438 objects and had a zeropoint of $a_0 = 23.25 \pm 0.01$ mag. We sigma-clipped out 72 Mira candidates, $\sim 16\%$, comparable to the amount removed in the Silver sample. The PLR for each sample is shown in Figure 2.17.

Despite the different selection criteria, the zeropoints of all of the samples are almost the same and the fraction of their outliers is also consistent. This is especially important for the Bronze sample, which used only NIR criteria. It suggests that future studies can also be successful with only NIR *HST* data to select Miras.

2.5.3 Relative Distance to the LMC

We compared our results in NGC 4258 with a sample of O-rich Miras discovered in the LMC by the OGLE survey (Soszyński et al., 2009b) to determine the relative distance modulus between these two galaxies. We obtained random-phase J and H magnitudes for the LMC variables from the IRSF catalog of Kato et al. (2007). We used Equation 3 to transform these into the equivalent *F160W* magnitudes, which were fit with the PLR of Equation 2.4.1 to solve for the zeropoint. The difference between the NGC 4258 and LMC zeropoints yields the relative distance modulus (not corrected for small differences in foreground extinction between the two galaxies).

Using the Gold sample defined in the previous section, we calculated a distance modulus relative to the LMC of $\Delta\mu_g = 10.95 \pm 0.01_r \pm 0.06_{sys}$ using Miras from the OGLE survey. For the Silver sample, we have $\Delta\mu_s = 10.97 \pm 0.01_r \pm 0.07_{sys}$, and for the Bronze sample, $\Delta\mu_b = 10.97 \pm 0.01_r \pm 0.08_{sys}$. These are consistent with a previous measurement of the Cepheid relative distance modulus from R16, $\Delta\mu_{R16} = 10.92 \pm 0.02$.

In order for the Cepheid scale to agree with the Planck results, it would need to be too short by $\sim 0.20\mu$. If we consider Miras an independent cross-check on the Cepheid distances and assume that the Cepheid relative distance modulus should be 10.95 ± 0.07, then we find that a true relative distance modulus of 10.75 ± 0.07 is ruled out by 2.4σ. This suggests that the Cepheid and Mira distance scales both have some tension with the Planck results.

Finally, we also used the color transformation from §2.5.1 to derive the PLR coefficients for an *F160W*-band PLR using the ground J and H-band relations from Yuan et al. (2017b). We then refit the PLRs for for both the LMC and NGC 4258 and found that these two methods yield marginal differences in the results.

2.5.4 Absolute Calibration to NGC 4258

We use the improved megamaser distance to NGC 4258 from R16 of 29.387 ± 0.057 mag. The uncertainty in the Humphreys et al. (2013) value was reduced to 2.6% from 3% by increasing the number of Monte Carlo Markov Chain (MCMC) trial values in the analysis by a factor of a hundred. Using this distance modulus puts the absolute calibration of the PLR for the Gold sample at $a_0 = -6.15 \pm 0.09$ mag in the *F160W*

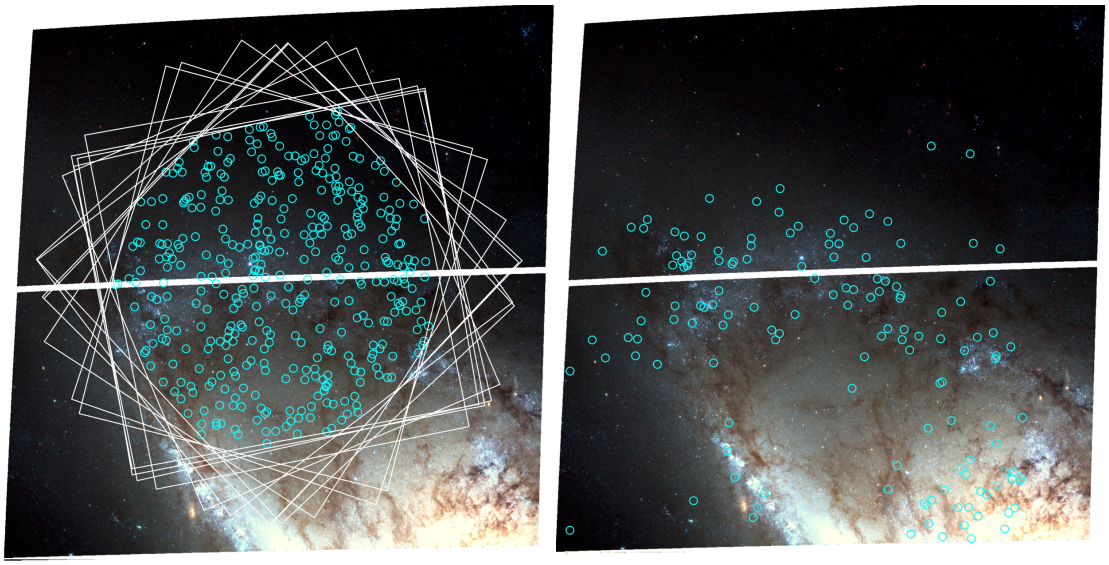

Figure 2.18 **Left:** The locations of the Bronze sample Miras (cyan circles) in in the NGC 4258 ACS inner field. The white regions show the *F160W* footprint. Because our observations were taken over the course of one year, the orientation changed in each observation, leaving an approximately circular area that was observed in all epochs. We searched in this region only for Miras. **Right:** Cepheids (cyan circles) from Macri et al. (2006) on top of the same ACS field. The Cepheid distribution traces the spiral arms of the galaxy while the Miras are more common and can be found evenly across the smaller *F160W* footprint.

bandpass.

2.5.5 Spatial Distribution

As a sanity check, we compared the spatial distributions of our Bronze Mira candidate sample with the spatial distribution of Cepheids in NGC 4258. Figure 2.18 shows the locations of Cepheids and Miras in the galaxy overlaid with the *F160W* footprints. The Cepheids trace the spiral arm of the galaxy while the Miras are found randomly distributed in the *F160W* footprint. These differences in spatial distribution have a physical origin in the progenitors of Cepheids and Miras. Cepheids, with their intermediate and high-mass progenitors, are young stars that are only found in regions with active star formation. Thus, they are present in the denser spiral arms of a galaxy and are part of the disk population. Almost all Miras have progenitors of low-to-intermediate mass, which therefore have intermediate-to-old ages and can exist in areas without re-

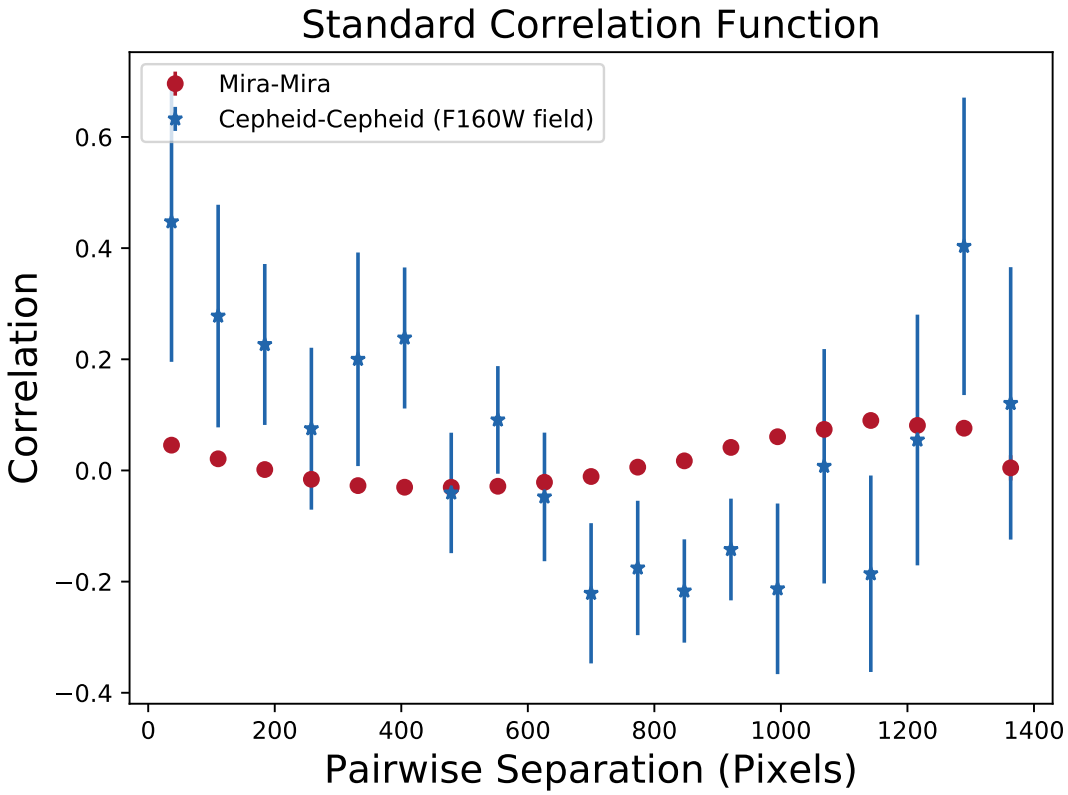

Figure 2.19 The Cepheid-Cepheid and Mira-Mira standard correlation function. in the NGC 4258 *F160W* field. Errors are obtained through bootstrap resampling. Cepheids are blue, the Miras in red. Due to the small sample of Cepheids (84) compared to Miras (438), the errors for the Cepheid-Cepheid autocorrelation functions are much larger.

cent star formation. For our sample limited to short-period Miras only, this is especially true, since the progenitor stars will all be of low mass. Miras can additionally be found in both the disk and halo populations.

We calculated the autocorrelation functions for both Cepheids and Miras in the *F160W* footprint shown in Figure 2.18. The autocorrelation function for Miras discovered in this project and the Cepheids discovered by Macri et al. (2006) is shown in Figure 2.19. The Cepheid and Mira autocorrelation functions follow different distributions, with the Mira autocorrelation being much flatter, as expected for evenly distributed objects. The results confirm that the two distributions are different spatially, and agree with what we would expect from a physical understanding of Mira and Cepheid progenitors.

2.6 Discussion

The largest source of uncertainty in local measurements of H_0 remains the number of SNe Ia host galaxies that have been calibrated with Cepheid distances. A 200-day Mira is roughly comparable in *F160W* brightness to a 30-day Cepheid, allowing them to be observed to approximately the same volume. SNe Ia used in R16 all have modern photometry, low reddening ($A_V < 0.5$ mag), and observations prior to peak luminosity. Additionally, only late-type host galaxies were targeted to ensure the presence of Cepheids. Using Miras over Cepheids would increase the number of SN host galaxies for cross-calibration and eliminate potential biases caused by host galaxy morphology.

Since Miras are an older population star they can be found in most galaxies regardless of host galaxy morphology. This can help us create a sample of cross-calibrators that is more representative of the Hubble flow SNe Ia sample. Rejkuba (2004) was able to derive a K-band Mira PLR for the giant elliptical galaxy NGC 5128, which would have been an unlikely target as an SNe Ia calibrator host. Miras are also part of the halo population so we can also potentially look for Miras in hosts that are not face-on, further increasing the number of potential targets.

In the future we will be able to further reduce our uncertainties in the relative distance by directly comparing measurements of Miras observed in the *HST* NIR with our calibrated PLRs from NGC 4258. In addition, by using the same criteria and filters we can help ensure that we selected for the same classes of objects. The consistency of

the results between the Bronze, Silver, and Gold samples also demonstrates that Miras can we conduct this search without optical data.

2.7 Conclusions

1. We discovered 438 Mira candidates in one field of NGC 4258 using only the *HST F160W* bandpass.

2. We developed criteria to reduce contamination from C-rich Miras in our sample that do not use spectroscopic information and found that amplitude cuts can help separate C- and O-rich Miras. This allows us to discover and characterize Mira candidates using solely or primarily *F160W*.

3. We determined a relative distance modulus between NGC 4258 and the Large Magellanic Cloud based on Mira variables of $\Delta\mu_g = 10.95 \pm 0.01_r \pm 0.06_{sys}$, which is consistent with the Cepheid relative distance modulus and also consistent with the relative distance modulus obtained using geometric methods.

4. We have calibrated the extragalactic Mira distance ladder in *F160W* using the geometric distance to NGC 4258.

5. We derived a Mira-specific color transformation from the ground-based H-band to the *HST F160W*.

2.8 Acknowledgments

We acknowledge with thanks the *o*Ceti observations from the AAVSO International Database contributed by observers worldwide and used in this research. PAW acknowledges a research grant from the South African National Research Foundation. We would also like to thank Drs. Yoshifusa Ita, Noriyuki Matsunaga, Gregory Sloan, Martha Boyer, Steven McDonald, Daniel Shafer, and Sjoert van Velzen for their helpful discussions.

Chapter 3

HST Observations of Miras in Type Ia SN Host NGC 1559, An Alternative Candle to Measure the Hubble Constant

One of the most intriguing issues in observational cosmology is the discrepancy between the Hubble Constant (H_0) measured in the present-day Universe using the Cepheid-supernovae distance ladder (Riess et al., 2016, hereafter, R16) and gravitational lensing time delays (Bonvin et al., 2017; Wong et al., 2019) and the one inferred from the early Universe using the cosmic microwave background (CMB) data assuming a ΛCDM cosmology (Planck Collaboration et al., 2018). Combining independent *SH0ES* (Riess et al., 2019, hereafter, R19) and H0LiCOW measurements (for a recent review, see Verde et al. (2019) and sources within), the difference is at the 5.3σ confidence level. Despite increasing attention, it appears difficult to explain the discrepancy as being caused by a single error in any specific measurement (Addison et al., 2018; Aylor et al., 2019). The persistence of the tension has led to the possibility of additions to ΛCDM as an explanation (Poulin et al., 2018), but the standard of proof for new physics is high, and alternative routes to the present measurements should be explored.

Independent distance indicators such as highly-evolved Mira variable stars and the Tip of the Red Giant Branch (TRGB) (Jang & Lee, 2017; Freedman et al., 2019; Yuan

et al., 2019) can help provide a check of local Cepheid distances. They can also increase the number of local Type Ia supernovae (SNe Ia) used as calibrators. Though evolved, Cepheids have massive progenitors and are thus relatively young stars, so *HST* searches for such variables in local SNe hosts target nearby, globally star-forming, late-type galaxies with modest inclination. Miras have absolute magnitudes comparable to those of Cepheids in the near-infrared (NIR) and can be seen out to the same volume, allowing them to fulfill a role in the distance scale similar to that of Cepheids, as calibrators of SNe Ia. Unlike Cepheids, short-period ($P < 400$ days) Miras have low-mass progenitors and are present in all galaxy morphologies (Boyer et al., 2017; Whitelock & Feast, 2014; Rejkuba, 2004). Miras can also be found in the halos of galaxies, removing the need for low-inclination hosts. The ubiquity of Miras makes them a potentially attractive tool to calibrate SNe Ia in all galaxy types.

Though Miras were the first pulsating variable stars discovered (over 400 yr ago), they remain relatively underused as a distance indicator. They are asymptotic giant branch (AGB) stars that pulsate in the fundamental mode with periods ranging from $\sim$ 100 days on the short end to greater than 2000 days for the longest-period objects. They have amplitude greater than 2.5 mag in the V band, the largest of any regular pulsator (Soszynski et al., 2005). Miras were suggested to have Period–Luminosity Relations (PLRs) by Gerasimovic (1928), but the scatter in visual magnitudes at a given period was large ($\sim$ 0.5 mag), as summarized by Feast et al. (1989). Later studies (Robertson & Feast, 1981) using observations in the NIR found a much tighter PLR, suggesting that they could be promising distance indicators at longer wavelengths. They are typically divided into two subclasses, oxygen-rich (O-rich) and carbon-rich (C-rich) (Kleinmann & Payne-Gaposchkin, 1979, see Ita & Matsunaga (2011) for comparisons of their PLRs). The O-rich Miras follow a well-defined PLR at IR wavelengths, while the C-rich Miras fall fainter than the PLR in the optical and NIR, likely owing to circumstellar reddening. However, corrected for reddening, or at longer wavelengths such as the K band (2.2 μm), C-rich Miras and O-rich Miras follow a similar PLR (Ishihara et al., 2011; Whitelock et al., 2003).

Host-galaxy metallicity affects Miras in several ways. Galaxies with higher metallicity exhibit larger ratios of O-to-C-rich Miras (Boyer et al., 2017; Hamren et al., 2015; Battinelli & Demers, 2005). In addition, O-rich Miras with more massive progenitors

($\sim 3\,M_{\odot}$; $P \gtrsim 400$ days) can experience hot-bottom-burning (HBB) (Whitelock et al., 2003; Marigo et al., 2017). HBB stars are brighter at their period range than would be predicted from a linear PLR fit to shorter-period objects. Though there is no consensus on the details of HBB, the onset of HBB is known to have a dependency on both mass (and thus period, since more-massive Miras have longer periods) and metallicity. Therefore, for distance measurements, selecting Miras with $P < 400$ days removes the known metallicity dependences of the Mira PLR.

Miras are not as commonly used as distance indicators as Cepheids or TRGB because obtaining the necessary observations has been more difficult. Years-long baseline observations are necessary in order to obtain accurate measurements of their periods. Furthermore, they do not follow tight PLRs in the optical — only in the IR — and these observations are more difficult to obtain from the ground. Mira light curves can be observed in the optical to obtain accurate period measurements, but still need IR follow-up observations in order to produce useful PLRs.

Until recently, calibrating their luminosities has also been challenging. Previous studies of Miras have used the Large Magellanic Cloud (LMC; Soszyński et al., 2013; Ita et al., 2004; Feast et al., 1989) and M33 (Yuan et al., 2017a) to calibrate the luminosity of these stars. Whitelock et al. (2008) showed using Hipparcos parallaxes that the PLR for Galactic Miras is consistent with that in the LMC. Individual parallaxes in the Milky Way are more difficult to measure than for most stars because the angular sizes of Miras are larger than their parallaxes (their physical sizes are larger than 1 au). In addition, they typically have time-variable asymmetries (Paladini et al., 2017) that have been speculated to result from giant convection cells (Lattanzi et al., 1997) or caused by nonradial pulsations. Even with *Gaia*, obtaining Mira parallaxes may only be possible with later data releases that can properly account for movement of the photocenter and the resolved profiles of these sources (Whitelock, 2018).

In our previous paper (Huang et al., 2018, hereafter, H18), we addressed the issue of calibration by searching for Miras in the water megamaser host galaxy NGC 4258. In addition to providing us with the farthest Miras to have measured luminosities and periods, the host galaxy's water megamaser allowed for a geometric distance with 2.6% precision (R16; Humphreys et al. 2013). This enabled us to obtain an absolute calibration for the Mira distance scale on the *HST* system of filters. These results were in

Table 3.1. *HST*-GO 15145 Observations Used in this Work

Epoch	Orientation (deg)	MJD	UT Date
01	160.6	58005.2	2017-09-08
02	160.6	58015.8	2017-09-19
03	−165.4	58037.6	2017-10-11
04	−165.4	58049.3	2017-10-22
05	−124.4	58084.9	2017-11-27
06	−78.6	58142.2	2018-01-23
07	−18.1	58199.3	2018-03-21
08	36.6	58256.2	2018-05-17
09	90.3	58314.6	2018-07-15
10	160.6	58372.8	2018-09-11

Note. — The WFC3/IR camera and *F160W* filter were used for each observation. The exposure time of each epoch was 1006 s. The orientiation is the angle east of north of the y-axis of each image.

agreement with the LMC Mira calibration of Yuan et al. (2017b). The maser distance of NGC 4258 has recently improved to 1.5% precision, adding more precision to this calibration (Reid et al., 2019).

In this paper, we present the Mira-based distance of NGC 1559, the first SN Ia host to have such a distance, yielding the first Mira-based calibration of the luminosity of SNe Ia. It is the first of four local SN Ia hosts in which we are searching for Miras with *HST*. In Section 3.1 we describe the observations, data reduction, and photometry. The selection criteria for Miras are discussed in 3.2. In Section 3.3 we characterize the systematic uncertainties. We present and discuss the main result in Section 3.4 and conclude in Section 3.5. Throughout the paper we use "amplitude" to refer to the total (peak-to-trough) variation of a variable star light curve over the course of one cycle.

3.1 Observations, Data Reduction, and Photometry

3.1.1 Observations and Data Reduction

This study uses ten epochs of *HST* WFC3/IR *F160W* data (GO-15145; PI Riess), with an exposure time of 1006 s for each epoch. The observations are also designed to measure Cepheid variables found using epochs of optical imaging (Miras are too red to appear in the optical images). The epochs have an approximately monthly cadence between 2017 September 8 and 2018 September 11, with a field of view centered at $\alpha = 04^{\rm h}17^{\rm m}37^{\rm s}$ and $\delta = -62^\circ47'00''$ (J2000). Table 3.1 contains the observational information for each

Table 3.2. Secondary Standards

ID	α (J2000)	δ (J2000)	X (pixels)	Y (pixels)	$F160W$ (mag)	Uncertainty (mag)
7599	$04^h17^m40.019^s$	-62°46′17.51″	843.0	203.9	18.939	0.081
10534	04 17 34.146	-62 46 41.15	461.3	280.8	19.039	0.078
4002	04 17 31.105	-62 46 26.79	335.7	111.1	19.195	0.070
25011	04 17 37.447	-62 47 23.13	525.8	673.1	19.238	0.093
10962	04 17 39.975	-62 46 28.86	809.8	292.5	19.355	0.104
8924	04 17 37.077	-62 46 28.90	653.0	238.8	19.381	0.060
25548	04 17 32.556	-62 47 36.57	225.1	687.9	19.433	0.066
16153	04 17 39.255	-62 46 48.42	717.8	433.2	19.466	0.107
4308	04 17 29.008	-62 46 32.80	206.1	119.5	19.684	0.070
31503	04 17 41.974	-62 47 34.16	740.5	844.3	19.789	0.083
25269	04 17 37.822	-62 47 23.10	546.2	679.8	19.823	0.050
11364	04 17 38.388	-62 46 34.00	710.0	303.5	19.895	0.052
5369	04 17 40.051	-62 46 10.18	864.6	146.8	19.986	0.074
24951	04 17 44.680	-62 47 05.78	963.8	671.1	20.022	0.064
7243	04 17 38.170	-62 46 20.78	734.1	195.2	20.168	0.075
29515	04 17 41.245	-62 47 29.25	714.4	791.0	20.193	0.111
26819	04 17 32.001	-62 47 42.17	179.9	721.8	20.195	0.064
25967	04 17 42.801	-62 47 13.83	840.4	699.5	20.236	0.166
31273	04 17 35.870	-62 47 47.77	373.8	837.8	20.236	0.077
1510	04 17 34.915	-62 46 09.25	589.4	43.7	20.242	0.057
35832	04 17 43.821	-62 47 43.95	813.7	955.8	20.265	0.094
23326	04 17 42.191	-62 47 06.19	828.2	627.9	20.282	0.055
29323	04 17 32.986	-62 47 48.13	216.9	787.1	20.325	0.059
30041	04 17 34.260	-62 47 47.51	287.5	805.9	20.659	0.109
27599	04 17 37.056	-62 47 32.79	478.5	741.9	20.690	0.082
27351	04 17 34.181	-62 47 38.82	306.8	735.9	20.702	0.067
28149	04 17 33.826	-62 47 42.35	278.0	757.1	20.778	0.078
35037	04 17 39.297	-62 47 51.99	547.5	934.9	20.803	0.063
9301	04 17 29.739	-62 46 47.50	205.8	248.9	20.835	0.075
5013	04 17 40.445	-62 46 08.02	891.7	137.1	20.932	0.067
6365	04 17 38.468	-62 46 17.28	759.7	173.2	21.021	0.059

Note. — All of the secondary sources used to calibrate the *F160W* light curves. ID numbers are photometry IDs. The X and Y positions are relative to the first epoch of the *F160W* image, and the uncertainties are photometric errors as estimated by `DAOPHOT`. The magnitudes are calculated as explained in Eq. 3.1.2.

epoch.

We use pipeline-calibrated images retrieved from the *HST* MAST Archive. We generate pixel-resampled and stacked images for each epoch using `Drizzlepac 2.2.2` (Gonzaga, 2012). Each epoch contains two subpixel dither positions and has been resampled to a scale of 0.12″ pix^{-1} (WFC3 has a native scale of 0.128″ pix^{-1}) and the orientation of the images rotates by slightly over a full rotation as a consequence of *HST* orient constraints. We choose the first epoch as the reference image and align all of the subsequent images with it using `DrizzlePac`.

3.1.2 Photometry and Calibration

We begin by stacking all of the *F160W* observations to make a deeper "master" image. This image is used to create a master source list for the photometry. Given the crowded nature of our fields, we use the crowded-field photometry packages `DAOPHOT/ALLSTAR` (Stetson, 1987) and `ALLFRAME` (Stetson, 1994) for the data reduction and source extraction. Our procedure closely follows the steps used to search for Miras in the water megamaser host NGC 4258 (H18).

The `DAOPHOT` routine `FIND` is used to detect sources with a $> 3\sigma$ significance. The signficance depends on sky background, readout noise, the number of images combined and averaged (we only combined). Then the `DAOPHOT` routine `PHOT` is used to perform aperture photometry. We input the star list produced from the aperture photometry into `ALLSTAR` for point-spread-function (PSF) photometry, optimized for a 2.5 pixel full-width at half-maximum intensity (FWHM). We then repeat these steps on the star-subtracted image generated by `ALLSTAR` (with all of the previously-discovered sources removed) to produce a second source list. The two source lists are then concatenated and used as input into another round of `ALLSTAR` (applied to the image without subtracted sources) to create a final master source list of $\sim$ 49,000 objects.

This master source list is input into `ALLFRAME`. We use the master source list to derive a consistent source list for PSF photometry of each *F160W* epoch. `ALLFRAME` is similar to `ALLSTAR`, except that it is capable of simultaneously fitting the profiles of all sources across the full baseline of epochs for a single field. This allows it to maintain a constant source list through multiple epochs and improves the photometry for stars closer to the detection limit. `ALLFRAME` produces time-series PSF photometry as output.

Secondary standards are used to correct for variations in the photometry of constant sources (detector and image quality) between different epochs. We search for secondary standards in the star lists by choosing bright objects that were observed in all ten *F160W* epochs. Their stellar profiles and surroundings were visually inspected to choose secondary standards that are relatively isolated compared to other stars in the image, removing any that showed variability or had large photometric errors. This leaves us with a total of 31 sources, summarized in Table 3.2. We calculate the celestial coordinates for all of these sources using the astrometric solutions in the FITS headers.

Photometry is conducted on the resampled images. The mean residuals for these stars across all epochs of *F160W* imaging exhibited a dispersion of 0.01 mag. We use this to correct the `ALLFRAME` photometry for epoch-dependent variations.

To put our observations on the same zeropoint as H18, which we adopt for an absolute calibration of distance, we use the same *HST* WFC3 IR photometric zeropoint for a 0.4″-radius aperture. In Vega magnitudes, the *F160W* zeropoint is 24.5037 mag. The use of a consistent zeropoint in a fixed aperture where we normalize the flux of the PSF compensates for small differences on the observing pattern, PSF, and resampling scale between NGC 4258 and NGC 1559. In NGC 4258, the observations of each epoch consisted of four subpixel dithers. This allowed us to drizzle images for each epoch to a finer scale in NGC 4258 (0.08″ pix^{-1}) than in NGC 1559 (0.12″ pix^{-1}), where we only have two subpixel dithers per epoch.

To define aperture corrections to the PSF, we select the brightest and most isolated stars in the field that are not saturated. These are often foreground stars, unlike secondary standards, which are chosen to be closer in expected magnitude to our variables. These stars are used to determine the correction from the PSF magnitude to the 0.4″ aperture magnitude only, not as photometric standards.

We subtract all other stars in the master source image from the image using `DAOPHOT/SUBSTAR` to create a "clean" image. Aperture photometry is then performed on the bright stars in the clean image using 10 apertures ranging from 1 to 5 pixels to create a growth curve. We inspect the growth curve of each of the stars used in the aperture corrections and reject any stars that do not have smooth, monotonically increasing growth curves. The aperture correction is defined as

$$\Delta m_{\rm ac} = m_{\rm ap} - m_{\rm PSF}, \tag{3.1.1}$$

where $m_{\rm ap}$ is the aperture magnitude for an aperture with a radius of 3.3 pixels, equivalent to the 0.4″ aperture zeropoint, and $m_{\rm PSF}$ is the PSF magnitude. We find an aperture correction of $0.023 \pm +/- 0.01$ magnitudes, which we add to $m_{\rm PSF}$ to correct to the *HST* zeropoint for a 0.4″ aperture. PSF photometry is used throughout our analysis, and the aperture correction is included at the end to put our old and new observations on the same *HST* zeropoint. The aperture correction may change slightly

between the observations of NGC 4258 and NGC 1559 owing to "breathing" and small focus changes. Because we do not have standard stars in common between our two fields, we cannot correct for this effect, which is estimated to be ~ 0.01 mag, so we include this in the uncertainty. Thus, including the aperture correction, we convert from instrumental magnitudes to calibrated magnitudes using

$$m_f = m_i - 2.5\log(t) - a_{\rm DAO} + a_{\rm HST} + \Delta m_{\rm ac} + \Delta m_b, \tag{3.1.2}$$

where m_f is the final calibrated magnitude, m_i is the instrumental magnitude output from `DAOPHOT` photometry, t is the exposure time, $a_{\rm DAO}$ is the `DAOPHOT` photometric zeropoint (25.0 mag), $a_{\rm HST}$ is the *HST* zeropoint for a $0.4''$ aperture (24.504 mag), $\Delta m_{\rm ac}$ is the aperture correction (0.06 mag), and Δm_b is the crowding bias correction (mean value of 0.13 mag) discussed in §3.2.4.

3.2 Mira Selection Criteria

Light-curve templates are typically used to identify and classify variable stars. Classical Cepheids, RR Lyrae stars, and Type II Cepheids all have distinctive light-curve shapes, and templates for these objects exist in both the optical and the NIR (Jones et al., 1996; Yoachim et al., 2009; Sesar et al., 2010; Inno et al., 2015; Bhardwaj et al., 2017). However, unlike most other variable stars that have been used as distances indicators, Miras do not have a homogeneous light-curve shape. In addition, both the shape and magnitude at a given phase of Mira light curves are known to vary between cycles, though these variations are smaller at NIR wavelengths (Whitelock et al., 1994; Olivier et al., 2001; Yuan et al., 2017b). Therefore, a sine function has been used to fit NIR Mira light curves in previous studies (Matsunaga et al., 2009). Here we also use a single sine function to fit the periodicity, and the amplitude of the sine to classify the variables. While the amplitude may change in subsequent cycles, the period remains more consistent, so a sine fit still allows us to capture the periodicity.

We use a number of steps to identify Miras and separate candidates from other types of Long-Period Variables (LPVs) and non-variable stars, including the Stetson variability index L, period, amplitude, and an approximate F-statistic. All of the candidate variables that pass these criteria are also visually inspected to remove any potential noisy

Table 3.3. Final Sample of Miras in NGC 1559

ID	Period (days)	α (J2000)	δ (J2000)	X (pixels)	Y (pixels)	Magnitude ($F160W$ mag)	Uncertainty ($F160W$ mag)	Ampli (Δ $F1$
300258	374.586	$04^h17^m36.487^s$	-62°46′00.66″	697.660	5.385	24.250	0.153	0.6
816	344.937	04 17 37.056	-62 46 01.59	725.941	23.264	24.302	0.163	0.6
300938	272.999	04 17 34.200	-62 46 08.26	553.360	22.640	24.749	0.176	0.6
934	339.024	04 17 32.541	-62 46 12.72	451.567	26.954	25.159	0.184	0.6
1372	260.733	04 17 37.048	-62 46 03.75	719.626	40.124	24.328	0.270	0.7
1423	240.849	04 17 28.711	-62 46 23.70	214.651	42.213	24.118	0.178	0.6
301623	295.503	04 17 37.568	-62 46 03.07	749.607	44.512	25.016	0.253	0.5
1964	263.733	04 17 34.958	-62 46 10.78	587.545	56.643	24.359	0.473	0.4
1606	310.348	04 17 30.305	-62 46 20.60	309.246	47.456	24.363	0.145	0.4
2227	347.314	04 17 33.852	-62 46 14.37	517.991	64.354	24.607	0.183	0.6
2640	381.497	04 17 38.749	-62 46 04.18	810.458	75.226	22.735	0.169	0.5
303038	337.114	04 17 32.496	-62 46 19.88	429.738	82.513	25.765	0.160	0.7
303532	319.410	04 17 31.855	-62 46 22.97	386.645	94.986	24.882	0.216	0.6
3973	272.939	04 17 36.615	-62 46 13.59	669.508	109.656	24.565	0.372	0.6
3626	251.081	04 17 30.908	-62 46 25.97	327.299	101.019	25.140	0.261	0.6
4015	326.046	04 17 38.073	-62 46 10.34	757.175	111.162	24.673	0.363	0.4
4099	267.813	04 17 38.127	-62 46 10.41	759.922	112.767	24.921	0.484	0.4
304685	254.121	04 17 37.465	-62 46 13.60	715.432	125.538	23.670	0.485	0.5
304909	328.070	04 17 28.879	-62 46 34.53	194.400	130.754	24.537	0.216	0.5
5985	257.784	04 17 28.723	-62 46 39.15	173.463	164.217	24.462	0.215	0.5

Note. — A partial list of Miras is shown here for information regarding form and content. The final magnitudes are consistent v
3.1.2. In order to fit the PLR we also applied an extinction correction of −0.01 mag and a C-rich contamination correction of −0.0
To obtain the magnitudes in Figure 3.9, add −0.065 mag to the magnitude column of this table.

stars or non-variable contaminants. In addition, use information about the local environment of the candidate Miras — surface brightness and crowding bias corrections — to determine if they are reliable sources not dominated by background flux. Finally, we use simulations (described in Section 3.2.6) to test the efficacy of our selection criteria.

The final sample after applying all of our selection criteria outlined in §3.2.1, §3.2.2, §3.2.3, and §3.2.4 is shown in Table 3.3.

3.2.1 Variability and Period Determination

The first step in our Mira selection process is calculating the Welch-Stetson variability index L of all of the objects in our field (Stetson, 1996). This index is only used to weed out as many nonvariable stars as possible before beginning the later parts of the search, as many objects with high variability indexes may still be non-Miras, short-period variables, or simply nonvariable stars with noisy measurements. We use a cutoff for the minimum variability index of $L \geq 0.75$, consistent with the criterion H18 used for NGC 4258. With simulations, we find that this variability cut removes $\sim 90\%$ of the nonvariable stars. Figure 3.1 shows a distribution of the L index for all of the stars

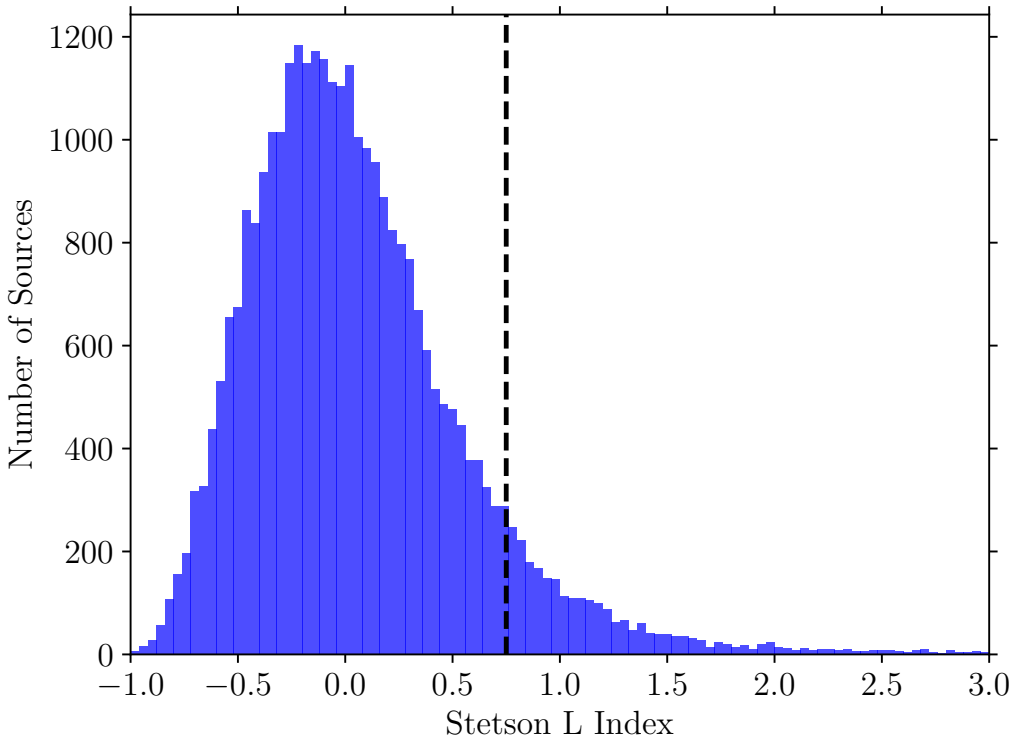

Figure 3.1 The distribution of the Stetson L index for all of the objects detected in the master image in ten epochs of observations. We began the variability search by examining objects with $L \geq 0.75$, indicated in the plot by the black dashed line. There were $\sim 49,000$ objects in the master list and $\sim 25,000$ with 10 epochs of observations.

Table 3.4. Mira Sample Criteria

	NGC 1559	NGC 4258 (gold)
Period Cut (days):	$240 < P < 400$	$P < 300$
Amplitude Cut (mag):	$0.4 < \Delta F160W < 0.8$	$0. < \Delta F160W < 0.8$
Surface Brightness Cut:	421 counts/second	—
F-statistic:	$\chi^2_s/\chi^2_l < 0.5$	—
Color Cut (mag):	—	$m_{F125W} - m_{F160W} < 1.3$
$F814W$ Detection:	—	Slope-fit to $F814W$ data$> 3\sigma$
$F814W$ Amplitude (mag):	—	$\Delta F814W > 0.3$

Note. — A comparison of the criteria for the final Mira samples in NGC 1559 and NGC 4258. Owing to differences in signal-to-noise ratio and the available data, we were unable to match the criteria exactly.

we detect in our master image. Approximately 3000 variable-star candidates remain at this stage.

Next, we calculate the most likely period (assuming the variability is periodic) of the remaining candidates. For each, we perform a grid search on periods ranging from 100 to 1000 days, the relevant period range for Miras. At each period we fit the light curve in magnitude space with a sine function with the amplitude, mean magnitude, and phase as free parameters using a χ^2 minimization, as done by H18. In addition, the mean magnitude from the sine fit is used as the mean magnitude of the Mira for fitting the PLR in both this paper and H18, giving us a consistent definition of mean magnitude. The period with the lowest χ^2 fit to a sine is then chosen as the best-estimate period of the Mira. As our observation baseline spanned ~ 370 days, and the shortest-period Miras we can effectively use in our PLR relations have $P = 240$ days (see §3.3), we would not see aliasing in our period estimations. Our observation timing is such that each Mira in our period range is sampled at least five phases per cycle.

3.2.2 Recovery of Mira Parameters

Following H18, we consider only variables in the amplitude range $0.4 < A < 0.8$ mag to be candidate O-rich Miras. The minimum amplitude removes semiregular variables (SRVs) from our sample, which typically have smaller amplitudes (Soszyński et al., 2013), or heavily-blended Mira stars, which will be artificially bright and have reduced amplitudes by their blending with a constant contaminant. The maximum amplitude is used to limit the number of heavily reddened C-rich Miras in our sample, which have on

average larger amplitudes than O-rich Miras with the same period range. While C-rich Miras with low reddening track the O-rich Mira PLR, heavily-reddened C-rich Miras fall below the PLR and would bias our fit (Ishihara et al., 2011; Whitelock et al., 2003). From our simulations, we find that our amplitudes are well-recovered, with the mean amplitude of the input and recovered Miras within a few 0.01 mag of each other.

Besides using the period and amplitude of the sine fit, to remove imposters we may also compare the quality of the fit to that of a monotonic rise or fall. We compare each object's goodness of fit to a sine and a line using the F-statistic, which is defined as

$$F = \chi_s^2/\chi_l^2, \tag{3.2.1}$$

where χ_s^2 is the reduced χ^2 of a sine fit and χ_l^2 is the reduced χ^2 for a line fit. This statistic may be used to retain only objects with light curves for which a sine fit is preferred over a straight line. We use simulations to determine the best value for the F-statistic to retain Miras while removing noisy, static stars. We find that keeping sources with $F < 0.5$ is a fairly optimal choice; it removes $\sim 92\%$ of the nonvariable stars while keeping $\sim 80\%$ of all of our simulated variables.

Examples of the straight-line and sine fits are shown in Figure 3.2. We further visually inspect all of the objects that pass these criteria to remove spurious fits.

3.2.3 Period Cut

We limit our sample to $P < 400$ days to exclude Miras undergoing hot-bottom-burning (although we would expect few if any HBB stars in this part of the galaxy because HBB stars typically have masses $> 3\,M_\odot$, which will be rare). An additional rationale for our period limit is that our observations span ~ 370 days, making the accurate recovery of periods greater than 400 days problematic. Figure 3.3 illustrates the simulated period recovery rate as a function of period, and Figure 3.4 shows the recovered and input periods. We considered a period recovered if the measured and true values were within 15% of each other. As a statistical error, this criterion would limit a period uncertainty to less than the apparent scatter of the PLR.

We also limit our sample at the short-period, faint end of the PLR, owing to magnitude incompleteness. The Mira PLR has an intrinsic width and not all stars at the same

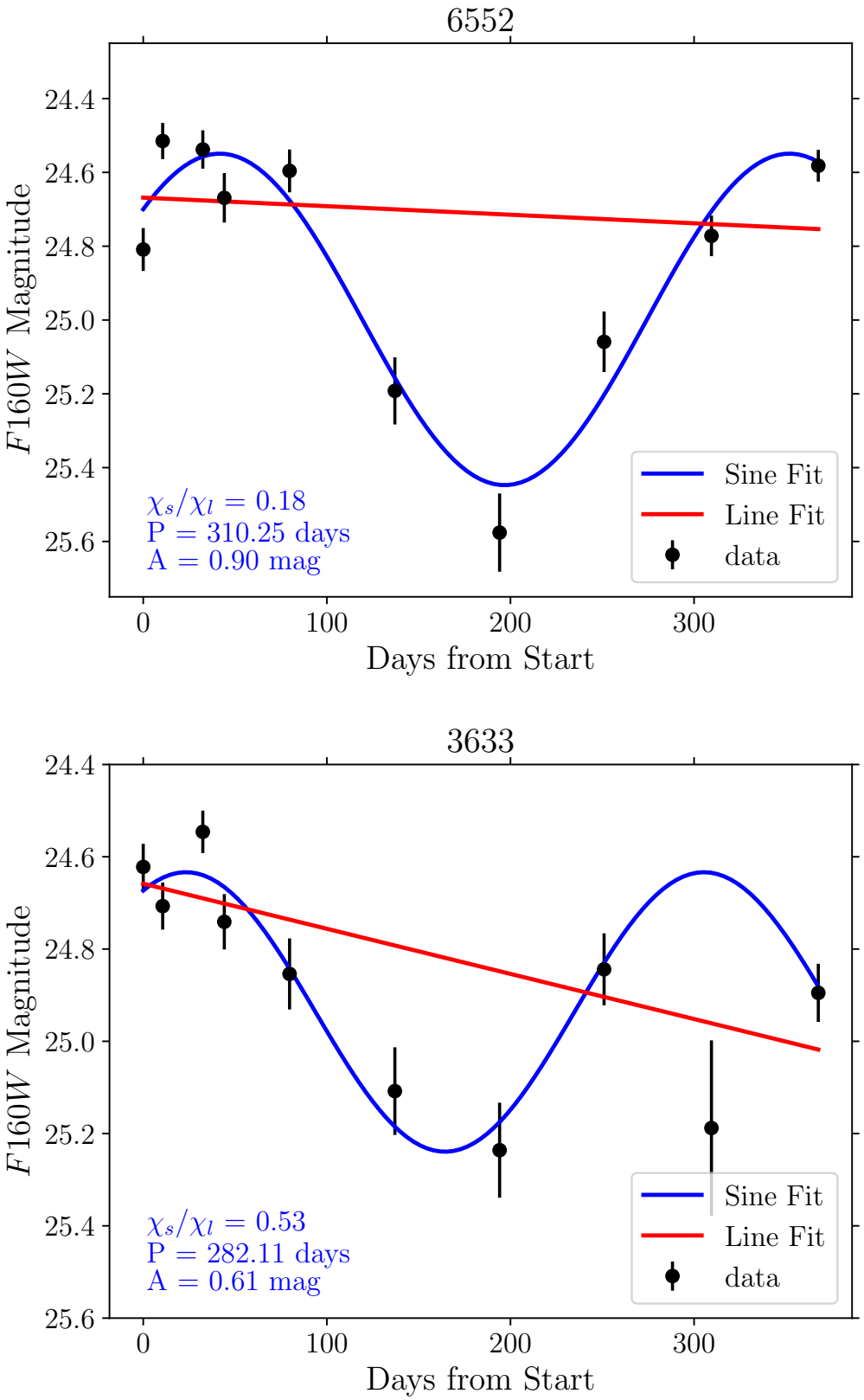

Figure 3.2 *Top:* An example of a variable that passed the F-statistic cut. *Bottom:* An example of a variable that failed the reduced F-statistic cut.

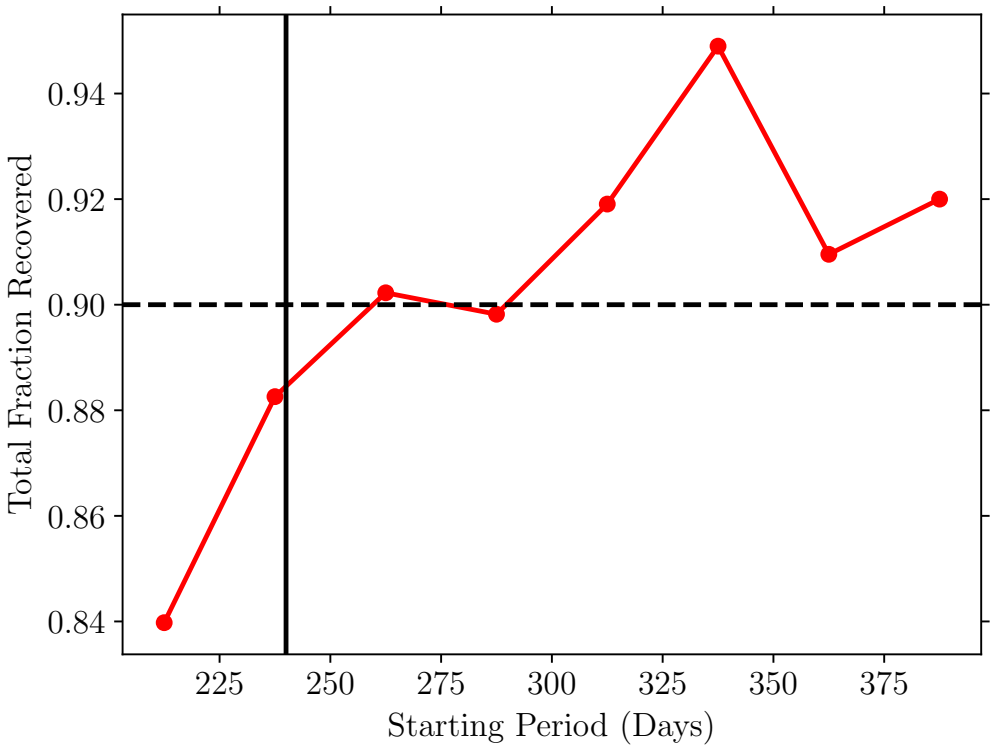

Figure 3.3 The fraction of simulated Miras recovered in our final sample as a function of period and smoothed into 25-day bins. We considered a period recovered if it was within 15% of the true period. The simulated Miras that passed our variability criterion were considered to be recovered as variables. The dashed line shows the 90% completeness limit. The black line shows the adopted 240-day lower period limit.

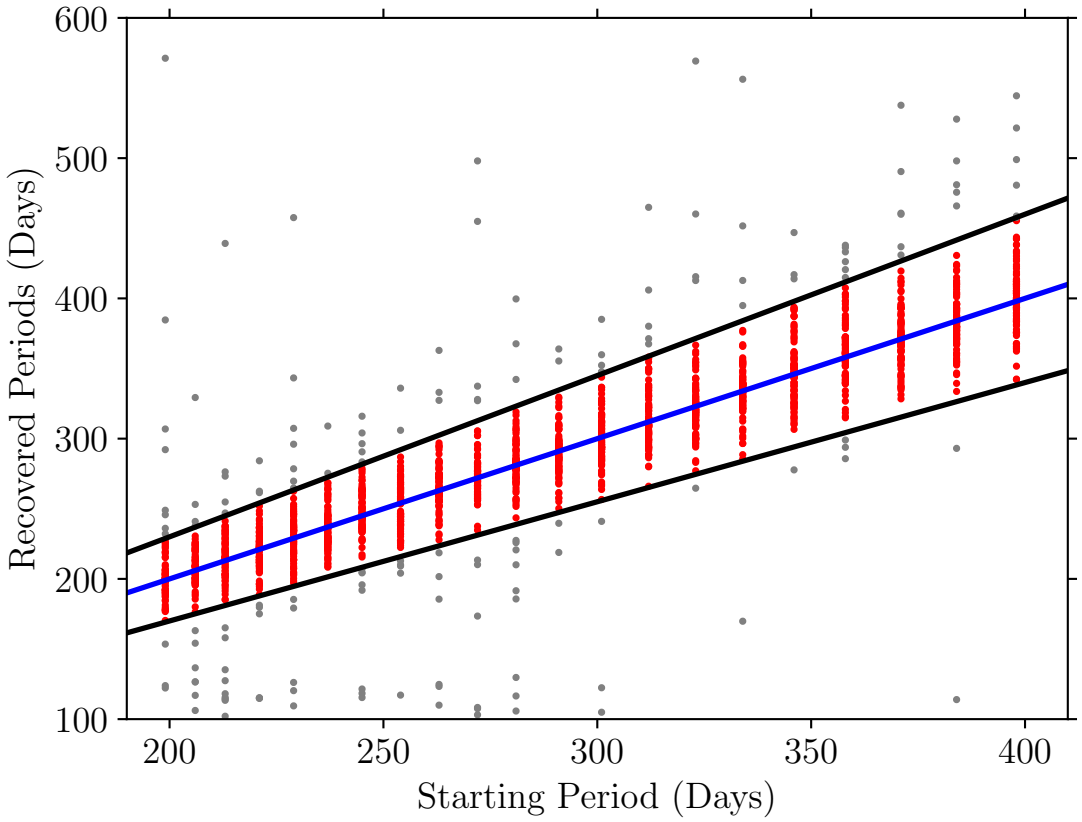

Figure 3.4 The input and recovered periods in our simulations. Red points are considered "recovered" (within 15% of the true input period). Black lines indicate the region of recovered periods. Gray points show periods that were not recovered by the simulation. The blue line shows $x = y$, where the true and recovered periods match exactly.

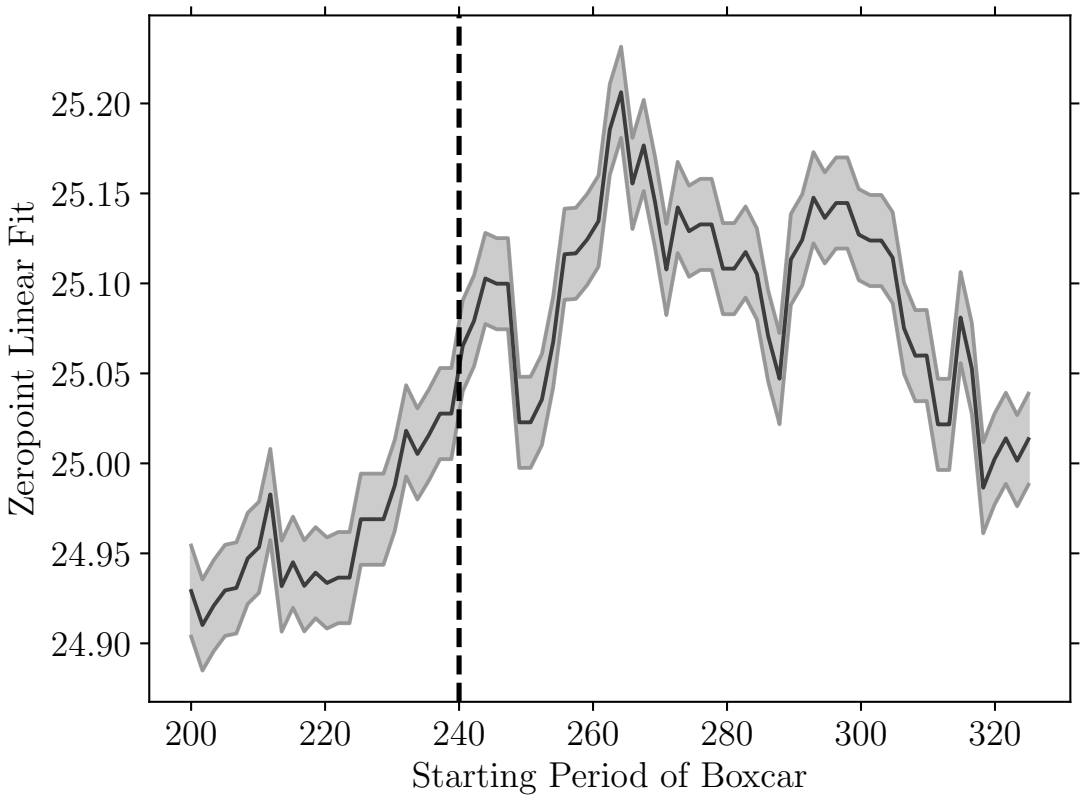

Figure 3.5 The zeropoint as a function of the starting period of each bin, using a boxcar fit with a width of 75 days. At $\sim$ 240 days (black dashed line) the zeropoint starts to converge and oscillate about the true value. We chose 240 days as the minimum period based on this result. The black line shows the zeropoint using the *F160W* slope. The gray lines denote the uncertainty in the zeropoint at each point.

period have the same magnitude. This means that the faintest stars at shorter periods are undetected, biasing us toward the brighter end of the PLR. Additional scatter due to the crowding and photometric errors further increases this magnitude range. We search for the minimum period above which we avoid this bias using three approaches.

First, to obtain an idea of the expected lower bound on our search for the completeness limit, we use the *HST* Exposure Time Calculator (ETC) to calculate the estimated signal-to-noise ratio (SNR) for each period range. We derive a preliminary fit to the candidate Mira PLR to relate Mira periods to their mean magnitudes. We then determine whether that mean magnitude would be detected at SNR > 5 at the depth of each imaging epoch, a minimum requirement for useful detection. This analysis leads us to draw the initial lower bound at $\sim$ 200 days. While this is the theoretical low-period limit to which we should discover Miras, in practice, crowding and the intrinsic width of the Mira PLR introduce additional scatter causing some Miras near that limit to go undetected. Thus, we only use the ETC results as a starting point.

Next, we proceed to look for the expected empirical signature of incompleteness — an approximate plateau of the PLR intercept or zeropoint at long periods and a brightening trend of the zeropoint as we cross the period completeness limit toward the short-period direction. In order to find the location of this break, we start at the initial value of 200 days from the *HST* ETC analysis and use a moving 75-day window (boxcar) to reduce the noise and measure the period-range average of the zeropoint. The result is shown in Figure 3.5. At $P > 240$ days the trend reaches a plateau (with oscillations due to noise and irregular sampling above this).

Finally, we use simulations (described in Section 3.2.6) to verify this empirical result based on the *expected* recovery rate.

Figure 3.3 displays the number of sources recovered as a function of starting period. We can see that an increasing fraction of stars is recovered as the input period increases, and at $\sim$ 240 days the recovery fraction reaches $\sim$ 90%, which is in accord with the empirical analysis. Therefore, we choose this period as our short-period end for the completeness.

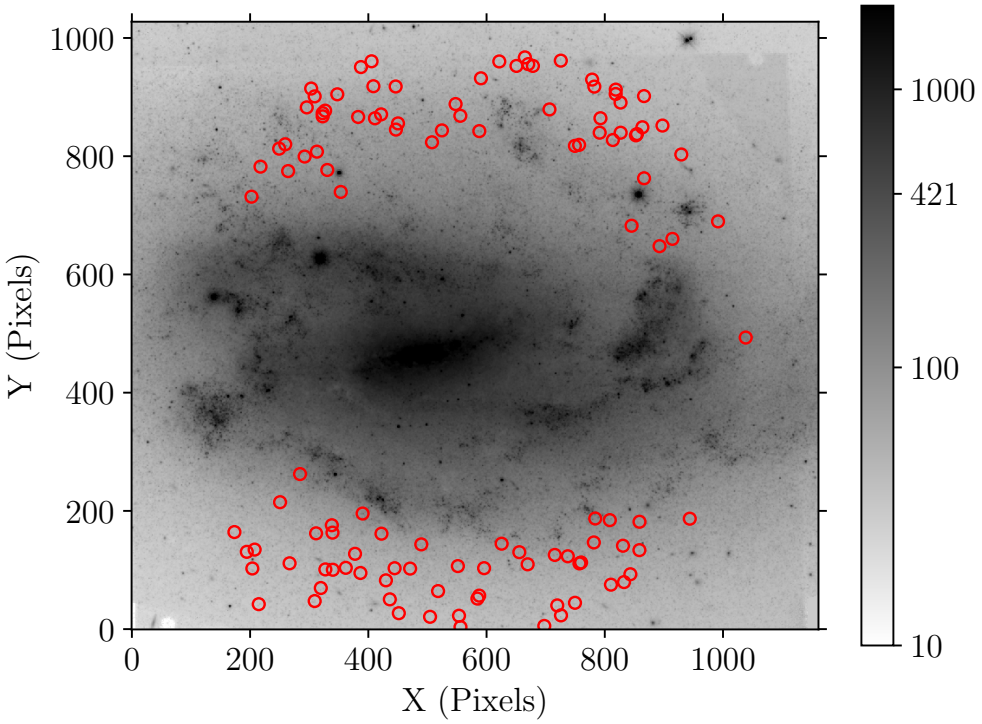

Figure 3.6 The distribution of Miras (in red circles) overplotted on the *F160W* master image. The colorbar shows the surface brightness in counts arcsec^{-2}. We used a surface brightness cutoff of 421 counts s^{-1} arcsec^{-2}, indicated on the colorbar.

3.2.4 Surface Brightness and Crowding

Cepheid analyses (Riess et al., 2016; Hoffmann et al., 2016) in the NIR routinely use artificial star injection and recovery to correct for the artificial brightness in detected sources due to unresolved background sources — that is, crowding. We follow this approach. Like the Cepheid analyses, we choose not to include objects in very crowded regions, thereby reducing the size of this correction (and its associated uncertainties). In the case of NGC 1559, this is most effectively addressed by including a requirement for low surface brightness background.

NGC 1559 has high surface brightness near the center, causing the image to be particularly crowded toward the nucleus of the galaxy (see Figure 3.6). The inclination of the galaxy, $i \approx 57.3°$ (Kassin et al., 2006), is a likely contributing factor to its high surface brightness near the center. Through our artificial star tests (described in the following section), we found that the crowding bias corrections would generally exceed 1 mag throughout an elliptical region around the center, meaning that these sources are dominated by the background, and will lose reliability compared to Miras in less crowded regions. We measured the local surface brightness in this region as the average number of counts per second in a $2''$-wide box around each candidate. We identified a minimum surface brightness of ~ 420 counts per second per square arcsecond as corresponding to this contiguous region and set this as the boundary for the maximum allowed surface brightness to be included in our sample. This leaves objects that are mainly distributed in the outer regions of the galaxy, as seen in Figure 3.6. As expected of aged populations, the Miras in NGC 1559 are evenly distributed in the regions of lower surface brightness, and do not follow spiral arms or other galactic structures.

After using surface brightness cuts to remove objects that would be in the most crowded regions, we employ artificial star tests to determine the individual crowding bias for the remaining candidate Miras. For each remaining Mira candidate we fit an initial PLR. We then inject 100 artificial stars for every Mira, using the Mira's period and the initial PLR fit to determine a starting point for the artificial star magnitude. The artificial star is randomly dropped within a $2''$ radius of the Mira, so that both are in the same environment.

We perform aperture and PSF photometry on the artificial stars exactly as we would

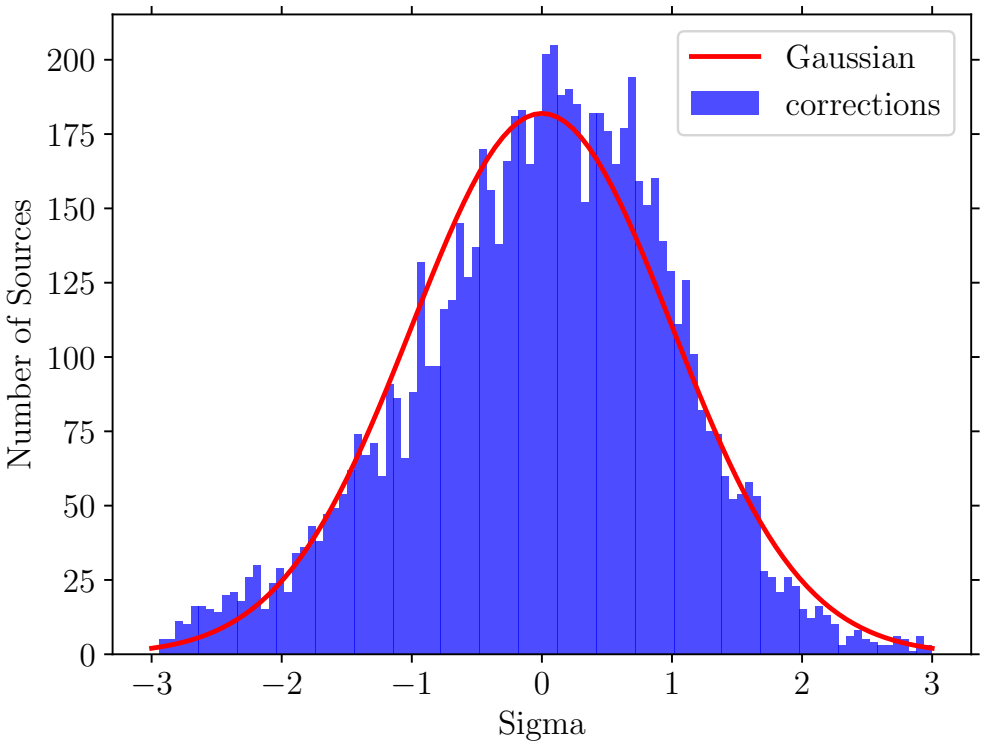

Figure 3.7 The distribution of crowding corrections for all of the artificial stars, after 3σ clipping and removing blended artificial stars. For each Mira, we use 100 artificial stars to measure its crowding correction. We then subtract the mean crowding correction for each Mira from its set of 100 artificial stars and divide all of the corrections by the standard deviation. The red line shows a Gaussian distribution, while the blue histogram is the actual distribution.

with the real Miras and measure the mean magnitudes at which they are recovered. The difference in magnitude between the input artificial stars and the output is used to get a first estimate of the correction for each star. The magnitude of the original Miras is then corrected before refitting the PLR to determine a new guess for the true magnitudes, and the process is repeated until the Mira magnitudes converge. The corrections apply to our use of the mean magnitude of the Mira (defined by the mean of the sine fit).

Occasionally, our artificial stars will fall close enough to a bright background star that the two will be"blended" (i.e., unresolved). If the superimposed star is sufficiently bright, this blending would suppress the amplitude of a variable star enough that it is unlikely to be recovered as a Mira based on our minimum-amplitude requirement. We approximate the blended amplitude by the expression

$$F = 10^{-0.4\Delta m} + 10^{-0.4A\phi}, \tag{3.2.2}$$

where Δm is the difference in magnitude between the two stars (positive if the background star is fainter), A is the amplitude of a Mira, and ϕ is the phase of the Mira. We can likewise calculate the magnitudes at the peak and trough of the lightcurve and subtract the two to obtain a new blended amplitude. At an original amplitude of 0.6 mag (mean of our range), and a background star 1 mag fainter than the artificial star, we find that the blended amplitude is ~ 0.4 mag, our cutoff for the low-amplitude end. Blended stars brighter than this threshold would cause the mean Mira to be removed solely on the basis of amplitude cuts. Thus, we consider the artificial star to be blended if it is within 1 pixel of a bright star (defined as < 1 mag fainter than the Mira) and these (like real blended Miras) are not included in our artificial star samples.

After a 3σ clip of the artificial star sample (the same clip we eventually use when fitting the PLR), we take the standard deviation of these crowding corrections to get an estimate for the uncertainty in each Mira's mean magnitude. We use the mean of the clipped crowding corrections to correct the magnitude of each Mira. Figure 3.7 shows the distribution of crowding corrections for all of our artificial stars, after subtracting the mean correction for each Mira and dividing by the standard deviation of the corrections for each Mira. This distribution in magnitudes compares well to a Gaussian distribution (in red).

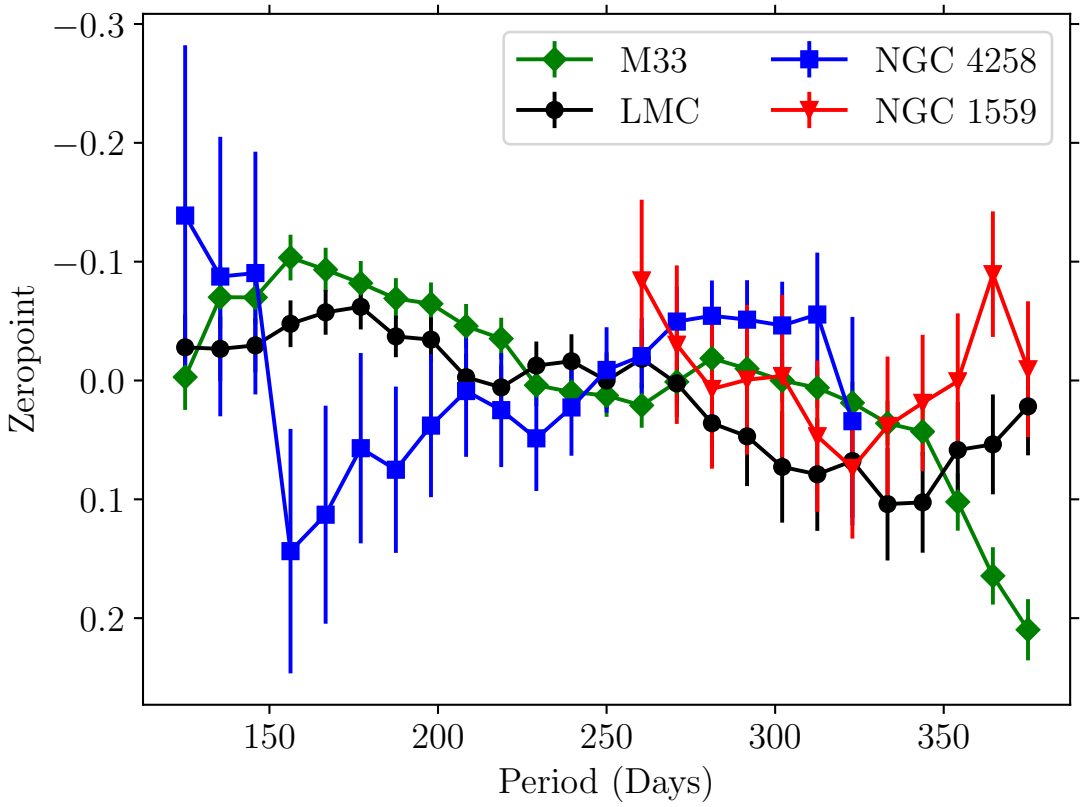

Figure 3.8 The zeropoint as a function of period for the contaminated samples from the LMC and M33 (in black and green, respectively) and for NGC 1559 and NGC 4258 (in red and blue, respectively). For the LMC and M33, we first convert the ground-based J and H data to *F160W* using our color term and then apply an amplitude cut to the combined C-rich and O-rich Mira dataset to simulate a contaminated sample before fitting the zeropoint in each bin.

We also conservatively eliminate 5 Mira candidates (3% of the sample) that have a crowding correction $\Delta m_b > 0.5$ mag. Although these may yield good measurements, this level of crowding is significantly greater than for the rest of the sample (the mean crowding correction is ~ 0.13 mag, with a standard deviation of 0.14 mag). The local surface brightness criterion already excludes the majority of candidates that would have fallen into this category, so this final cut ensures that all of the objects remaining are in uncrowded regions.

3.2.5 C-Rich Mira Contamination

Although we used amplitude cuts to reduce the number of C-rich Miras or nonvariable stars in our sample, here we quantify and correct for a potentially low level of residual contamination from C-rich Miras. C-rich Miras are typically fainter than O-rich Miras

in *F160W*; thus, C-rich contamination in the Mira PLR can result in a fainter absolute magnitude calibration. We employ the OGLE-LMC sample — the most complete sample of Mira variables with well-categorized Miras — to measure the difference in zeropoint between a pure O-rich sample and a model C-rich-contaminated sample (by mixing O-rich and C-rich LMC Miras). We note that this is not a large correction because for the LMC, the contaminated sample would shift the zeropoint by ~ 0.07 mag.

To create the LMC "contaminated sample," we convert the 2MASS ground-based J and H data from the LMC to *F160W* and then apply the same amplitude cuts and sigma-clipping used for NGC 4258 and NGC 1559. In the LMC, at $P < 400$ days, the ratio of O-rich to C-rich Miras is approximately 2 : 3 before the amplitude cuts and 2 : 1 after. As expected, the amplitude cuts remove the majority of C-rich Miras in this range. Then we calculate the zeropoint (i.e., the PLR intercept) as a function of period by fitting a PLR with a fixed slope to the Mira sample binned by 50 days. As shown in Figure 3.8, the zeropoint of the contaminated sample grows fainter as the contamination by C-rich Miras increases ($P \gtrsim 250$ days), whereas a purely O-rich sample ($P < 250$ days) is relatively flat. Therefore, we can use the change in zeropoint of the LMC contaminated sample as a template to measure the contamination in other hosts.

We take the samples of Miras in M33 (also well-categorized into C-rich and O-rich subclasses) from Yuan et al. (2018) as a test of our ability to measure the contamination. The observations of M33, like NGC 1559 and NGC 4258, impose a magnitude limit on the Mira sample such that the C-rich population is relatively incomplete compared to the O-rich population. We combine the O-rich and C-rich samples from Yuan et al. (2018) which pass our amplitude cuts and measure the zeropoint as a function of period. Adopting the LMC curve from Figure 3.8 as a model for C-rich contamination, we fit the M33 curve from Figure 3.8 using the form

$$Z_1 = \alpha Z_{\rm LMC} + \beta, \tag{3.2.3}$$

where Z_1 is the zeropoint of the contaminated M33 PLR as a function of period, $Z_{\rm LMC}$ is the zeropoint of the contaminated LMC PLR as a function of period, and α and β are fit parameters: β simply shifts the curve and does not contribute to a correction, while α tells us the amount to correct the zeropoint as a function of the total difference

in zeropoint between the combined and O-rich-only values.

For M33 we find that $\alpha = 0.58 \pm 0.18$ is the best fit to the LMC curve. For the LMC, the difference in zeropoint is -0.07 ± 0.013 mag. Therefore, in order to correct the zeropoint of the combined C-rich and O-rich M33 dataset to match the zeropoint of the O-rich-only M33 set, $m_c = -0.04 \pm 0.01$ mag. The known difference in zeropoint of the purely O-rich and the contaminated PLR is -0.034 mag, within the uncertainties of our contamination correction. We now apply this same technique to NGC 1559 and NGC 4258.

In Figure 3.8, we plot the change in zeropoint as a function of period for NGC 4258 and NGC 1559. Applying the LMC as a model to NGC 4258 and NGC 1559, we find that $\alpha = -0.77 \pm 0.25$ for NGC 4258, but $\alpha = 0.81 \pm 0.35$ for NGC 1559, indicating some possible C-rich contamination. We determine an overall correction to the zeropoint of NGC 1559 of $m_c = -0.057 \pm 0.024$ mag. We apply this correction to the m_f given in Eq. 3.1.2,

$$m_{cf} = m_f + m_c, \tag{3.2.4}$$

where m_c is the C-rich correction. For NGC 4258, where $\alpha < 0$, we do not correct for any possible C-rich contamination, since C-rich contamination should only make the zeropoint fainter, not brighter.

We would expect to find more C-rich contamination in NGC 1559 than in NGC 4258 because the range of Mira periods extends up to 400 days in NGC 1559 and only up to 300 days in NGC 4258, and there are more C-rich stars at longer periods. Depending on the amount of circumstellar extinction, C-rich Miras can be as much as 2–3 mag fainter in the H band than O-rich Miras having the same period (Ita & Matsunaga, 2011). Thus, we would also expect to find less contamination in magnitude-limited samples like NGC 1559 and NGC 4258 than in the complete sample in the LMC, in good agreement with the results of our C-rich contamination corrections.

3.2.6 Simulations

To test the efficacy of our selection criteria, we use simulated light curves of Miras and nonvariable stars. We also use the simulations to determine the amount of contamination that we might expect from nonvariable stars, and the completeness limit of the sample.

For each simulation, we inject 105 artificial variable stars into the star catalogs at 21 periods between 200 and 400 days. The artificial stars have random phases, similar to our Mira sample. We use a sine wave of the appropriate period and a starting amplitude of 0.7 mag, the estimated median "true" amplitude of our sources. We then include a scatter of 0.4 mag to the mean magnitude of the source to mimic the spread of our Mira PLR. Next, using the *HST* ETC, we estimate the SNR of each source, add in the appropriate noise, randomize the starting phase, and sample the light curve at the observation dates of our survey. We perform the rest of the variability search on these stars just as we would for the true Miras. The same is done for nonvariable stars to see the effects of the variability cuts on both the simulated Miras and nonvariable stars. Nonvariable stars are simulated by using starting magnitudes in the same range as the Mira variables, but with zero amplitude.

To test the level of nonvariable star contamination, we simulate 10,000 nonvariable stars at the catalog level and then apply all of our Mira selection criteria (outlined in Sections 3.2.1, 3.2.2, and 3.2.3). We find four stars that passed all of the variability cuts. However, all four stars also fall more than 1.5 mag below the Mira PLR and were sigma-clipped out of the final sample. Thus, we conservatively estimate that we may have 1 nonvariable star contaminant per 10,000 nonvariable stars in the master star list. Out of the observed star list of 49,000, approximately 40,000 are nonvariable stars. We expect an upper limit of four nonvariable star contaminants in the Mira PLR and we do not expect these to meaningfully bias the PLR.

3.3 Systematics

In this section, we discuss the sources of systematic uncertainties in our analysis, summarized in Table 5. Specifically, we consider the effect of slope on the zeropoint (§3.3.1) and potential systematics from reddening (§3.3.2). Our present uncertainty in H_0 is dominated by the uncertainty from a single SN Ia, with the systematic uncertainties discussed below being subdominant.

Table 3.5. Systematic and Statistical Uncertainties

Source	Systematic Uncertainty (mag)	Statistical Uncertainty (mag)
a_B	0.00176	—
Aperture Correction	—	0.01
C-rich Correction	—	0.024
Color Term	0.02	—
Differential Extinction	0.04	—
LMC Distance Modulus	0.0263	—
LMC Zeropoint	—	0.01
NGC 1559 Zeropoint	—	0.038
NGC 4258 PLR	—	0.017
NGC 4258 Distance Modulus	0.032	—
Uncertainty in Slope (both slopes)	0.01	—
Supernova Peak Magnitude	—	0.11
Subtotals (NGC 4258)	**0.052**	**0.050**
Subtotals (LMC)	**0.033**	**0.047**

Note. — With the new maser distance to NGC 4258 (Reid et al., 2019), the uncertainty in the extinction is now the dominant source of systematic uncertainty. Uncertainties shown are for preferred value of H_0 using two anchors and the slope we fit after converting ground-based data to *F160W* (−3.35). The subtotals give the amount of statistial and systematic error for the calibration of the distance modulus of NGC 1559 ($\sigma_{\mu 1559}$ from Equation **??**) assuming a 240-400 day period range. The color-term uncertainty comes from H18, and is the estimated uncertainty from using a ground-based sample (LMC) to calibrate the *HST* samples. Thus, it does not contribute to the systematic error when using the NGC 4258 only as an anchor.

3.3.1 Slope

Miras and other variable stars are typically fit with a linear PLR, and we apply two different choices of slopes derived from LMC Miras. Because the Mira samples in NGC 4258 and NGC 1559 have lower SNR and a shorter period range than thoes in the LMC, we do not attempt to use these to derive an independent slope, though this may become possible as the SN-Mira host sample grows.

The first slope is derived by Yuan et al. (2017b) using observations of about 170 LMC O-rich Miras in the H band, which is the closest match to *F160W*:

$$m = a_0 - 3.64(\log P - 2.3), \tag{3.3.1}$$

where P is the period in days, m is the H-band magnitude, and a_0 is the intercept or zeropoint. For the "gold" sample of NGC 4258 Miras, we obtain $a_0 = 23.15 \pm 0.017$ mag (statistical error only) with this slope.

In addition to the slope determined by Yuan et al. (2017b), we use the OGLE LMC variable-star database to estimate the slope of the Mira PLR in *F160W* by transforming

from ground-based IR data to the *HST* bandpass. Using 2MASS J and H data for OGLE LMC Mira variables, we adopt the color correction derived by H18,

$$m_{F160W} = H + 0.39(J - H), \tag{3.3.2}$$

to convert their O-rich Mira sample from ground-based J and H into *F160W* magnitudes. This sample includes only periods below the HBB cutoff, $P = 400$ days, to better match our *HST* sample. Using this sample of 416 Miras with $P < 400$ days, we obtain a slope fit of

$$m = a_0 - 3.35(\log P - 2.3). \tag{3.3.3}$$

For this slope, we obtain $a_0 = 23.18 \pm 0.017$ mag (statistical error only) for the NGC 4258 gold sample of Miras. In Table 5 we include a systematic uncertainty based on the differences in a_0 when using these two slopes.

3.3.2 Extinction

Using the Schlafly & Finkbeiner (2011) dust maps, we find that the Galactic extinction in the direction of NGC 1559 in the 2MASS J band is ~ 0.022 mag and the 2MASS H band is ~ 0.014 mag. However, for the purposes of calibration, we are affected by the difference in extinction between NGC 4258 and NGC 1559. The Galactic foreground extinction at the location of NGC 4258 in the 2MASS J and H bands is 0.012 and 0.007 mag (respectively), for a difference of 0.01 and 0.007 mag between the two, for which we correct as follows:

$$m_{\rm PLR} = m_{cf} + m_e, \tag{3.3.4}$$

where $m_{\rm PLR}$ is the final mean magnitude of the Mira (which we use for fitting the PLR), m_{cf} is the C-rich contamination-corrected mean magnitude defined in Equation 3.2.4, and m_e is the correction for the differential foreground extinction, which we estimate to be 0.01 mag. The *F160W* lies between the J and H bands, so we derive its extinction by interpolating between the J and H bands.

We expect the *difference* between the Mira interstellar extinction in NGC 1559 and NGC 4258 to be quite low. Miras are not a disk population where dust is concentrated.

Table 3.6. Summary of Mira H_0 Values

Anchor	Period Range (days)	H_0 (km s^{-1} Mpc^{-1}) Slope = −3.35	Slope = −3.64
NGC 4258	$240 < P < 300$	74.6 ± 4.8	74.7 ± 4.8
NGC 4258	$240 < P < 400$	72.7 ± 4.5	72.5 ± 4.5
LMC	$240 < P < 400$	73.9 ± 4.2	73.6 ± 4.2
LMC + NGC 4258	$240 < P < 400$	**73.3 ±3.9**	73.2 ± 3.9

Note. — The H_0 with two anchors and the slope fit using *F160W* (−3.35) is our preferred value.

The positional distribution of the NGC 4258 Mira sample (see H18) is uniform, and thus should mimic a lower extinction halo distribution. Likewise for NGC 1559, most of our sources are in the outer regions of the galaxy and thus would have low extinction. Most importantly, our measurements are at 1.6 μm which is much less sensitive to extinction than shorter wavelengths. However, there could be a small difference in the extinction between the regions where the NGC 4258 and NGC 1559 Miras are located. Riess et al. (2009) suggested a ~ 0.04 mag differential extinction between Cepheids in the H band between NGC 4258 and SN hosts, and we propagate this value as a systematic uncertainty to account for a difference in interstellar extinction.

3.4 Results and Discussion

The uncertainty for each Mira mean magnitude (determined from the sine fit) is given by

$$\sigma_{\rm tot} = \sqrt{\sigma^2_{\rm int} + \sigma^2_{\rm crowd}}, \tag{3.4.1}$$

where $\sigma_{\rm int}$ is the intrinsic scatter of the Mira PLR and $\sigma_{\rm crowd}$ is the measurement error given by the standard deviation of the recovered artificial star distribution. We use an intrinsic scatter of ~ 0.13 mag derived from LMC observations of Miras. The DAOPHOT photometric errors are typically < 0.1 mag, and are included in the artificial star results. The total uncertainty in most cases is dominated by the measurement error, as indicated by the artificial stars.

Using water megamasers orbiting the center of the galaxy, Reid et al. (2019) obtained

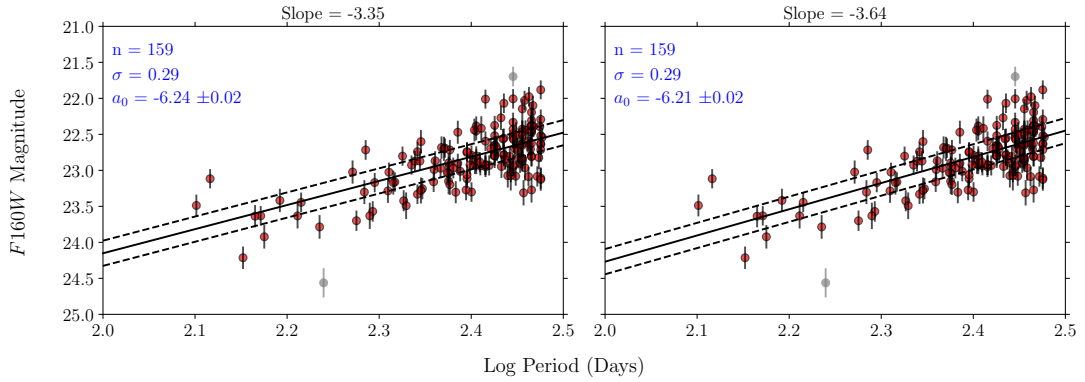

Figure 3.9 The linear PLR for the gold sample of Miras from H18 with the *F160W* slope derived from the OGLE LMC O-rich Mira data (left) and the *H*-band slope from Yuan et al. (2017a). H18 originally used only a quadratic PLR. Thus, we have refit the same data with a linear PLR to obtain a calibration for the linear Mira PLR. Red points were used in the fit and gray points were excluded from the clip via sigma-clipping. Dashed black lines show the 1σ dispersion. The error in the zeropoint only include the statistical errors.

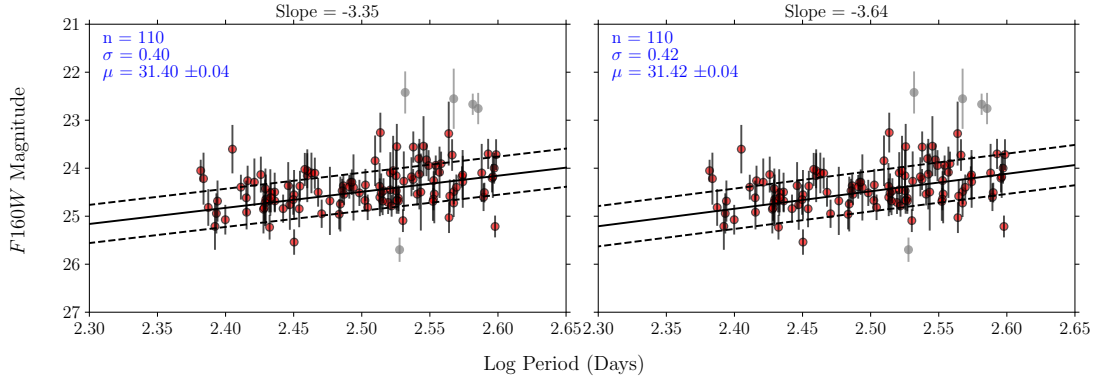

Figure 3.10 The final PLRs with the *F160W* slope derived from the OGLE LMC O-rich Mira data (left) and with the *H*-band slope from Yuan et al. (2017a). Red points were used in the fit and gray points were excluded via a 3σ clip, consistent with our artificial star tests. Dashed black lines show the 1σ dispersion. The uncertainties listed in the distance modulus include only the statistical errors.

the most precise geometric distance to NGC 4258 to date, of 7.58 ± 0.08 (stat) ± 0.08 (sys) Mpc. Thus, the distance modulus for NGC 4258 is $\mu = 29.398 \pm 0.0324$ mag. Using this we calculate an absolute calibration of $a_0 = -6.25 \pm 0.036$ mag for the Mira linear PLR using the *F160W* slope and $a_0 = -6.21 \pm 0.036$ mag for the *H*-band slope (both containing systematic and statistical errors). These PLRs are shown in Figure 3.9.

We then use the absolute calibration from NGC 4258 to derive absolute distances to NGC 1559 of $\mu = 31.41 \pm 0.052$ (sys) ± 0.040 (stat) mag and $\mu = 31.42 \pm 0.052$ (sys) $\pm$ 0.040 (stat), respectively. The PLRs for NGC 1559 are shown in Figure 3.10.

NGC 1559 was host to the normal SN Ia 2005df. Its color-corrected, light-curve corrected peak magnitude on the Pantheon SN Ia sample system (Scolnic et al., 2018) is $m_B = 12.14 \pm 0.11$ mag, resulting in a calibration of the fiducial SN Ia absolute magnitude $M_B^0 = -19.27 \pm 0.13$ mag. The uncertainty in M_B^0 is given by

$$\sigma_M = \sqrt{\sigma_{\mu 1559}^2 + \sigma_{\rm SNe}^2}, \tag{3.4.2}$$

where σ_M is the uncertainty in M_B^0, $\sigma_{\mu 1559}$ is the uncertainty in the Mira-calibrated distance modulus to NGC 1559, and $\sigma_{\rm SNe}$ (= 0.11 mag) is the uncertainty in the corrected peak magnitude of SN 2005df. This agrees well with the fiducial value for SNe Ia calibrated by Cepheids in 19 SN Ia hosts (R16) of $M_B^0 = -19.28 \pm 0.05$ mag based on the geometric calibrations of Cepheids in NGC 4258.

From the combination of the SN Ia absolute magnitude derived here and the intercept of the SN Ia Hubble diagram we can determine the value of the Hubble constant.

We derive H_0 using

$$\log H_0 = (M_B^0 + 5a_B + 25)/5, \tag{3.4.3}$$

where a_B is the intercept of the SN Ia magnitude-redshift relation. The value for a_B is adopted from R16, $a_B = 0.71273 \pm 0.00176$. To get the uncertainty in H_0, we sum in quadrature σ_M and $5\sigma {a_B}^2$.

We find $H_0 = 72.7 \pm 4.5$ km s^{-1} Mpc^{-1} with a measurement uncertainty of 6.1% based on the masers in NGC 4258 as the sole geometric source of calibrating the luminosity of Miras.

We also calculate the distance modulus to NGC 1559 using only Miras with periods

between 240 and 300 days. This is the period range of Miras in NGC 1559 that overlaps with the periods of Miras in NGC 4258. Using the subset of Miras from NGC 4258 in this period range to calibrate, we find that for the *F160W* slope, we have $a_0 = -6.25 \pm 0.06$ mag. For the H-band slope this becomes $a_0 = -6.21 \pm 0.06$ mag. This gives us a distance modulus to NGC 1559 of $\mu = 31.36 \pm 0.08$ mag using the *F160W* slope and $\mu = 31.36 \pm 0.08$ mag using the H-band slope, resulting in $H_0 = 74.6 \pm 4.8$ km s^{-1} Mpc^{-1} for the former. Selecting a smaller period range increases our statistical error.

As an alternative source of calibration of Mira luminosities we can use the LMC in lieu of NGC 4258. The LMC OGLE-III sample of long-period variables and our color terms yield an intercept (apparent) of the LMC sample of 12.28 ± 0.01 mag. Using the distance modulus to the LMC from detached eclipsing binaries of 18.477 ± 0.004 (stat)± 0.026 (sys) mag (Pietrzyński et al., 2019), we obtain an absolute calibration of $a_0 = -6.27 \pm 0.03$ mag in the *F160W* bandpass. Using this calibration, we estimate a distance modulus to NGC 1559 of $\mu = 31.38 \pm 0.06$ mag. The calibration of SN 2005df using the LMC Mira sample results in $M_B^0 = -19.24 \pm 0.133$ mag and gives us $H_0 = 73.9 \pm 4.2$ km s^{-1} Mpc^{-1}.

We combine the two anchors by taking a weighted mean of the distances to NGC 1559 using the LMC and using NGC 4258 as anchors. The uncertainty in the weighted mean distance is given by

$$\sigma_{\rm wm} = \sqrt{\left(\frac{1}{\sigma^2_{\rm LMC}} + \frac{1}{\sigma^2_{4258}}\right)^{-1}}, \tag{3.4.4}$$

where $\sigma_{\rm LMC}$ is the uncertainty using the LMC as an anchor and σ_{4258} is the uncertainty using NGC 4258 as an anchor. Combining the two anchors, $H_0 = 73.3 \pm 3.9$ km s^{-1} Mpc^{-1} and $M_B^0 = -19.26 \pm 0.117$ mag.

All of these measurements of H_0 are within 1σ of the Cepheid-based values from R16 and R19, and they are dominated by the statistical uncertainty from the sole SN Ia calibrator. Both the systematics inherent to the Mira PLR ($\sim$ 0.05 mag) and the statistical error ($\sim$ 0.05 mag) are subdominant to the random error ($\sim$ 0.11 mag) of having only one calibrator. We are targeting three additional SN Ia host galaxies that will eventually have both Cepheid and Mira calibrations of SNe. These additions to the local calibrator SN sample size will decrease the overall uncertainty on the Mira H_0 by

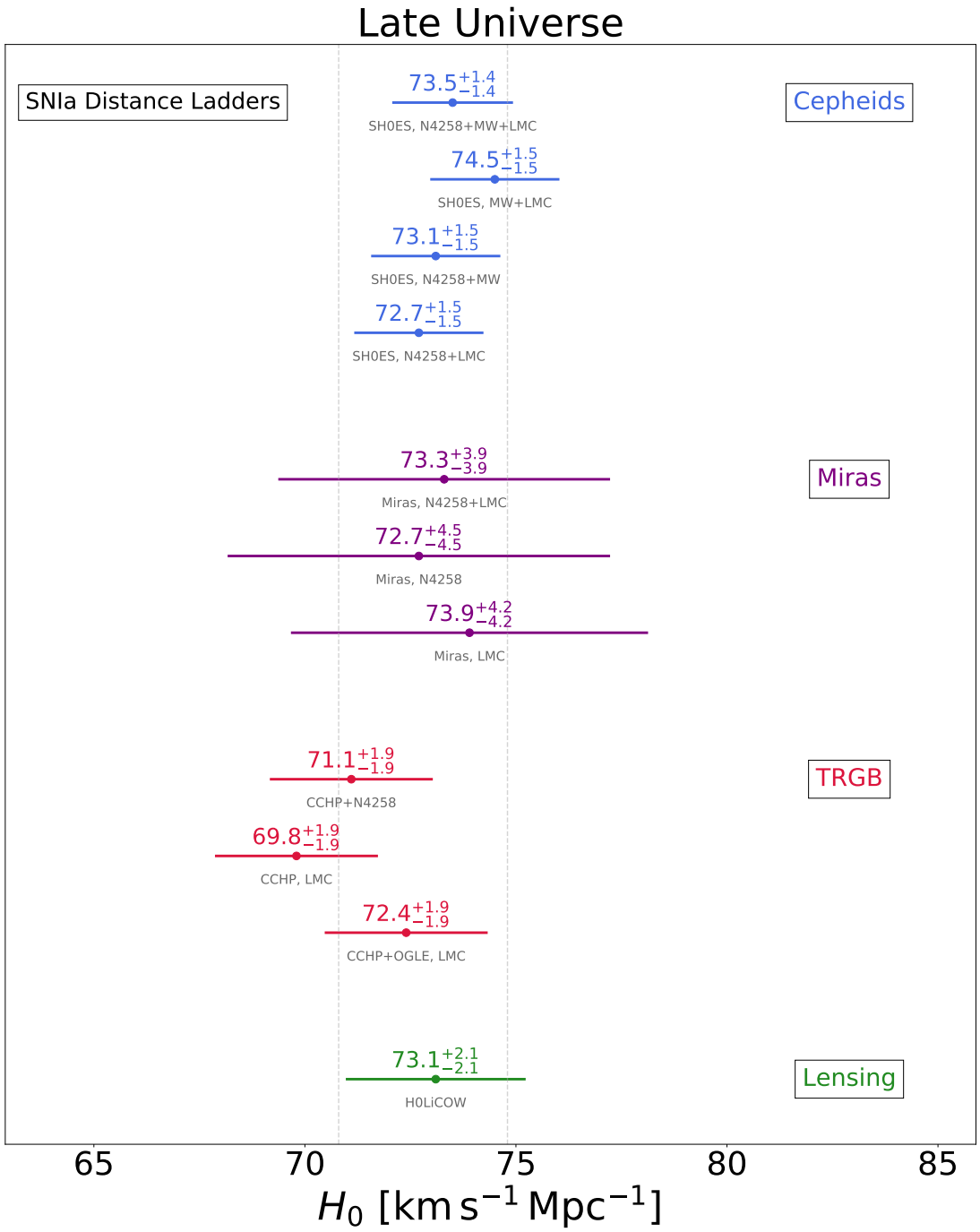

Figure 3.11 A summary of recently-published late-Universe H_0 measurements using different SN Ia distance ladders and anchors and their 1σ uncertainties. The set shown are those reviewed by Verde et al. (2019). Featured are Cepheid results from R16 and R19 (in blue) with calibration from Reid et al. (2019), Mira results from this paper (in violet), TRGB from Freedman et al. (2019) (CCHP), Yuan et al. (2019) (CCHP+OGLE) and Reid et al. (2019) (CCHP+N4258) (in red), and gravitational lensing time delays from Taubenberger et al. (2019) used to calibrate SNe Ia (in green). For Cepheids, Miras, and TRGB, the combinations of anchors used are denoted in gray under the measurement points. Gray dashed vertical lines mark a range of 4 km s^{-1} Mpc^{-1}, ± 2 km s^{-1} Mpc^{-1} centered on the mean of the measurements.

a factor of 2 and decrease the random uncertainty from the the SN calibrators.

Figure 3.11 shows a set of different approaches recently used to calibrate the SN Ia distance ladder and measure H_0 as recently reviewed by Verde et al. (2019). As shown, the Mira calibration of SN Ia is in good agreement with the mean from Cepheid, TRGB and strong lensing.

The Mira sample in NGC 1559 contains the most distant Miras for which we have measured periods and magnitudes. They are also the first Miras to be used to calibrate the absolute luminosity of a SN Ia, and thus the first Mira-based determination of H_0. With the absolute calibration from NGC 4258 on the *HST* filter system, we can remove biases from converting from the ground-based filter magnitudes to *HST* WFC3/IR magnitudes.

In addition to showing that we can detect Miras in nearby SN hosts, we have shown that it is possible to find them in the halos of galaxies. This confirms that Miras can be used to increase the nearby SN sample by allowing us to look at edge-on galaxies in addition to early-type galaxies that are not actively star-forming.

While newer space telescopes like *JWST* may eventually surpass the ability of *HST* to observe Miras in the NIR, *HST* currently remains the best option for searching for Miras in SN host galaxies. *JWST* offers advantages and challenges for observing Miras. Its higher sensitivity and resolution are great advantages to reach more-distant hosts, but searching for time-variable phenomena poses challenges as *JWST* has only two continuous viewing zones near the North and South ecliptic poles, where year-round observations would be possible.

3.5 Conclusions

In H18, we calibrated the absolute magnitude of Miras using a sample observed with *HST* WFC3-IR in the megamaser host galaxy NGC 4258. In this paper, we present a sample discovered in NGC 1559, use them to calibrate SN 2005df, and demonstrate that Miras can fulfill a role historically occupied by Cepheids as the second rung of the distance ladder. Now we are undertaking a program to calibrate the luminosity of SNe Ia in other galaxies with Miras, which can yield an independent cross-check on the Cepheid-based H_0 measurements.

To review, we identified ~ 3000 potential variable objects in 10 epochs of *HST* NIR imaging of NGC 1559, and we used selection criteria designed to identify O-rich Miras to narrow this down to a final sample of 115 objects. We empirically corrected for sample contamination by C-rich Miras using the LMC as a model.

Potential systematics that affect our measurement include the reddening, color, bias due to crowding, and uncertainty in the slope of the PLR. Our estimate of the zeropoint is dominated by the systematic error, since we are only fitting a single parameter to the PLR. Reddening should be negligible based on small foreground extinction and location of the Miras in the halo of NGC 1559, away from the most crowded regions.

Finally, we determine a distance to SN 2005df host NGC 1559, the first estimate of distance to a such a host with Miras. We use the absolute calibration from NGC 4258 to anchor the Mira distance scale and measure a value of H_0, 72.7 ± 4.5 km s^{-1} Mpc^{-1}, in good agreement with the Cepheid-calibrated H_0 to within 1σ of the uncertainties. In addition, the values of H_0 for the subset of the data at the same period range as the Miras in NGC 4258, 74.6 ± 4.8 km s^{-1} Mpc^{-1}, and (adding the LMC as an additional anchor) our preferred value of 73.3 ± 3.9 km s^{-1} Mpc^{-1}, are also consistent with the Cepheid-calibrated H_0.

This paper demonstrates that Miras can be used as calibrators for local SNe Ia. The ubiquity of Miras means that they can be found in a wider range of local SN Ia hosts, thereby increasing the sample of possible calibrators, and also potentially making the results more representative of the Hubble-flow sample.

Acknowledgements

We are grateful to John Soltis for providing Figure 3.11, the compilation of recent H_0 measurements.

Support for this work was provided by the National Aeronautics and Space Administration (NASA) through *HST* program GO-15145 from the Space Telescope Science Institute (STScI), which is operated by AURA, Inc., under NASA contract NAS 5-26555. A.V.F. is also grateful for financial assistance from the TABASGO Foundation, the Christopher R. Redlich Fund, and the Miller Institute for Basic Research in Science (UC Berkeley). P.A.W. thanks the South African NRF for a research grant.

Chapter 4

NIR Spectral Classification of Galactic Miras

4.1 Introduction

In Chapters 2 and 3, we found that clean classification of Miras into their O– and C– rich subtypes was challenging using only *HST* broad bands. Even using narrower ground-based filters, photometric classifications of AGB stars can still have an error rate of $\sim$ 7% (Sibbons et al., 2015). Spectra remain the cleanest way to classify AGB stars into subtypes, and a better understanding of Mira spectra, particularly in the NIR and IR, can improve our modeling of these stars. In this Chapter we present preliminary results of a Mira NIR spectral catalogue.

Accurate spectral classification of Miras is integral to their usage as distance indicators. In addition to their application to the distance scale, Miras and other AGB stars are also of purely astrophysical interest as they contribute significantly to the integrated flux of galaxies, particularly in the NIR and IR (Renzini & Buzzoni, 1986). The reddest AGB stars may contribute as much as 80 % of the light of a galaxy in the K band (Lançon & Wood, 2000).

AGB stars begin as O-rich stars with photospheric ratios of C/O < 1. Through dredge-up events, carbon created from the triple-α process in an AGB star's He-burning shell is brought to the surface. This causes the C/O ratio to shift as the amount of carbon on the surface of the star grows. Stars where the C/O ratio ~ 1 are known as S-type stars (S-stars). If the C/O eventually becomes greater than 1, the star is

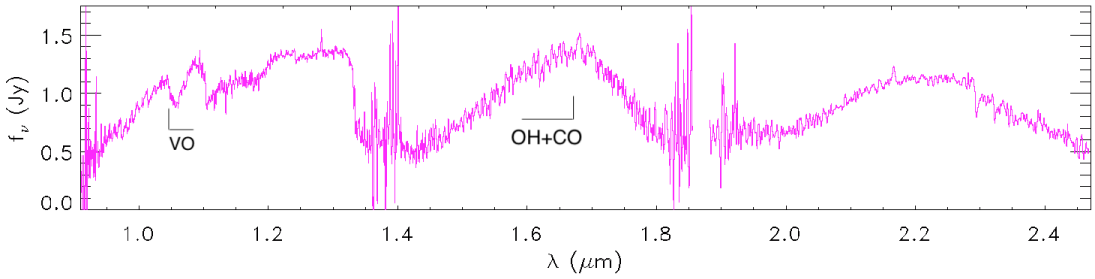

Figure 4.1 The near-infrared spectrum of Mira Z CrB which we classified as O-rich. The location of the VO, OH, and CO are shown. VO becomes prominent in later spectral types of M-stars.

considered C-rich. C-rich stars are more common at lower metallicities because fewer dredge-up events are required to turn the surface chemistry from C/O<1 to C/O >1 (Iben & Renzini, 1983). The ratio of the number of C-stars to M-stars (O-rich stars) is called the C/M ratio, and can be used as an proxy for the local metallicity at the time that they were born.

There are a number of molecules that can serve to separate C– and O– rich stars. C and O present in the photosphere will tend to form carbon monoxide (CO). When there is more oxygen than carbon, the remaining oxygen will form a variety of oxides in the stellar photosphere. When the ratios are approximately equal (S-type stars, C/O $\sim 0.9-1.0$), Zirconium Dioxide (ZrO) will dominate the spectrum. For carbon stars, the dominant spectral features will be small carbonaceous molecules and all of the oxygen will be locked in CO.

4.2 Observations and Data Reduction

This catalogue contains spectra taken the ARC 3.5m telescope instrument TripleSpec (Wilson et al., 2004) located at Apache Point Observatory in Sunspot, New Mexico. TripleSpec is cross-dispersed NIR spectrograph that has wavelength coverage from 0.95-2.46μm in five spectral orders. The wavelength coverage overlaps with the NIR J, H, and K photometric bands. We used the primary configuration for the spectrograph, which has a spectral resolution of R= 3500 in a 1.1$''$ slit at 2.1 pixels per slit on the spectrograph array.

The data was collected over the course of 8 total half-nights between July 20, 2017 and May 07, 2018. Each half-night, we took 10 60s flat field observations using bright

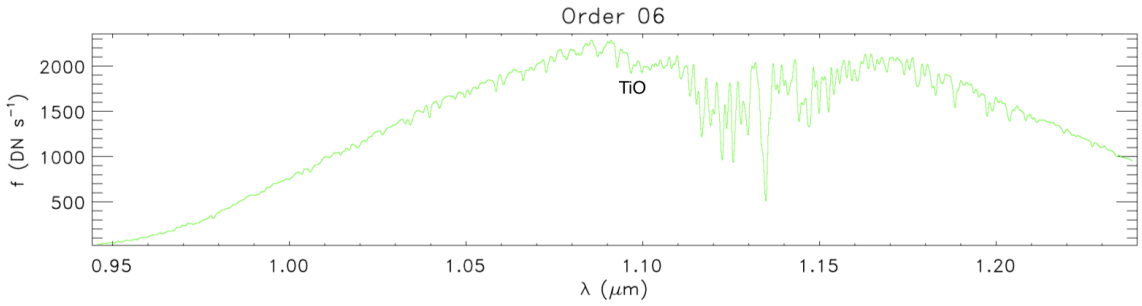

Figure 4.2 The sixth order of the NIR spectrum for SS Her, an O-rich Mira that we classified using the 1.1μm TiO feature. This feature is much less prominent than VO and right before the start of telluric features.

quartz lamps and 10 60s open shutter dark images. Integration times for the Miras typically varied between 1s to 60s. The dark images were either taken at the beginning or end of the night. Observations were collected using an alternating slit nodding sequence of ABBA.

We reduce the spectra using the APO `TripleSpecTool`, an `IDL` package that accepts raw data files from TripleSpec and can produce combined and telluric-corrected spectra. We begin by using the `xspextool` program to generate a single normalized flat field. The individual flat field exposures are combined into one master flat field using their median values. We create a new master flat field for each night of observation due to changes in the position of the spectrum on the detector which are caused by the instrument flexor. Next, we construct wavelength calibration (wavecal) files with `xspextool`. We also construct new wavecal files for each night of observation. The wavecal files use lines from telluric OH to determine the wavelength as a function of position. We use standard star files where the star is far from the center of the slit to create the wavecal files.

Next, the sources are extracted using the wavecal and flat field files. Because we observed with an ABBA nodding sequence, each pair of images is subtracted and the result divided by the normalized flat field in order to produce spatial profiles that we use to define the apertures. We then define extraction apertures by examining the spatial profile along each order. The extraction aperture determines the size of the aperture that `xspextool` uses to compute the source flux of each column. Based on the spatial profiles of our sources, we use an aperture size of 2″. We also subtract the sky background, which is defined with an inner aperture radius of 3″ with a width of 2″.

We then use `xcombspec` to combine all of the spectra taken of one object over the

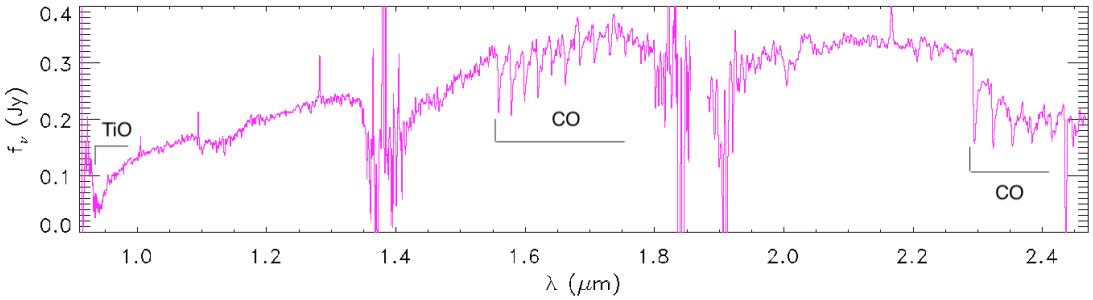

Figure 4.3 The combined, telluric-corrected spectrum for V0890 Cas. All spectra orders have been combined. We classified this Mira as having an S-type based on the TiO and CO features.

course of one evening, with the exception of a few cases where the airmass changed by greater than ~ 0.1 in between observations. The spectral order with the highest signal-to-noise ratio (SNR) is used to determine the median level of each spectra, and normalize them before combining. Atmospheric molecules (primarily H_2O and CO_2) produce telluric features through scattering and absorption. To correct for the telluric lines, we use the program `xtellcorbasic`. This program divides the combined spectra of the target by the combined spectrum of a standard star (at a similar airmass) to remove telluric features. In order to preserve the continuum shape and absolute flux level of the target spectrum, we use the blackbody temperature (estimated from the spectral class of the standard star) and V-band magnitude of the standard star.

The final step in the reduction process is merging the five spectral orders into one spectrum. We use the program `xmergeorders` for this step. The lowest order is used as the anchor order, and the other orders are added one by one, with scaling if necessary. In the case of wavelength overlaps with neighboring orders, we choose the orders with the higher SNR in the overlap regions, and clip the ends of the lower SNR orders.

4.3 Target Selection and Spectral Classification

Mira targets were selected from the General Catalogue of Variable Stars (GCVS) (Samus' et al., 2017). For each half-night, we selected targets that would be visible at airmass 1.3 or lower during the majority of our observation window. We prioritized Miras without a spectral classification listed in the catalogue, and observed additional targets with any remaining observing time.

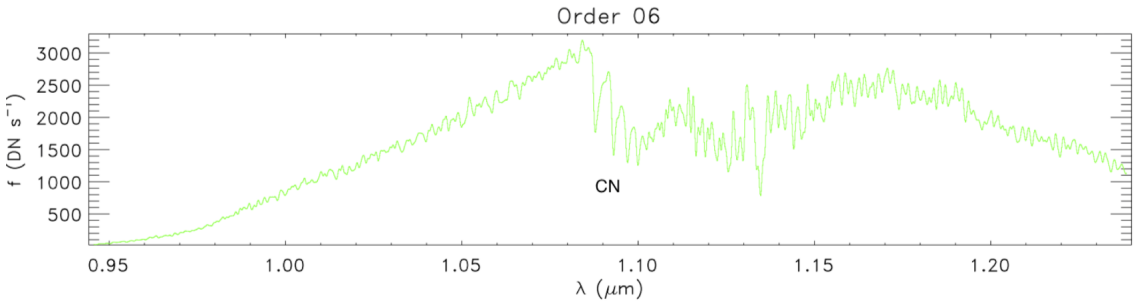

Figure 4.4 The sixth order of the NIR spectrum for T Lyn, an C-rich Mira that we classified using the broad CN feature that begins at $\sim 1.075\mu$m and extends into the telluric lines.

Standard stars were chosen from Persson et al. (1998). For each night we observed 2-4 standard stars in addition to our Mira targets. For each target, the standard star with most similar airmass was used to correct its telluric features. The NIR standards from Persson et al. (1998) were chosen to be solar analogues, and thus, if the spectral type of the standard stars used could not be separately verified (as in the case of 9188), we assumed that they were G2V and had the same blackbody temperature as the Sun. For standard stars for which we could not find V-band magnitudes, we approximated the V-band magnitude using the J-band magnitude and using a template G2V star spectrum.

After the spectra are reduced, we use absorption features to determine their spectral classification. The 1μm to 1.4μm range (similar to J band) of our observations is generally the most useful for spectral classification. In this region, O-rich stars have Titanium Oxide (TiO) or Vanadium Oxide (VO) bands, S-type stars have Zirconium Dioxide (ZrO) features, and C-rich stars have C_2 and CN.

4.3.1 O-rich Stars

When present, the VO feature starting at 1.046 μm is the clearest indicator of an O-rich photosphere. Figure 4.1 shows an O-rich Mira variable from our study — Z CrB — and its VO band. However, only stars with spectra type M6 or later typically exhibit strong VO features (Wright et al., 2009).

In cases where the VO bands are not visible, we use TiO and a combination of OH and CO bands (beginning around) instead. Figure 4.2 shows a single order of the combined spectra for SS Her, with the location of one of the TiO features marked. TiO

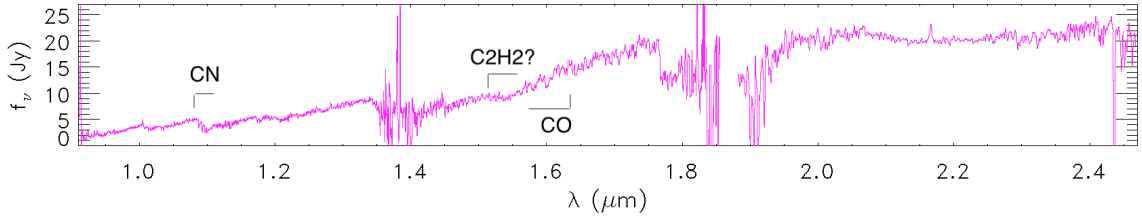

Figure 4.5 The combined, telluric-corrected spectrum for V0666 Cas. We classified this Mira as having an C-type based on the CN, CO, and possible C_2H_2 features.

features are visible for stars cooler than $\sim$ 3600 K, and later than $\sim$M3 (Lançon et al., 2007). The most prominent TiO feature is located at .92μm, but it also overlaps with a telluric feature. There are additional TiO features at .97μm, 1.1μm and 1.2μm.

OH features start at around 1.53μm and overlap with CO features. This causes them to blend, and makes them distinguishable from S-type stars whose spectra are dominated by CO. In addition, the shape of the continuum in the *H*-band window for O-rich stars is affected by the strength of photospheric water vapor bands on either side, at around 1.4-1.5μm and 1.7-1.8μm. At later spectral classes, the strength of the photospheric water bands increases, limiting the transmission to the middle of the *H*-band window.

4.3.2 S-type Stars

S-type stars represent an evolutionary stage between O and C stars, when the ratio of carbon-to-oxygen in the photosphere is approximately equal. This causes their spectra to be dominated by CO bands. Occasionally we find stars displaying characteristics of both an S-type star and a C-or-O-type star. In those cases, we label the spectral type as S/C or S/O.

S-type stars are typically classified by the presence of TiO at 0.92μm or ZrO at 0.93μm in addition to CO bands that start at 1.56μm to about 1.7μm. While O-rich stars will also have CO bands, their spectra contain OH bands that interfere with the CO bands. Thus, the CO bands in S-type stars are much more prominent. Figure 4.3 shows the spectrum of a star we identify as S-type, V0890 Cas. The locations of both the TiO and the CO bands are delineated.

Though we do not encounter any such stars in our sample, S-type stars of later spectral type are most easily identified by a pair of ZrO bands at 1.03μm and 1.06μm. Like the VO feature in O-rich stars, there are no other small molecular features in that

Table 4.1. Spectral Classification

Mira	Period	Classification	Class (Lit)	H Mag	R.A.	Dec	Lines
S Boo	269.88	O	O	3.594	14 22 52.92	+53 48 37.30	TiO
Z Boo	282.2	O	O	4.24	14 06 29.54	+13 29 05.61	VO
RR Boo	194	O	O	5.521	14 47 05.78	+39 19 01.56	VO
RT Boo	275.5	O	O	3.06	15 17 14.71	+36 21 33.44	TiO
V0500 Cas	250	S	S	6.391	02 51 32.96	+57 50 34.31	CO
V0666 Cas	424	C	C	3.59	02 01 28.15	+58 18 13.97	CN
R CMi	340	C	C	2.77	07 08 42.61	+10 01 26.46	CN
T Com	406	O	O	4.01	12 58 38.91	+23 08 21.23	VO
W CrB	238.4	O	O	4.145	16 15 24.55	+37 47 44.21	VO
X CrB	241.17	O	O	3.7	15 48 53.53	+36 14 52.59	TiO
Z CrB	250.68	O	O	4.62	15 56 08.42	+29 14 17.92	VO
U CVn	342.9	O	O	3.613	12 47 19.61	+38 22 30.66	VO
RT CVn	253.9	O	O	5.982	13 48 44.69	+33 43 34.30	VO
SY Dra	391.38	O	O	3.096	17 33 57.81	+53 57 37.51	VO
R Her	318.14	O	O	3.46	16 06 11.71	+18 22 13.20	VO
W Her	280.03	O	O	3.521	16 35 12.32	+37 20 43.014	VO
AQ Her	280.91	O	O	4.529	17 56 00.43	+42 52 23.45	TiO
AS Her	269.14	O	O	2.179	16 38 51.85	+14 03 58.35	TiO
CF Her	306.2	O	O	3.54	17 44 53.78	+21 29 46.63	VO
DF Her	337.7	O	O	3.088	18 06 33.46	+20 16 20.98	VO
RS Her	219.7	O	O	3.608	17 21 42.35	+22 55 16.05	VO
RT Her	298.08	O	O	4.18	17 10 48.04	+27 03 59.00	TiO
RV Her	205.23	O	O	5.925	17 00 33.25	+31 13 23.82	TiO
SS Her	107.36	O	O	5.943	16 32 55.54	+06 51 29.74	TiO
SU Her	333.8	O	O	2.984	17 49 01.72	+22 32 22.96	VO
SY Her	116.91	O	O	4.809	17 01 29.25	+22 28 38.72	TiO
UZ Her	263.74	O	O	3.81	17 30 22.95	+17 54 50.50	VO
VV Her	385.64	O	O	3.489	16 12 29.75	+24 53 57.13	VO
VY Her	300.38	O	O	3.6	17 07 17.61	+17 10 22.81	TiO
V0697 Her	475	O	O	3.657	16 27 51.35	+34 48 10.54	VO
WW Her	312.37	O	O	5.291	17 24 30.083	+46 08 05.96	VO
VX Gem	379.4	C	C	3.36	07 12 48.97	+14 36 03.72	CN
CW Leo	630	C	C	4.03	09 47 57.41	+13 16 43.56	CN
S Leo	190.16	O	O	5.84	11 10 50.76	+05 27 34.78	TiO
V Leo	273.35	O	O	3.79	10 00 01.92	+21 15 44.36	VO
S LMi	233.83	O	O	4.074	09 53 43.17	+34 55 35.34	TiO
T Lyn	406	C	C	3.64	08 22 42.85	+33 31 09.47	CN
AW Oph	239	O	O	7.235	18 08 38.74	+04 33 42.75	TiO
KU Oph	382.5	O	O	4.513	18 05 04.57	+02 46 11.62	VO
RT Oph	426.34	O	O	2.41	17 56 32.03	+11 10 09.70	VO
RU Oph	202.29	O	O	5.379	17 32 52.64	+09 25 24.85	VO
RW Oph	246.71	O	O	4.956	17 55 20.47	+07 49 48.01	VO
SV Oph	215.93	O	O	5.872	17 56 24.76	+03 22 38.17	VO
UY Oph	332	O	O	4.125	17 16 24.84	+04 43 16.88	VO
VW Oph	285	O	O	4.978	17 27 25.94	+04 13 39.07	VO
V0421 Oph	337	O	O	3.83	17 36 44.45	+10 51 06.88	VO
V0790 Oph	370	O	O	3.83	17 36 44.45	+10 51 06.88	VO
V0873 Oph	151	O	O	5.618	18 07 11.40	+08 25 02.28	VO
V2582 Oph	260.98	O	O	5.22	16 51 25.10	+08 18 51.36	VO
EL Per	167	S	O	2.86	02 40 16.62	+52 08 26.99	CO
V0672 Per	—	O	O	5.382	02 56 18.02	+45 53 13.13	VO
U Ser	237.5	O	O	4.38	16 07 17.66	+09 55 52.47	TiO
AH Ser	283.5	O	O	5.923	15 59 20.55	+19 46 47.28	VO
BC Ser	245	O	O	5.045	16 00 58.08	+02 10 27.94	VO
YY Tri	—-	C	C	9.82	02 18 06.04	+28 36 45.35	CO
T UMa	256.6	O	O	3.11	12 36 23.466	+59 29 12.97	VO
RU UMa	252.46	O	O	5.594	11 41 40.25	+38 28 29.26	VO
R Vir	145.63	O	O	2.44	12 38 29.93	+06 59 19.03	VO
U Vir	206.64	O	O	5.26	12 51 05.74	+05 33 11.56	TiO
AO Vir	254.61	O	O	4.96	14 21 51.89	+03 54 27.86	TiO
SU Vir	208.6	O	O	5.823	12 05 14.80	+12 21 38.024	TiO
SV Vir	295.33	O	O	4.106	12 00 20.80	-10 11 05.11	TiO

Note. — A partial list of the Miras with spectral classifications for which we obtained spectra. The H-band magnitudes are single-epoch measurements from 2MASS. The lines column denotes the spectral features that we used to determine the classification. The Classification column denotes our classification while the Class (Lit) column lists the literature classification of the star.

Table 4.2. Spectral Classification

Mira	Period	Classification	H Mag	R.A.	Dec	Lines
AX And	378	O	4.19	02 32 46.14	+46 29 20.31	OH,CO
EM And	280	S	6.397	01 28 14.24	+50 00 14.95	TiO,CO
GU And	280	O	7.777	02 34 31.46	+40 04 06.22	VO
V0416 And	359	O	4.605	01 10 30.43	+45 06 11.57	VO
V0417 And	281	O	5.72	01 16 04.71	+50 11 44.73	OH
V0418 And	305	O	4.016	01 30 05.77	+50 10 00.66	VO
V0420 And	355.8	S	3.728	02 18 21.32	+50 46 03.06	CO
V0448 And	285	S/C	6.672	02 03 21.18	+46 23 47.65	CO,CN
V0459 And	384	O	6.92	02 33 57.92	+45 59 55.78	OH,CO
RT Ari	258.1	O	5.762	03 05 23.91	+19 31 49.82	VO
IN Cas	224	O	7.514	01 40 57.23	+56 19 43.74	OH,CO
PR Cas	342	O	7.359	01 32 51.34	+58 01 32.32	faint VO
V0476 Cas	228	O	6.108	01 43 21.79	+59 21 50.80	faint VO
V0692 Cas	420	O	5.667	02 47 29.08	+58 07 32.26	VO
V0696 Cas	189.5	O	7.682	02 51 40.22	+59 26 40.67	faint VO
V0890 Cas	—	S	6.103	01 07 44.58	+59 03 01.89	TiO,CO
AL Per	145	O	7.252	03 02 03.25	+48 29 49.13	VO
BZ Per	298.6	O	5.835	01 55 12.27	+54 11 11.08	OH,CO
CL Per	266	O	6.322	02 04 54.93	+53 15 49.45	OH,CO
DR Per	287	O	6.389	02 28 25.86	+57 10 06.68	VO
DT Per	228.9	O	7.014	02 31 23.13	+56 52 57.37	VO
EP Per	262	O	7.376	02 55 11.58	+54 25 46.64	TiO
ES Per	251	O	8.437	01 32 50.15	+54 20 35.63	OH
GG Per	277.84	O	5.653	03 11 40.78	+41 38 46.83	VO
LQ Per	—	O	8.009	02 31 27.80	+56 31 39.56	VO,OH,CO
LV Per	420	O	5.896	03 03 52.10	+45 11 42.81	VO
LW Per	373.7	O	4.417	03 07 25.57	+50 57 48.34	VO
V0663 Per	—	O	7.125	02 15 13.94	+56 13 02.86	VO
V0671 Per	—	O	4.676	02 50 45.22	+55 49 00.93	VO
V0673 Per	—	O	5.723	03 05 52.90	+54 20 54.12	VO
AW Psc	—	O	3.36	01 11 15.93	+30 38 06.24	VO
TZ Psc	376	O	5.137	01 22 52.96	+25 23 06.91	VO
VW Psc	296.5	O	5.731	01 14 27.72	+32 41 39.92	VO
RT Tri	115.4	O	7.907	02 21 19.61	+31 52 57.49	OH,CO
CV Vir	146.38	O	9.207	12 30 58.10	+12 18 30.73	TiO

Note. — A partial list of the Miras with no previous spectral classification. The H-band magnitudes are single-epoch measurements from 2MASS. The lines column denotes the spectral features that we used to determine the classification.

region, leaving little room for confusion.

Finally, we search for the presence of weak features typically found in C- or O-rich stars. If we only find features unique to S-type stars, we classify the star as an S-type star. Otherwise, we add an additional classification of C- or O-type.

4.3.3 C-rich Stars

The C-rich Miras in our sample are typically identified using the CN feature around 1.075μm, shown in Figure 4.4. In addition, the shape of the continuum for a C-rich Mira is also easily distinguishable from that of O-rich or S-type Miras. Unlike in S- or O- type stars, the longer wavelength (K-band) end of the spectrum contributes the majority of the flux.

C-rich Miras, like S- and O-type stars, will also display CO features. However, their CO features tend to look "ragged" due to the presence of features from small carbonaceous molecules like CN, which is thought to produce many features along the spectrum. C-rich stars also have a potential C_2H_2 feature in the H-band window. These are shown in Figure 4.5.

4.4 Results and Discussion

We present the spectra and classifications of 97 Galactic Miras. Many of the targets saturated in the lower (longer wavelength) orders. However, because the 6th and 7th orders ($0.92 - 1.20\mu$m) are the most useful for classification and these typically did not saturate, we are still able to classify all of our targets. We also found that in cases where there are no prominent features in the J-band window, the H-band window ($1.4-1.7\mu$m) is the next most helpful region due to the presence of OH, CO, and C_2H_2 bands. In addition, the shape of the continuum in this region differs between C- and O-rich stars due to the presence of deep, potential C_2H_2 features in the former and water vapor in the latter.

Out of 62 Miras we classify that have previous spectral types, 61 of their spectral types agree with the classifications from the literature. The literature classifications are a mixture of photometric and spectrum-based classifications. This suggests that photometric classifications are reliable for separating most C– and O– stars. Table 4.1

shows our classifications for these stars.

Of the 35 newly-classified Miras, we find 31 O-rich stars, 3 S-type stars, and one potential SC star. The results for this group are shown in Table 4.2. We do not find any previously undiscovered carbon stars. It is possible that a few of the S-type stars may actually be O-rich stars with C/O close to 1, since we do not find any that contain the distinctive pair of ZrO features in the J-band window.

Acknowledgements

C.D.H. thanks David O. Jones for training her to use the 3.5m telescope and APO observatory staff for helping with nightly observations.

Bibliography

Addison, G. E., Watts, D. J., Bennett, C. L., et al. 2018, ApJ, 853, 119

Aringer, B., Girardi, L., Nowotny, W., Marigo, P., & Bressan, A. 2016, MNRAS, 457, 3611

Aringer, B., Girardi, L., Nowotny, W., Marigo, P., & Lederer, M. T. 2009, A&A, 503, 913

Aylor, K., Joy, M., Knox, L., et al. 2019, ApJ, 874, 4

Battinelli, P., & Demers, S. 2005, A&A, 434, 657

Bhardwaj, A., Macri, L. M., Rejkuba, M., et al. 2017, AJ, 153, 154

Blanco, V. M., & McCarthy, M. F. 1983, AJ, 88, 1442

Bono, G., Caputo, F., Marconi, M., & Musella, I. 2010, ApJ, 715, 277

Bonvin, V., Courbin, F., Suyu, S. H., et al. 2017, MNRAS, 465, 4914

Boyer, M. L., Girardi, L., Marigo, P., et al. 2013, ApJ, 774, 83

Boyer, M. L., McQuinn, K. B. W., Groenewegen, M. A. T., et al. 2017, ApJ, 851, 152

Bresolin, F. 2011, ApJ, 729, 56

Castelli, F., & Kurucz, R. L. 2004, ArXiv Astrophysics e-prints, astro-ph/0405087

Cioni, M.-R. L., & Habing, H. J. 2003, A&A, 402, 133

Cioni, M.-R. L., Marquette, J.-B., Loup, C., et al. 2001, A&A, 377, 945

Cioni, M.-R. L., Blommaert, J. A. D. L., Groenewegen, M. A. T., et al. 2003, A&A, 406, 51

Dhawan, S., Jha, S. W., & Leibundgut, B. 2017, ArXiv e-prints, arXiv:1707.00715

Feast, M. W., Glass, I. S., Whitelock, P. A., & Catchpole, R. M. 1989, MNRAS, 241, 375

Follin, B., & Knox, L. 2017, ArXiv e-prints, arXiv:1707.01175

Ford, H. C., Clampin, M., Hartig, G. F., et al. 2003, in Proc. SPIE, Vol. 4854, Future EUV/UV and Visible Space Astrophysics Missions and Instrumentation., ed. J. C. Blades & O. H. W. Siegmund, 81–94

Fraser, O. J., Hawley, S. L., & Cook, K. H. 2008, AJ, 136, 1242

Freedman, W. L., Madore, B. F., Gibson, B. K., et al. 2001, ApJ, 553, 47

Freedman, W. L., Madore, B. F., Hatt, D., et al. 2019, arXiv e-prints, arXiv:1907.05922

Gerasimovic, B. P. 1928, Proceedings of the National Academy of Science, 14, 963

Glass, I. S., & Lloyd Evans, T. 2003, MNRAS, 343, 67

Gonzaga, S. e. a. 2012, The DrizzlePac Handbook

Hamren, K. M., Rockosi, C. M., Guhathakurta, P., et al. 2015, ApJ, 810, 60

Hoffmann, S. L., Macri, L. M., Riess, A. G., et al. 2016, ApJ, 830, 10

Houk, N. 1963, AJ, 68, 253

Huang, C. D., Riess, A. G., Hoffmann, S. L., et al. 2018, ApJ, 857, 67

Humphreys, E. M. L., Reid, M. J., Moran, J. M., Greenhill, L. J., & Argon, A. L. 2013, ApJ, 775, 13

Iben, Jr., I., & Renzini, A. 1983, ARA&A, 21, 271

Inno, L., Matsunaga, N., Romaniello, M., et al. 2015, A&A, 576, A30

Ishihara, D., Kaneda, H., Onaka, T., et al. 2011, A&A, 534, A79

Ita, Y., & Matsunaga, N. 2011, MNRAS, 412, 2345

Ita, Y., Tanabé, T., Matsunaga, N., et al. 2004, MNRAS, 347, 720

Jang, I. S., & Lee, M. G. 2017, ApJ, 835, 28

Jones, R. V., Carney, B. W., & Fulbright, J. P. 1996, PASP, 108, 877

Kassin, S. A., de Jong, R. S., & Pogge, R. W. 2006, ApJS, 162, 80

Kato, D., Nagashima, C., Nagayama, T., et al. 2007, PASJ, 59, 615

Kholopov, P. N., Samus, N. N., Kazarovets, E. V., & Perova, N. B. 1985, Information Bulletin on Variable Stars, 2681

Kleinmann, S. G., & Payne-Gaposchkin, C. 1979, Earth and Extraterrestrial Sciences, 3, 161

Lançon, A., & Wood, P. R. 2000, A&AS, 146, 217

Lançon, A., Hauschildt, P. H., Ladjal, D., & Mouhcine, M. 2007, Astronomy and Astrophysics, 468, 205

Lattanzi, M. G., Munari, U., Whitelock, P. A., & Feast, M. W. 1997, ApJ, 485, 328

Le Bertre, T., Epchtein, N., Guglielmo, F., & Le Sinadier, P. 1994, Ap&SS, 217, 105

Macri, L. M., Ngeow, C.-C., Kanbur, S. M., Mahzooni, S., & Smitka, M. T. 2015, AJ, 149, 117

Macri, L. M., Stanek, K. Z., Bersier, D., Greenhill, L. J., & Reid, M. J. 2006, ApJ, 652, 1133

Madore, B. F. 1982, ApJ, 253, 575

Marigo, P., Girardi, L., Bressan, A., et al. 2017, ApJ, 835, 77

Matsunaga, N., Kawadu, T., Nishiyama, S., et al. 2009, MNRAS, 399, 1709

Mouhcine, M., & Lançon, A. 2003, MNRAS, 338, 572

Nicholls, C. P., Wood, P. R., Cioni, M.-R. L., & Soszyński, I. 2009, MNRAS, 399, 2063

Olivier, E. A., Whitelock, P., & Marang, F. 2001, MNRAS, 326, 490

Paladini, C., Klotz, D., Sacuto, S., et al. 2017, A&A, 600, A136

Payne-Gaposchkin, C. 1954, Annals of Harvard College Observatory, 113, 189

Percy, J. R., Bakos, A. G., Besla, G., et al. 2004, in Astronomical Society of the Pacific Conference Series, Vol. 310, IAU Colloq. 193: Variable Stars in the Local Group, ed. D. W. Kurtz & K. R. Pollard, 348

Percy, J. R., & Deibert, E. 2016, Journal of the American Association of Variable Star Observers (JAAVSO), 44, 94

Persson, S. E., Murphy, D. C., Krzeminski, W., Roth, M., & Rieke, M. J. 1998, AJ, 116, 2475

Pietrzyński, G., Graczyk, D., Gallenne, A., et al. 2019, Nature, 567, 200

Planck Collaboration, Ade, P. A. R., Aghanim, N., et al. 2016, A&A, 594, A13

Planck Collaboration, Aghanim, N., Akrami, Y., et al. 2018, arXiv e-prints, arXiv:1807.06209

Poleski, R., Soszyński, I., Udalski, A., et al. 2010a, Acta Astron., 60, 179

—. 2010b, Acta Astron., 60, 1

Poulin, V., Smith, T. L., Karwal, T., & Kamionkowski, M. 2018, arXiv e-prints, arXiv:1811.04083

Reid, M. J., Pesce, D. W., & Riess, A. G. 2019, arXiv e-prints, arXiv:1908.05625

Rejkuba, M. 2004, A&A, 413, 903

Renzini, A., & Buzzoni, A. 1986, in Astrophysics and Space Science Library, Vol. 122, Spectral Evolution of Galaxies, ed. C. Chiosi & A. Renzini, 195–231

Riess, A. G., Casertano, S., Yuan, W., Macri, L. M., & Scolnic, D. 2019, arXiv e-prints, arXiv:1903.07603

Riess, A. G., Macri, L., Casertano, S., et al. 2009, ApJ, 699, 539

Riess, A. G., Macri, L. M., Hoffmann, S. L., et al. 2016, ApJ, 826, 56

Robertson, B. S. C., & Feast, M. W. 1981, MNRAS, 196, 111

Saio, H., Wood, P. R., Takayama, M., & Ita, Y. 2015, MNRAS, 452, 3863

Samus', N. N., Kazarovets, E. V., Durlevich, O. V., Kireeva, N. N., & Pastukhova, E. N. 2017, Astronomy Reports, 61, 80

Schlafly, E. F., & Finkbeiner, D. P. 2011, ApJ, 737, 103

Scolnic, D. M., Jones, D. O., Rest, A., et al. 2018, ApJ, 859, 101

Sesar, B., Ivezić, Ž., Grammer, S. H., et al. 2010, ApJ, 708, 717

Sibbons, L. F., Ryan, S. G., Napiwotzki, R., & Thompson, G. P. 2015, A&A, 574, A102

Soszyński, I. 2007, ApJ, 660, 1486

Soszynski, I., Udalski, A., Kubiak, M., et al. 2005, Acta Astron., 55, 331

Soszynski, I., Poleski, R., Udalski, A., et al. 2008, Acta Astron., 58, 163

Soszyński, I., Udalski, A., Szymański, M. K., et al. 2008, Acta Astron., 58, 293

—. 2009a, Acta Astron., 59, 1

—. 2009b, Acta Astron., 59, 239

—. 2009c, Acta Astron., 59, 335

—. 2013, Acta Astron., 63, 21

Stetson, P. B. 1987, PASP, 99, 191

—. 1994, PASP, 106, 250

—. 1996, PASP, 108, 851

STScI Development Team. 2013, pysynphot: Synthetic photometry software package, Astrophysics Source Code Library, ascl:1303.023

Taubenberger, S., Suyu, S. H., Komatsu, E., et al. 2019, arXiv e-prints, arXiv:1905.12496

Trabucchi, M., Wood, P. R., Montalbán, J., et al. 2017, ApJ, 847, 139

Udalski, A., Szymanski, M. K., Soszynski, I., & Poleski, R. 2008, Acta Astron., 58, 69

Verde, L., Treu, T., & Riess, A. G. 2019, arXiv e-prints, arXiv:1907.10625

Whitelock, P., Menzies, J., Feast, M., et al. 1994, MNRAS, 267, 711

Whitelock, P. A. 2018, arXiv e-prints, arXiv:1809.10077

Whitelock, P. A., & Feast, M. W. 2014, in EAS Publications Series, Vol. 67, EAS Publications Series, 263–269

Whitelock, P. A., Feast, M. W., Marang, F., & Groenewegen, M. A. T. 2006, MNRAS, 369, 751

Whitelock, P. A., Feast, M. W., & Van Leeuwen, F. 2008, MNRAS, 386, 313

Whitelock, P. A., Feast, M. W., van Loon, J. T., & Zijlstra, A. A. 2003, MNRAS, 342, 86

Wilson, J. C., Henderson, C. P., Herter, T. L., et al. 2004, in Proc. SPIE, Vol. 5492, Ground-based Instrumentation for Astronomy, ed. A. F. M. Moorwood & M. Iye, 1295–1305

Wong, K. C., Suyu, S. H., Chen, G. C. F., et al. 2019, arXiv e-prints, arXiv:1907.04869

Wood, P. R., Alcock, C., Allsman, R. A., et al. 1999, in IAU Symposium, Vol. 191, Asymptotic Giant Branch Stars, ed. T. Le Bertre, A. Lebre, & C. Waelkens, 151

Wright, N. J., Barlow, M. J., Greimel, R., et al. 2009, MNRAS, 400, 1413

Yoachim, P., McCommas, L. P., Dalcanton, J. J., & Williams, B. F. 2009, AJ, 137, 4697

Yuan, W., He, S., Macri, L. M., Long, J., & Huang, J. Z. 2017a, AJ, 153, 170

Yuan, W., Macri, L. M., He, S., et al. 2017b, ArXiv e-prints, arXiv:1708.04742

Yuan, W., Macri, L. M., Javadi, A., Lin, Z., & Huang, J. Z. 2018, AJ, 156, 112

Yuan, W., Riess, A. G., Macri, L. M., Casertano, S., & Scolnic, D. 2019, arXiv e-prints, arXiv:1908.00993

Vita

Caroline Huang was born on June 26, 1991 in Anderson, South Carolina. She received her A.B. in Physics and Astrophysics from Harvard University in 2013. As an undergraduate, she worked on extragalactic astronomy and cosmology. She won the Leo Goldberg Prize for her senior thesis work dark matter annihilation lines supervised by Prof. Douglas Finkbeiner. She started her Ph.D. in Physics in 2013 at the Johns Hopkins University and received an M.A. in 2015.

Caroline received her Ph.D. from Johns Hopkins in 2019 under the supervision of Prof. Adam Riess, where she worked on distance measures in cosmology. Starting in 2019, she will be a Postdoctoral Fellow at Johns Hopkins and Space Telescope Science Institute.